

AD-A053 468

KAMAN AVIDYNE BURLINGTON MASS

F/G 19/4

MEASUREMENTS OF BLAST PRESSURES ON A RIGID 65 DEG. SWEEPBACK WI--ETC(U)

JUN 77 J R RUETENIK, R F SMILEY

DNA001-76-C-0106

UNCLASSIFIED

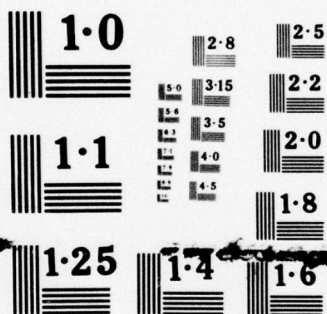
KA-TR-137-VOL-1

DNA-4400F-1

NL

1 OF 2
ADA
053468





NATIONAL BUREAU OF STANDARDS
MICROCOPY RESOLUTION TEST CHART

AD-E300184

DNA 4400F-1

AD A 053468

**MEASUREMENTS OF BLAST PRESSURES
ON A RIGID 65° SWEEPBACK WING
AT MACH 0.76 FROM ROCKET
PROPELLED SLED TESTS**

6
SC

Volume I—Test Documentation

Kaman AviDyne
83 Second Avenue
Burlington, Massachusetts 01803

20 June 1977

Final Report for Period October 1975—May 1977

CONTRACT No. DNA 001-76-C-0106

APPROVED FOR PUBLIC RELEASE;
DISTRIBUTION UNLIMITED.

THIS WORK SPONSORED BY THE DEFENSE NUCLEAR AGENCY
UNDER RDT&E RMSS CODE B342077464 N99QAXAE50101 H2590D.

AD No. _____
DDC FILE COPY

Prepared for
Director
DEFENSE NUCLEAR AGENCY
Washington, D. C. 20305

DDC
RECEIVED
MAY 3 1978
B

14 KA-TR-137-VOL-1

UNCLASSIFIED

SECURITY CLASSIFICATION OF THIS PAGE (When Data Entered)

REPORT DOCUMENTATION PAGE		READ INSTRUCTIONS BEFORE COMPLETING FORM
1. REPORT NUMBER DNA 4400F-1 [✓]	2. GOVT ACCESSION NO.	3. RECIPIENT'S CATALOG NUMBER 9
4. TITLE AND SUBTITLE MEASUREMENTS OF BLAST PRESSURES ON A RIGID 65°deg. SWEEPBACK WING AT MACH 0.76 FROM ROCKET PROPELLED SLED TESTS. Volume I - Test Documentation.		5. TYPE OF REPORT & PERIOD COVERED Final Report, Final Report October 1975-May 1977,
7. AUTHOR(S) 10 J. Ray/Ruetenik Robert F./Smiley		6. PERFORMING ORG. REPORT NUMBER KA TR-137, Volume I [✓]
9. PERFORMING ORGANIZATION NAME AND ADDRESS Kaman Avidyne [✓] 83 Second Avenue Burlington, Massachusetts 01803		8. CONTRACT OR GRANT NUMBER(s) 15 DNA 001-76-C-0106 ^{new}
11. CONTROLLING OFFICE NAME AND ADDRESS Director Defense Nuclear Agency Washington, D.C. 20305		10. PROGRAM ELEMENT, PROJECT, TASK AREA & WORK UNIT NUMBERS 16 NWED Subtask 17 E501 N99QAXAE501-01
14. MONITORING AGENCY NAME & ADDRESS (if different from Controlling Office) 18 DNA, SBIE		12. REPORT DATE 11 20 Jun 1977
19 4400F-1, AD-E300 184		13. NUMBER OF PAGES 150 12 149p
15. SECURITY CLASS (of this report) UNCLASSIFIED		15a. DECLASSIFICATION/DOWNGRADING SCHEDULE
16. DISTRIBUTION STATEMENT (of this Report) Approved for public release; distribution unlimited. 62704H		
17. DISTRIBUTION STATEMENT (of the abstract entered in Block 20, if different from Report)		
18. SUPPLEMENTARY NOTES This work sponsored by the Defense Nuclear Agency under RDT&E RMSS Code B342077464 N99QAXAE50101 H2590D.		
19. KEY WORDS (Continue on reverse side if necessary and identify by block number) Blast Explosives Subsonic Shock Aircraft Sled Test Wing Pressure Vortex Experimental Test Sweepback		
20. ABSTRACT (Continue on reverse side if necessary and identify by block number) Interaction of a blast wave with a highly sweptback wing model was measured in a series of three sled tests, performed on the 50,788-foot track at Holloman Air Force Base in July and August of 1976. The sled, traveling at Mach 0.76, was intercepted progressively by blast waves produced from the sequential detonation of three charges of TNT. → rest pay		

DD FORM 1 JAN 73 1473

EDITION OF 1 NOV 65 IS OBSOLETE

UNCLASSIFIED

SECURITY CLASSIFICATION OF THIS PAGE (When Data Entered)

194 970

JUB

UNCLASSIFIED

SECURITY CLASSIFICATION OF THIS PAGE(When Data Entered)

20. ABSTRACT (Continued)

The model consisted of a sting-mounted wing and fuselage combination. Wing properties were: 46.80-in. span, 18.95-in. mean chord, 2.47 aspect ratio, 0.29 taper ratio, 67 deg. leading edge sweepback, 64.8 deg. quarter-chord sweepback, and a 64A012 wing section. Blast induced loadings were measured at 20 locations on the wing for blast intercept overpressures of about 2 and 4 psi for blast intercept angles of about 20, 90, and 135 degrees from head-on.

A preliminary analysis of the test data indicates the existence of some non-linear blast-induced loads on the model appreciably greater than would be expected on the basis of linearized aerodynamic theory.

Volume 1 of this report describes the tests, and presents and discusses the reduced test data. Volume 2 presents a complete set of the wing pressure time histories in working size plots.

UNCLASSIFIED

SECURITY CLASSIFICATION OF THIS PAGE(When Data Entered)

PREFACE

This work was performed by the Avidyne Division of the Kaman Sciences Corporation for the Defense Nuclear Agency under Contract DNA-001-76-C-0106. MAJ David W. Garrison of the DNA Shock Physics Directorate served as technical monitor.

Dr. J. Ray Ruetenik of Kaman Avidyne was the project leader under Dr. Norman P. Hobbs, Technical Director of KA. Mr. Robert F. Smiley performed engineering functions.

Appreciation is expressed to MAJ Garrison for his continuing interest and significant support of this program. Appreciation is also expressed to the Holloman Air Force Base Test Directorate personnel, particularly Mr. Floyd D. Amburgey of Track Operations for coordination of the test activities, Mr. Daniel J. Krupovage of Track Engineering for mechanical engineering functions and Mr. Joe Haden of Track Instrumentation for electronic and sled-instrumentation support. Appreciation is also expressed to Army Ballistics Research Laboratories personnel headed by Mr. George Teel for providing the blastline measurements.

ACCESSION for		
NTIS	White Section	<input checked="checked" type="checkbox"/>
DDC	Buff Section	<input type="checkbox"/>
UNANNOUNCED		<input type="checkbox"/>
JUSTIFICATION		
BY		
DISTRIBUTION/AVAILABILITY CODES		
Dist.	AVAIL	and/or SPECIAL
A		

CONVERSION FACTORS FOR U.S. CUSTOMARY TO METRIC (SI) UNITS OF MEASUREMENT

To Convert From	To	Multiply By
angstrom	meters (m)	1.000 000 X E -10
atmosphere (normal)	kilo pascal (kPa)	1.013 25 X E +2
bar	kilo pascal (kPa)	1.000 000 X E +2
barn	meter ² (m ²)	1.000 000 X E -28
British thermal unit (thermochemical)	joule (J)	1.054 350 X E +3
calorie (thermochemical)	joule (J)	4.184 000
cal (thermochemical)/cm ²	mega joule/m ² (MJ/m ²)	4.184 000 X E -2
curie	giga becquerel (GBq)*	3.700 000 X E +1
degree (angle)	radian (rad)	1.745 329 X E -2
degree Fahrenheit	degree kelvin (K)	$t_K = (t_F + 459.67)/1.8$
electron volt	joule (J)	1.602 19 X E -19
erg	joule (J)	1.000 000 X E -7
erg/second	watt (W)	1.000 000 X E -7
foot	meter (m)	3.048 000 X E -1
foot-pound-force	joule (J)	1.355 818
gallon (U.S. liquid)	meter ³ (m ³)	3.785 412 X E -3
inch	meter (m)	2.540 000 X E -2
jerk	joule (J)	1.000 000 X E +9
joule/kilogram (J/kg) (radiation dose absorbed)	Gray (Gy)**	1.000 000
kilotons	terajoules	4.183
kip (1000 lbf)	newton (N)	4.448 222 X E +3
kip/inch ² (ksi)	kilo pascal (kPa)	6.894 757 X E +3
ktap	newton-second/m ² (N-s/m ²)	1.000 000 X E +2
micron	meter (m)	1.000 000 X E -6
mil	meter (m)	2.540 000 X E -5
mile (international)	meter (m)	1.609 344 X E +3
ounce	kilogram (kg)	2.834 952 X E -2
pound-force (lbf avoirdupois)	newton (N)	4.448 222
pound-force inch	newton-meter (N·m)	1.129 848 X E -1
pound-force/inch	newton/meter (N/m)	1.751 268 X E +2
pound-force/foot ²	kilo pascal (kPa)	4.788 026 X E -2
pound-force/inch ² (psi)	kilo pascal (kPa)	6.894 757
pound-mass (lbm avoirdupois)	kilogram (kg)	4.535 924 X E -1
pound-mass-foot ² (moment of inertia)	kilogram-meter ² (kg·m ²)	4.214 011 X E -2
pound-mass/foot ³	kilogram/meter ³ (kg/m ³)	1.601 846 X E +1
rad (radiation dose absorbed)	Gray (Gy)**	1.000 000 X E -2
roentgen	coulomb/kilogram (C/kg)	2.579 760 X E -4
shake	second (s)	1.000 000 X E -8
slug	kilogram (kg)	1.459 390 X E +1
torr (mm Hg, 0° C)	kilo pascal (kPa)	1.333 22 X E -1

*The becquerel (Bq) is the SI unit of radioactivity; 1 Bq = 1 event/s.

**The Gray (Gy) is the SI unit of absorbed radiation.

A more complete listing of conversions may be found in "Metric Practice Guide E 380-74," American Society for Testing and Materials.

TABLE OF CONTENTS

	<u>Page</u>
1. INTRODUCTION	9
2. TEST EQUIPMENT	12
2.1 HAFB Sled Track	12
2.2 General Test Arrangement.	12
2.3 Test Area	12
2.4 Sled.	17
2.5 Wing Model.	23
2.6 Explosives.	27
2.7 Blast-Line Pressure Measurements.	32
2.8 Wing Pressure Measurements.	32
2.9 Sled Velocity and Position Measurements	32
2.10 High Speed Photography.	33
2.11 Telemetry	33
2.12 Model Strength and Stiffness Tests.	35
2.12.1 Strength.	35
2.12.2 Deflection.	35
2.12.3 Frequencies	36
3. TEST SERIES.	39
3.1 Intercept Conditions.	39
3.2 Run 9B-A1	44
3.3 Run 9B-A2	45
3.4 Run 9B-A3	45
4. TEST DATA.	47
4.1 A/D Data Processing	47
4.2 Data Presentation	47
4.3 Accuracy of Data.	52
4.3.1 Blast-Line Transducers	52
4.3.2 Sled-Borne Transducers	54

TABLE OF CONTENTS (CONCL'D)

	<u>Page</u>
5. BLAST VARIABLES AT SLED.	55
5.1 General Procedure	55
5.2 Overpressure, Density and Velocity Time Histories . .	55
6. DISCUSSION	74
6.1 Wind Tunnel Tests	74
6.2 VIBRA-6 (Doublet Lattice) Correlation	81
6.3 Analysis of Blast Loading Histories	81
6.3.1 Intercept 9B-A1-2; $\phi = 87.6$ deg., $\Delta p_s = 2.1$ psi. .	87
6.3.2 Intercept 9B-A2-1; $\phi = 20.1$ deg., $\Delta p_s = 2.0$ psi. .	88
6.3.3 Intercept 9B-A2-2; $\phi = 90.3$ deg., $\Delta p_s = 4.0$ psi. .	89
6.3.4 Intercept 9B-A2-3; $\phi = 134.9$ deg., $\Delta p_s = 2.0$ psi. .	90
6.3.5 Intercept 9B-A3-1; $\phi = 20.1$ deg., $\Delta p_s = 3.6$ psi. .	91
7. SUMMARY OF OBSERVATIONS.	93
7.1 Effects of Blast-Induced Angle of Attack.	93
7.2 Relative Importance of Diffractive Loading.	93
7.3 Nonlinear Vortex Effects.	94
8. CONCLUSIONS.	95
REFERENCES.	96
APPENDIX A PRESSURE AND ACCELERATION TIME HISTORIES.	99
APPENDIX B DENSITY AND VELOCITY TIME HISTORIES	145

LIST OF ILLUSTRATIONS

<u>Figure</u>		<u>Page</u>
1	Schematic of Typical HAFB Blast Test Arrangement. . .	11
2	Aerial View of Test Area for Run 9B-A3	13
3	Blast Area Outline	14
4	Photograph of Blast Area	15
5	Sketch of Rear View of Sled and Ground Surface Showing Procedure for Reducing Blast Interference Effects. . .	16
6	View of Test Area Showing Blast-Line Probes.	18
7	Oblique View of Model on Sled.	20
8	Front View of Model and Sled	21
9	Side View of Sled, Model and Propulsion Rockets. . . .	22
10	Inside View of Steel Wing Section.	25
11	Outside View of Steel Wing Section	26
12	Sketch of Wing and Fuselage Model Showing Pressure Measurement Stations	28
13	View of Test Setup Showing Charges in Place.	30
14	10,000 Pound Charge.	31
15	Sled Velocity Profiles	34
16	Sample Wing Differential Pressure Time History	49
17	Sample Blast-Line Pressure Time Histories.	50
18	Sample Blast-Line Pressure Variation Produced as the Sled Passes a Blast-Line Probe	53
19	Blast Flow Conditions at the Sled for Run 9B-A1, Intercept 2	59

LIST OF ILLUSTRATIONS (CONT'D)

<u>Figure</u>		<u>Page</u>
20	Blast Flow Conditions at the Sled for Run 9B-A2, Intercept 1	62
21	Blast Flow Conditions at the Sled for Run 9B-A2, Intercept 2	65
22	Blast Flow Conditions at the Sled for Run 9B-A2, Intercept 3	68
23	Blast Flow Conditions at the Sled for Run 9B-A3, Intercept 1	71
24	Wing Details of Boeing Model and Comparison With Planform of Present Model	75
25	Isobars for Upper Surface of Boeing Model at Mach 0.85	76
26	Net Chordwise Pressure Distributions for Boeing Model at Mach 0.85.	78
27	Wing Pressures, Run 9B-A1, Intercept 2, $\phi = 87.6$ deg., $\Delta p_s = 2.1$ psi	82
28	Wing Pressures, Run 9B-A2, Intercept 2, $\phi = 90.3$ deg., $\Delta p_s = 4.0$ psi	83
29	Wing Pressures, Run 9B-A2, Intercept 1, $\phi = 20.1$ deg., $\Delta p_s = 2.0$ psi	84
30	Wing Pressures, Run 9B-A3, Intercept 1, $\phi = 20.1$ deg., $\Delta p_s = 3.6$ psi	85
31	Wing Pressures, Run 9B-A2, Intercept 3, $\phi = 134.9$ deg., $\Delta p_s = 2.0$ psi.	86
32	Blast-Line Overpressures, Run 9B-A1, Intercept 2	100
33	Blastward and Leeward Wing Pressures, Run 9B-A1, Intercept 2	104
34	Total Pressure, Run 9B-A1, Intercept 2	106
35	Wing Acceleration, Run 9B-A1, Intercept 2.	107

LIST OF ILLUSTRATIONS (CONCL'D)

<u>Figure</u>		<u>Page</u>
36	Blast-Line Overpressures, Run 9B-A2, Intercept 1. . .	108
37	Blastward and Leeward Wing Pressures, Run 9B-A2, Intercept 1.	112
38	Total Pressure, Run 9B-A2, Intercept 1.	116
39	Wing Acceleration, Run 9B-A2, Intercept 1	117
40	Blast-Line Overpressures, Run 9B-A2, Intercept 2. . .	118
41	Blastward and Leeward Wing Pressures, Run 9B-A2, Intercept 2.	119
42	Total Pressure, Run 9B-A2, Intercept 2.	123
43	Wing Acceleration, Run 9B-A2, Intercept 2	124
44	Blast-Line Overpressures, Run 9B-A2, Intercept 3. . .	125
45	Blastward and Leeward Wing Pressures, Run 9B-A2, Intercept 3.	129
46	Total Pressure, Run 9B-A2, Intercept 3.	133
47	Wing Acceleration, Run 9B-A2, Intercept 3	134
48	Blast-Line Overpressures, Run 9B-A3, Intercept 1. . .	135
49	Blastward and Leeward Wing Pressures, Run 9B-A3, Intercept 1.	139
50	Total Pressure, Run 9B-A3, Intercept 1.	142
51	Wing Acceleration, Run 9B-A3, Intercept 1	143

LIST OF TABLES

<u>Table</u>		<u>Page</u>
1	Blast-Line Stations for Runs	19
2	Basic Model Data	24
3	Distribution of Airloads Measurement Stations Over Instrumented (Upper) Wing.	29
4	Sled, Support and Model Modes.	37
5	General Sled Test Conditions	40
6	Blast Intercept Conditions	41
7	Pressure Measurements on the Wing.	42
8	Comparison of Intercept Location Estimates	43
9	Index of Test Data Figures	48

1. INTRODUCTION

Military planners have a continuing requirement for the prediction of vulnerability envelopes of aircraft due to structural response resulting from a nuclear blast wave. This requirement involves both the development of computer codes to predict these blast wave effects and the acquisition of experimental data to evaluate their degree of reliability.

Code development has been recently concerned with the VIBRA-4 and VIBRA-6 codes. The VIBRA-4 code (Reference 1) is currently used by the Air Force and others for the prediction of blast vulnerability envelopes of aircraft. Recently, it has been demonstrated that improved predictions of blast-induced wing loadings at subsonic speeds can be obtained for some flight conditions by use of doublet-lattice methods (Reference 2), and the VIBRA-6 code utilizing these methods is currently under development (References 3-5).

The objective of the program described in this report is to provide a data-base of the blast-induced wing loadings on a high-sweepback wing at high subsonic speeds and to present these data in a form convenient for evaluation of the doublet-lattice method as used in the VIBRA-6 code.

Regarding previous related work, the JANAF series of blast loading tests was conducted at Wallops Island and Edwards Air Force Base during 1961 and 1962 (Reference 6). The present program differs from the earlier tests in four important aspects. First, the quarter-chord sweepback angle is about twice that of the previous model. Secondly, the model used for the present tests was constructed in a particularly rigid manner in order to avoid structural deformations and associated response pressures as had been questioned for the earlier experimental investigations. Thirdly, a better airplane simulation was achieved by the capability for full-wing testing instead of the half wing that had to be employed previously. Finally, a better ground plane was achieved at HAFB, by means of grading and other measures to reduce track interference.

To accomplish the test purpose, a series of blast tests was made at the 50,788-ft high speed sled track at Holloman Air Force Base (HAFB), using the multiple blast intercept technique illustrated in Figure 1. As indicated in the figure, the rocket sled bearing the test model is subjected sequentially to three blast waves of different orientations produced by the sequential detonation of three charges located at different points in the test area.

Three sled runs were made at a nominal preintercept Mach number of 0.76 and Reynolds number based on mean chord of 7.0 million. The test model had a 46.80-in wing span and 18.95-in mean chord. Seven separate TNT charges were detonated, six of 1,000 pounds and one of 10,000 pounds. Test results are reported for five blastwave intercepts nominally 20, 90 and 135 degrees from head-on at overpressures of about two and four psi.

The test techniques developed and used in the three test runs are described in Section 2. The test conditions, test results and data analysis procedures are presented in Sections 3, 4 and 5, respectively. The results of the three tests are discussed in Section 6, where comparisons are made with VIBRA-6 quasi-steady blast-induced wing loadings. A summary of observations is presented in Section 7 and conclusions are presented in Section 8.

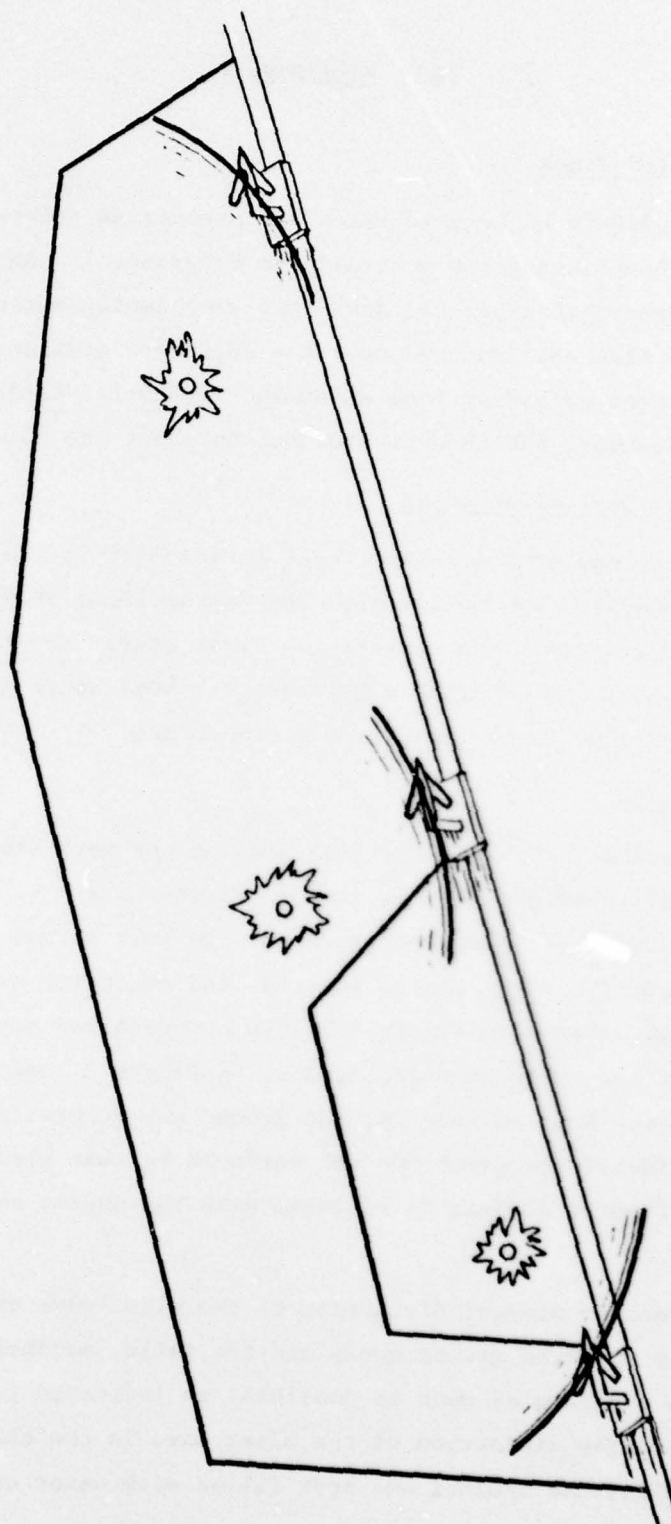


Figure 1. Schematic of Typical HAFB Blast Test Arrangement

2. TEST EQUIPMENT

2.1 HAFB Sled Track

The 50,788-ft high-speed track and associated general test equipment at HAFB are described generally in Reference 7. In the test procedure described here, the dual-rail sled employed ran from south to north. The sled was launched near the 10,500-ft station, entered the blast test area extending from about the 12,500-ft station to the 13,850-ft station, and then coasted out to about the 30,000-ft station.

2.2 General Test Arrangement

A photograph of the overall test arrangement is shown in Figure 2 (for Run 9B-A3A). The moving sled enters the field of view from the left and progressively encounters the blast waves from the detonation of several separate TNT charges placed about 6 feet above ground level at various locations on the west side of the track.

2.3 Test Area

The ground surface in the test area on the west side of the track was generally composed as indicated in Figures 3 and 4. The test area extended 1,250 feet along the track and 320 feet normal to the track. The area near the first charge location and extending almost to the edge of the track, Area I in Figure 3, had a concrete and asphalt surface. The rest of the surfaced area, Area II in Figure 3, had a basecoat and dirt surface. West of Area II, the ground was generally gypsum sand. The east side of the track was not surfaced but was graded for a lateral distance of about 20 feet to be level with the rails, as indicated in Figure 5.

In order to prevent distortion of the blast wave by gaps existing between the surfaced ground areas and the rails, sandbags were inserted to fill in the gaps as much as possible, as indicated in Figure 5. Also to minimize distortion of the blast wave in the channel between the two rails, the channel was kept filled with water during test runs, as indicated in Figure 5.

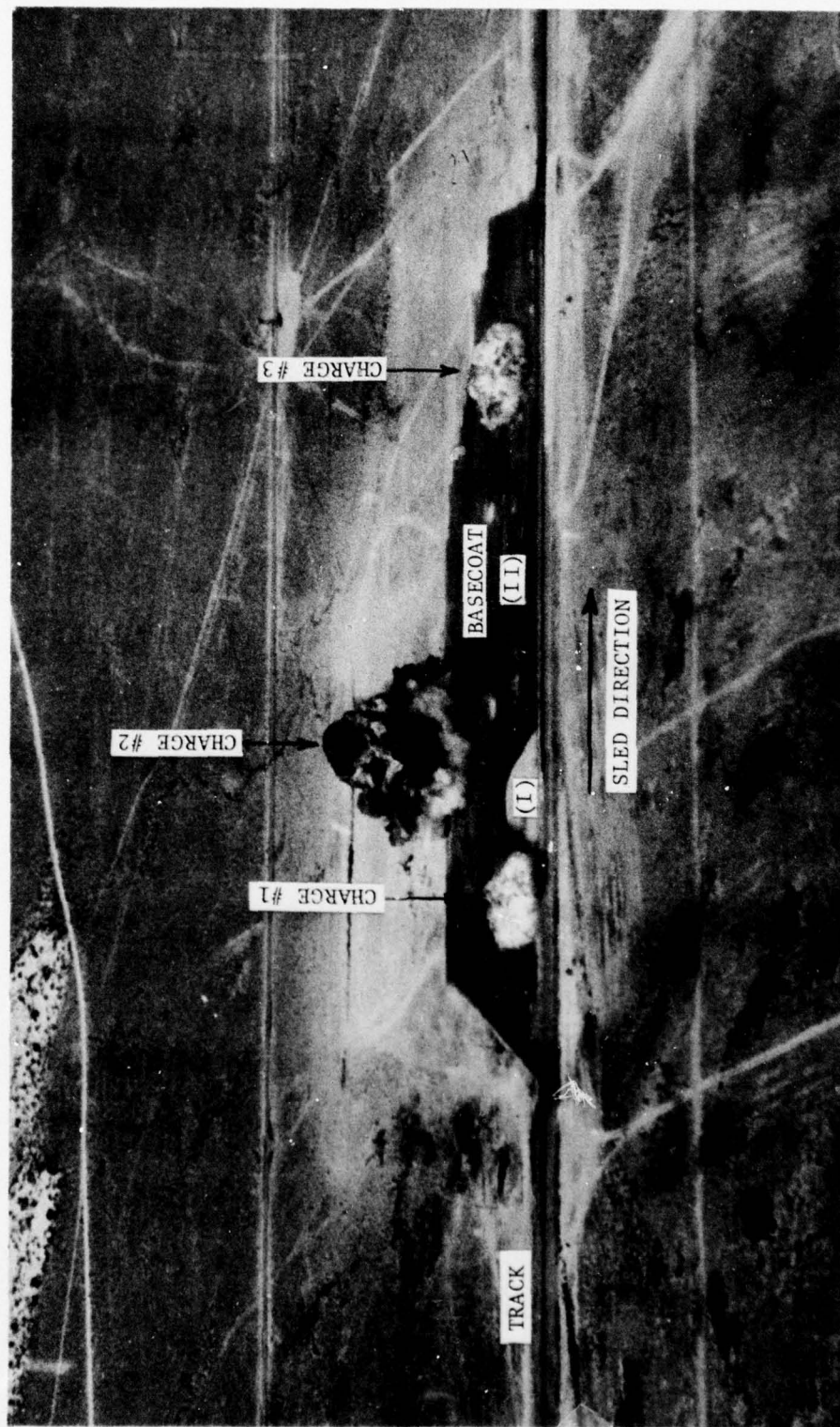


Figure 2. Aerial View of Test Area for Run 9B-A3

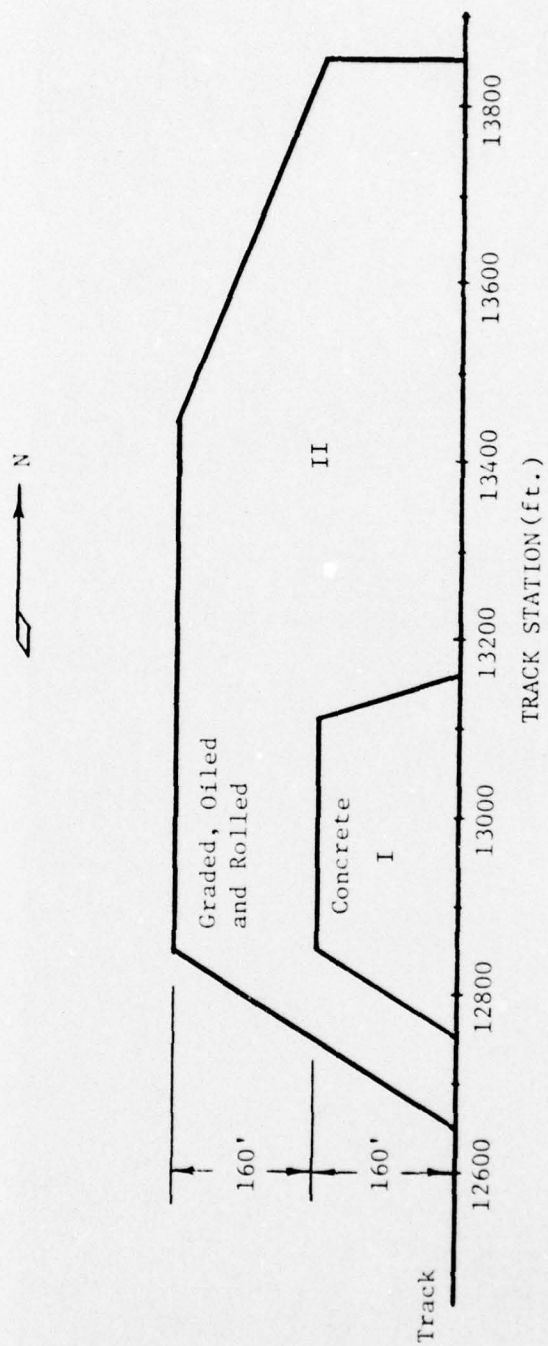


Figure 3. Blast Area Outline



Figure 4. Photograph of Blast Area

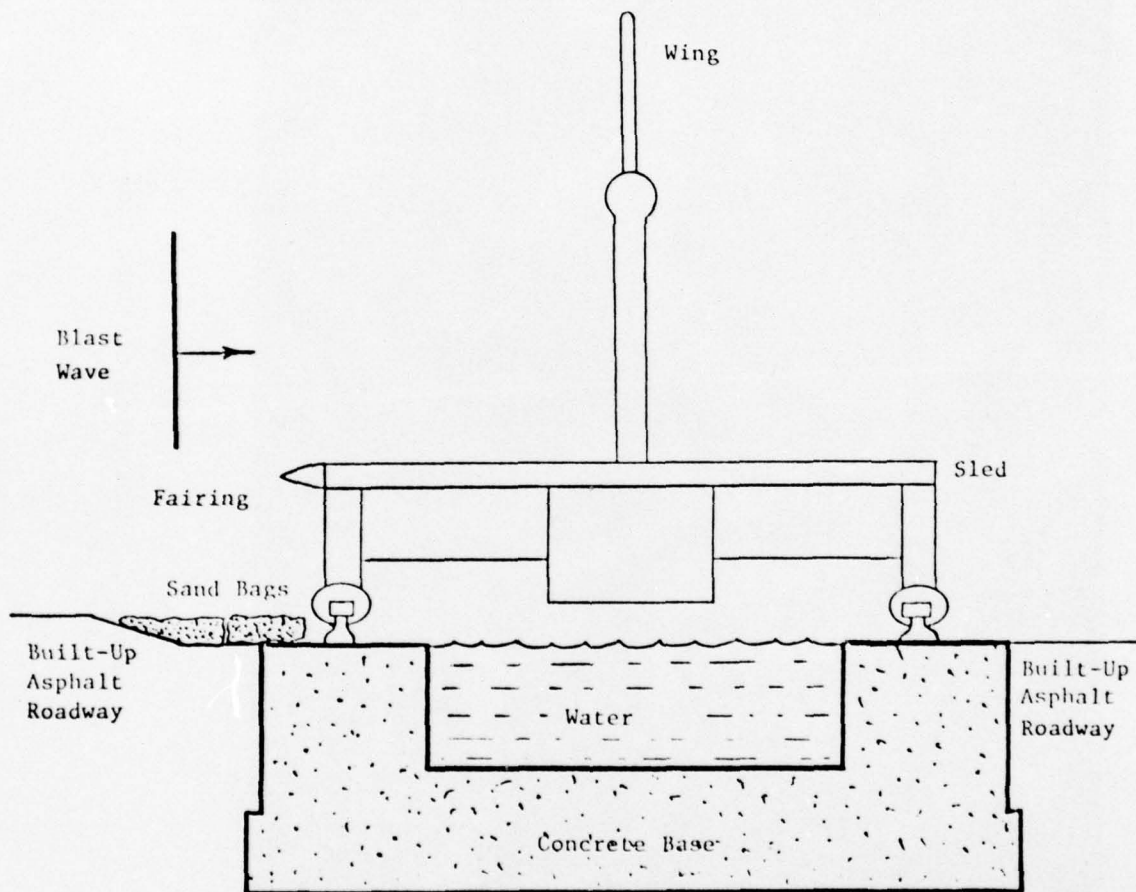


Figure 5. Sketch of Rear View of Sled and Ground Surface Showing Procedures for Reducing Blast Interference Effects

Four blast-line pressure probes were used to define the free-air blast profile for each of the three intercepts for each run, as can be seen for one location in Figure 6. The locations of the vertical struts supporting these pressures transducers (see Figure 6), designated 1 to 12, in terms of track station (distance parallel to track) are given in Table 1. All struts were located laterally (perpendicular to track) 7.5 feet west of the track centerline. All transducers were located approximately 18 inches closer to the corresponding charge location than the supporting strut.

Breakwires across the west rail were used to trigger the explosive firings and to provide a common time reference signal for checking time correlation of different recorders. These breakwires were stretched out across a rail at specified stations. They served as links in an electrical circuit, which was broken by the leading edge of the forward left slipper of the sled. The trigger breakwires were located between about 80 and 150 feet ahead of the desired intercept point (DIP) and the time reference breakwires were located 50 feet ahead of the DIP.

Several grid boards with diagonal stripes were placed in the blast area to serve as backgrounds for photographic studies of sled and blast wave motions. A typical grid board can be seen in Figure 6.

2.4 Sled

A modified HAFB dual rail rocket sled, designated as FDN 6326, was employed in these tests.

Photographs of the sled and associated propulsion rocket motors are presented in Figures 7 to 9, which present oblique, front and side views, respectively, of the sled. The top surface of the sled is basically a thick blunt flat plate whose front and blastward edges are faired to minimize sled drag and distortion of the blast wave striking the model due to interference with the sides and lower parts of the sled structure.

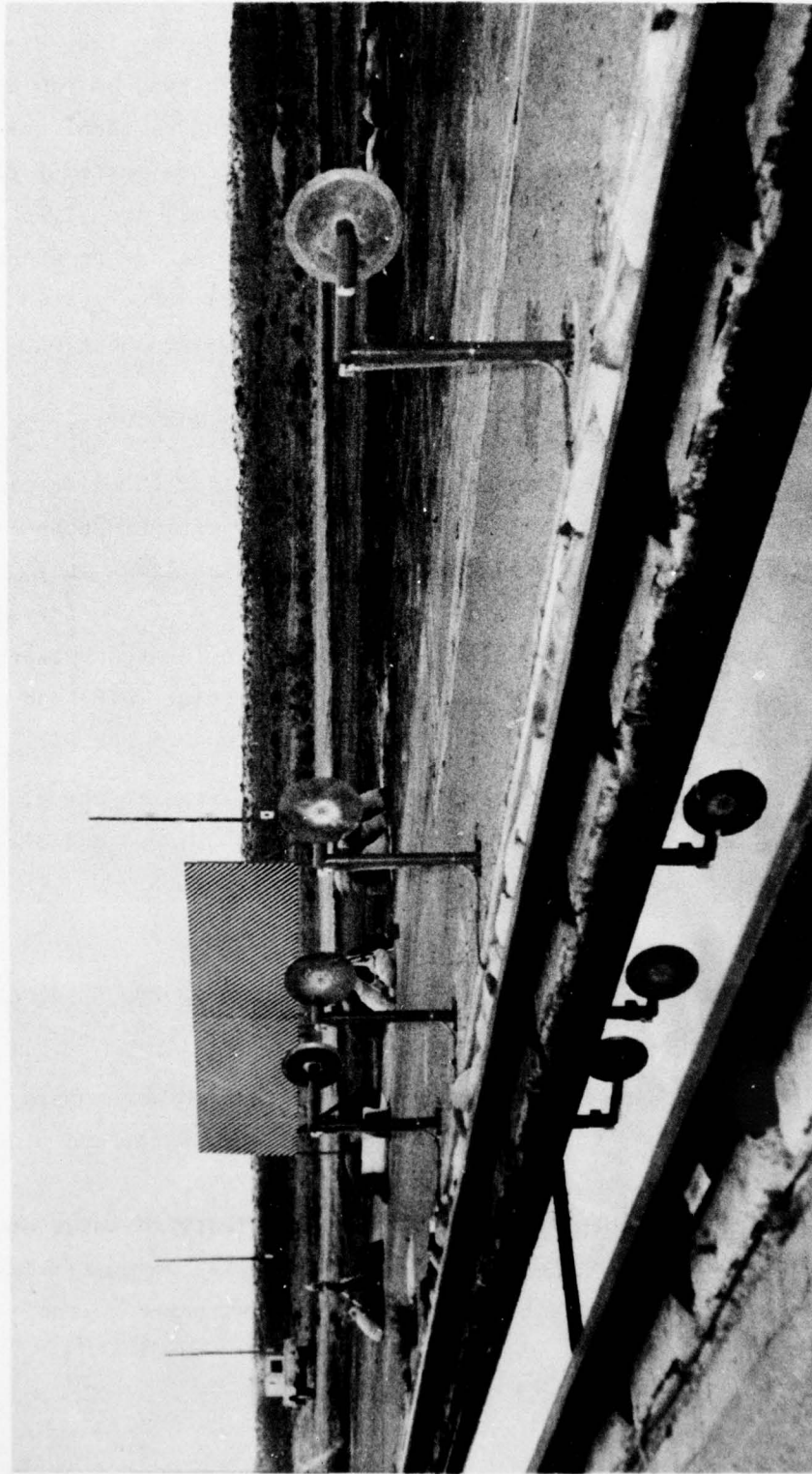


Figure 6. View of Test Area Showing Blast-Line Probes

TABLE 1
BLAST-LINE STATIONS FOR RUNS
(Location of Blast-Line Probe Mount)

Intercept Station No.	TRACK STATION*					
	RUN 1		RUN 2		RUN 3	
	DIP	Mounts	DIP	Mounts	DIP	Mounts
1	12730	12746.9 12752.6 12758.9 12772.0	12730	12746.9 12752.6 12758.9 12772.0	12730	12746.9 12752.6 12758.9 12772.0
2	13180	13171.9 13187.9 13202.7 13225.7	13180	13171.9 13187.9 13202.7 13225.7	13153	13133.9 13171.9 13202.7 13251.1
3	13630	13608.0 13636.6 13668.1 13713.1	13630	13608.0 13636.6 13668.1 13713.1	13730	13713.1 13738.3 13768.1 13813.5

DIP = Desired Intercept Point

*All mount poles are located 4 feet west of west rail (7.5 feet west of track centerline)

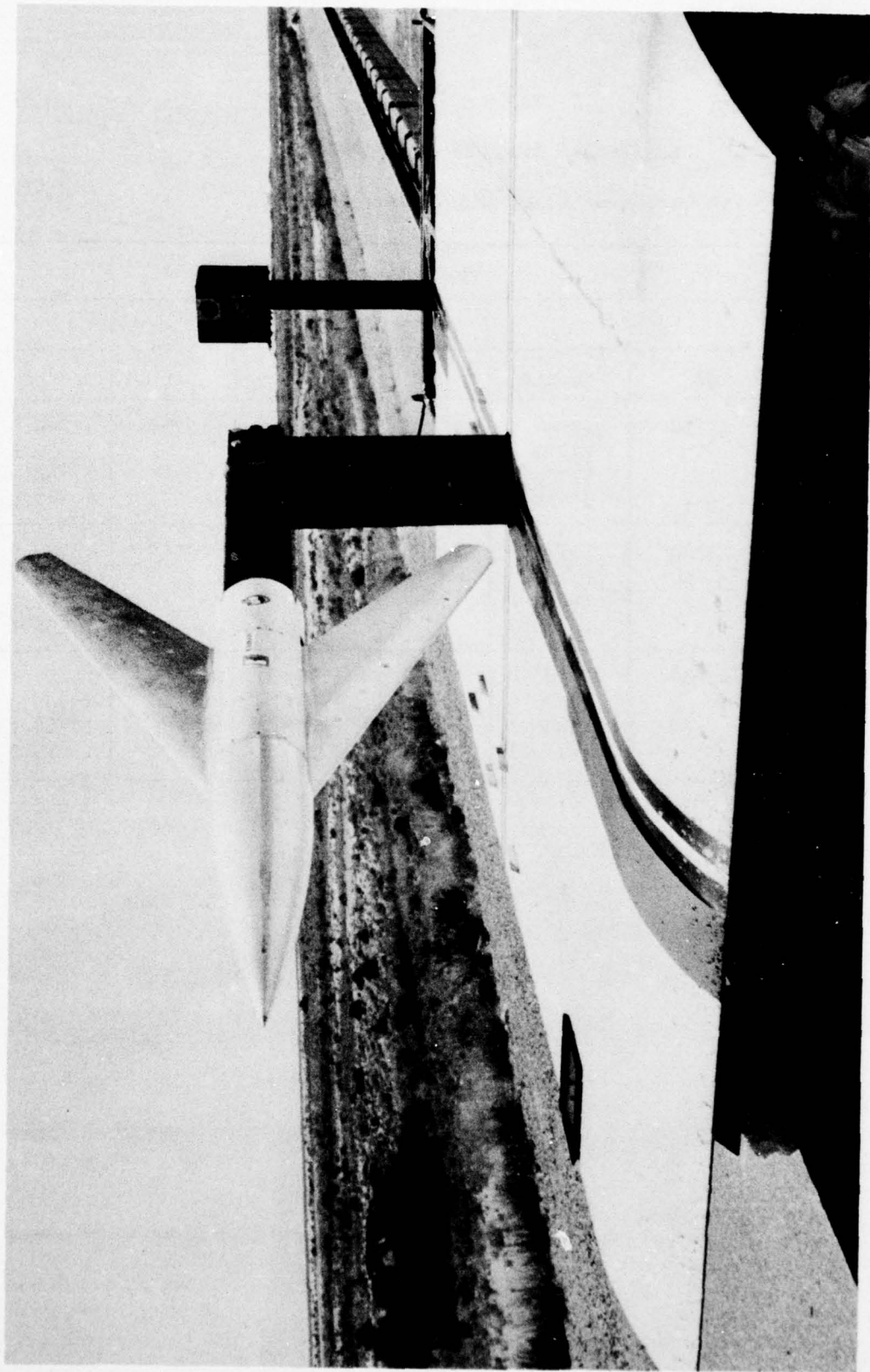


Figure 7. Oblique View of Model on Sled

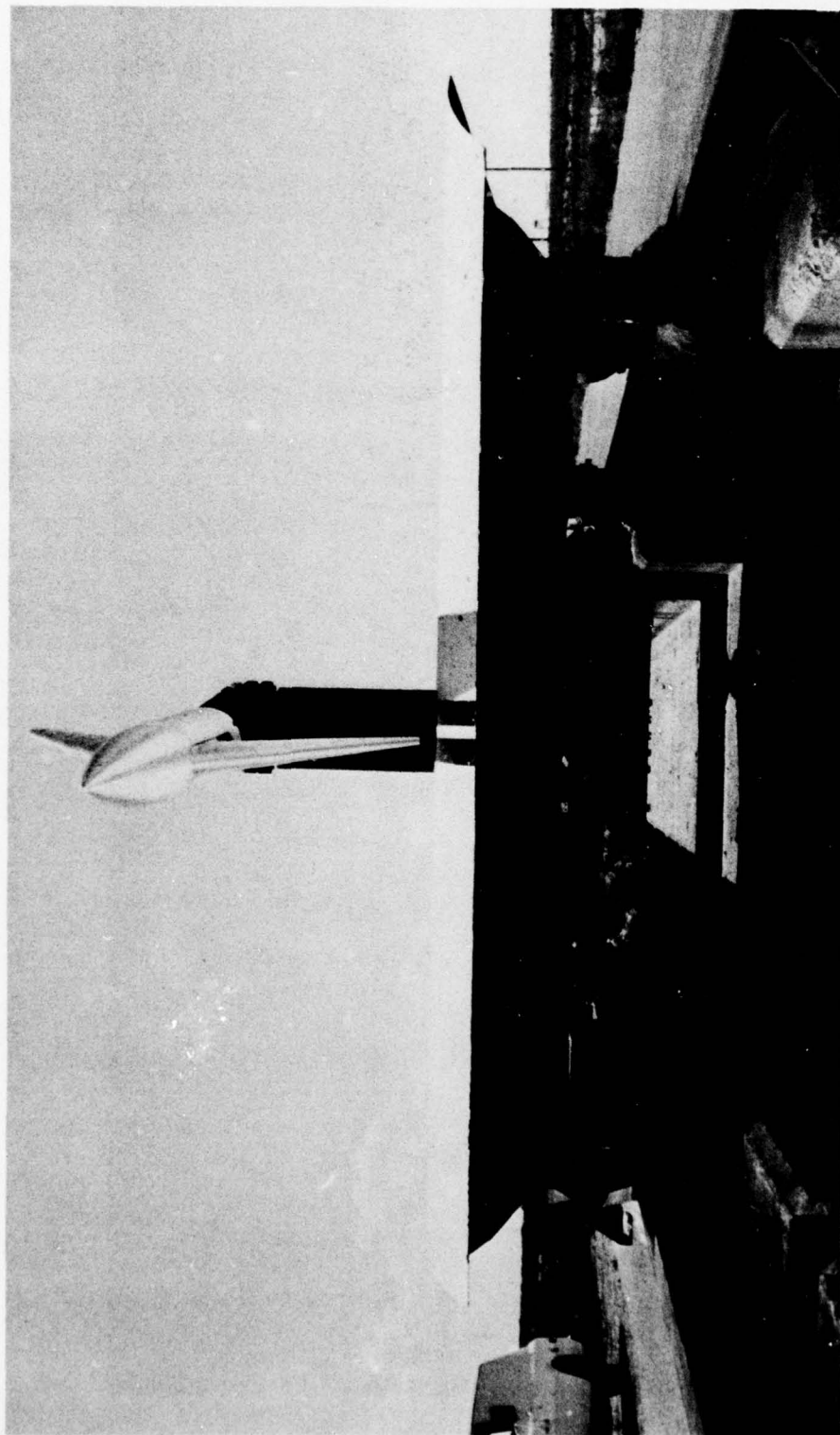


Figure 8. Front View of Model and Sled

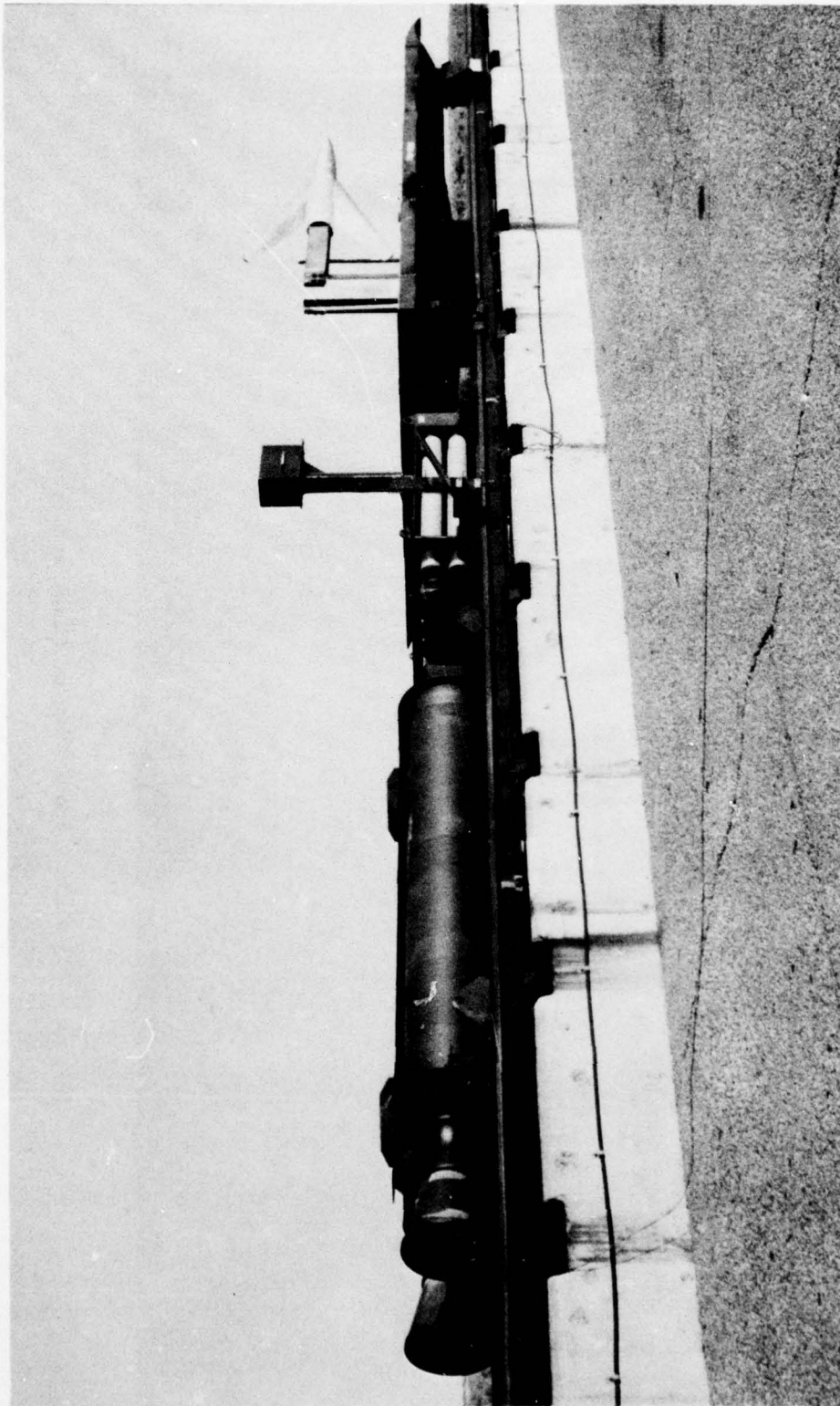


Figure 9. Side View of Sled, Model and Propulsion Rockets

The test model is mounted on the front of the sled by the vertical strut and horizontal sting attachment seen in Figures 7 and 9.

A pair of cameras aimed at the upper wing half are mounted on the sled bed in a box behind the model, as indicated in Figures 7 and 9.

The propulsion systems used to drive the sled are shown in Figure 9. The first stage propulsion unit, used to accelerate the sled to about Mach 0.6, is a separate pusher sled, not attached to the test sled, which is powered by two Nike rockets. In addition, there is another short rocket sled unit consisting of 23 HVAR rockets, which is attached behind the test sled. Eighteen of the HVAR rockets are fired after burnout of the Nike rockets to bring the test sled up to test velocity and the remainder to maintain constant speed during the test period. For all test intercepts, the sled speed after blast intercept did not vary more than about 4 fps from the intercept speed during the next 100 feet of travel, which is about the maximum distance of interest.

2.5 Wing Model

The test model consisted of a swept wing model with a nose and partial fuselage section, sting-mounted to the sled as shown in Figure 7. The model wing planform, fuselage and nose sections were constructed to simulate the basic features of the B-1 aircraft in its most sweptback position at 1/20 of full scale dimensions. Basic model data are listed in Table 2 and details are given in Reference 8. Wing leading and trailing edge sweepback angles were 67° and 55° , respectively. The wing cross section (streamwise) was made up as a 64A012 symmetrical airfoil.

The wing was mounted at an angle of attack of 3.2° , in a direction such that the pre-blast steady-state lift force was in the same direction as the blast-induced force.

The right (lower) and left (upper) halves of the wing were built up from separate solid upper-surface and lower-surface sections, see Figures 10 and 11. The sections were profile milled using a numerically controlled mill and were bolted together to assemble the total wing halves. Alignment between the sections was maintained by precision integral rings. One wing half, the upper half in Figures 7 to 9, was machined from Fremax 45 steel with wiring channels and holes for

TABLE 2
BASIC MODEL DATA

Wing Span, b	46.80 in.
Wing Planform Area, S	6.16 ft ²
Aspect Ratio	2.47
Taper Ratio	0.29
Leading-Edge Sweepback	67.0 deg.
Quarter-Chord Sweepback	64.8 deg.
Trailing-Edge Sweepback	55.0 deg.
Mean Chord (S/b)	18.95 in.
Root Chord (at model centerline)	30.60 in.
Wing Section (streamwise)	64A012
Thickness Ratio (streamwise)	12%
Pressure Stations (Two transducers per station)	20
Fuselage Diameter	8 in.

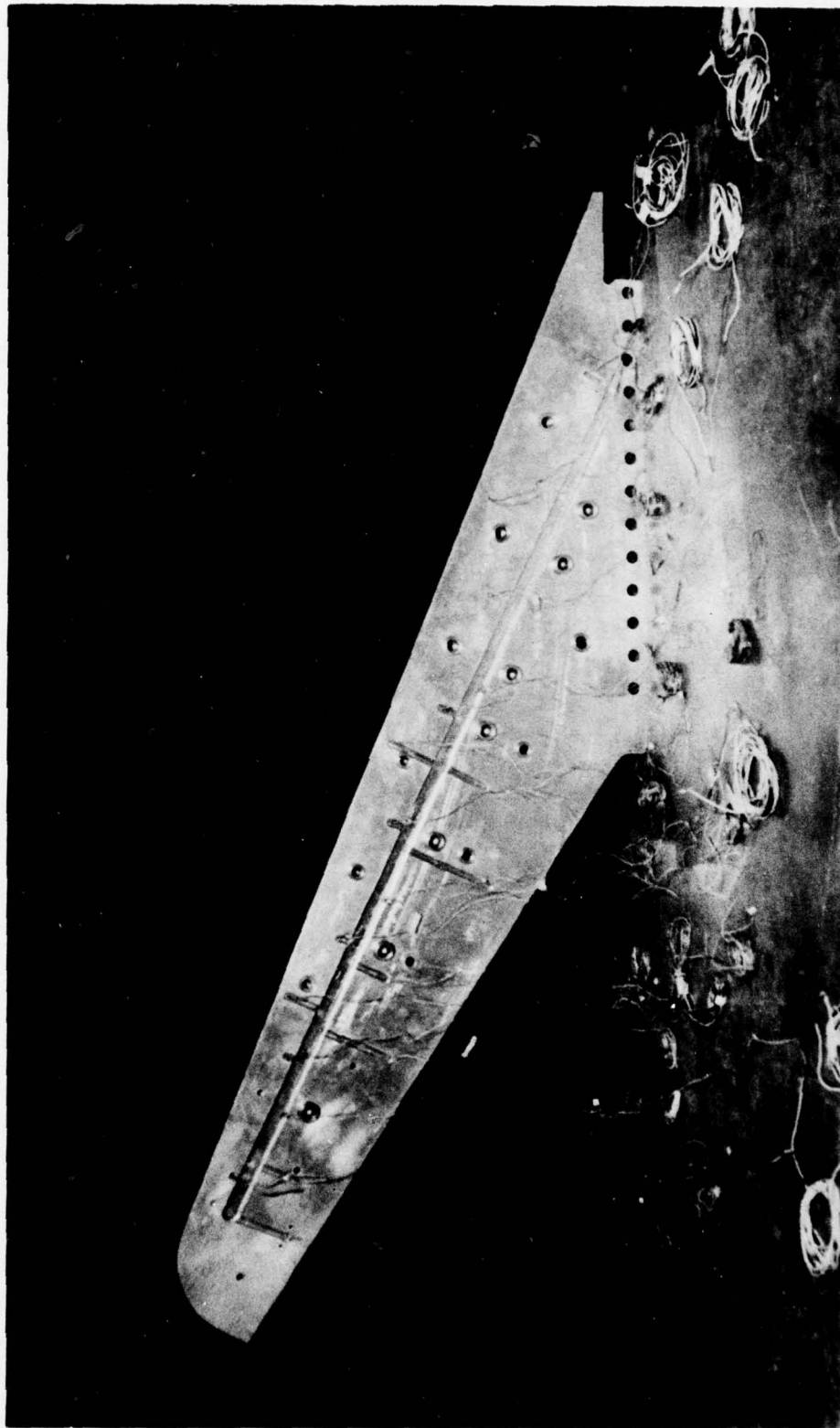


Figure 10. Inside View of Steel Wing Section



Figure 11. Outside View of Steel Wing Section

installation of 20 pairs of pressure transducers. The other wing half was similarly machined from 7075-T651 aluminum with no instrumentation installations.

The instrumented left wing half was constructed of steel in order to minimize pressure transients associated with wing elastic structural deformations produced by the blast forces. The other uninstrumented wing half was intended mainly to assure reasonable aerodynamic symmetry on the overall aircraft wing model and did not require a rigid steel construction.

Holes for twenty wing transducer locations were located as indicated in Figure 12 and Table 3. Two transducers were installed for each location to measure pressure differences between wing blast and leeward surfaces. Also provision was made for one pressure transducer being located at the nose-tip of the fuselage for measurement of total pressure at the sled. An accelerometer was mounted inside the left wing half near the 90 percent semi-span location for measurement of wing motion normal to the wing plane.

2.6 Explosives

The explosives used for each firing consisted of either 1,000 or 10,000-lb charges of TNT.

Each 1,000-lb charge was cast as a single spherical ball with an integral detonator well. Each charge was mounted with its center about 6 ft. above the ground level, sitting on top of a five foot high styrofoam pillar, as shown in Figure 13. These charges were held by straps to the ground where necessary to avoid the possibility of preceding detonations knocking the charges off their pedestals. Below each styrofoam support was either a 3 or 6 in-thick 8 ft-wide steel plate (for intercepts 1 and 3) or a 1 1/2-in base of 8 x 8-ft plywood sheets (for intercept 2).

The 10,000-lb charge was prepared by the Canadian Research Establishment, Suffolk. It consisted primarily of 306 4-in. x 1-ft. x 1 ft., 32.5-lb TNT blocks, plus a 16 in-dia hemispherical, 62.5-lb booster stacked on a 1.5 in-thick 8 x 8-ft plywood support as shown in Figure 14.

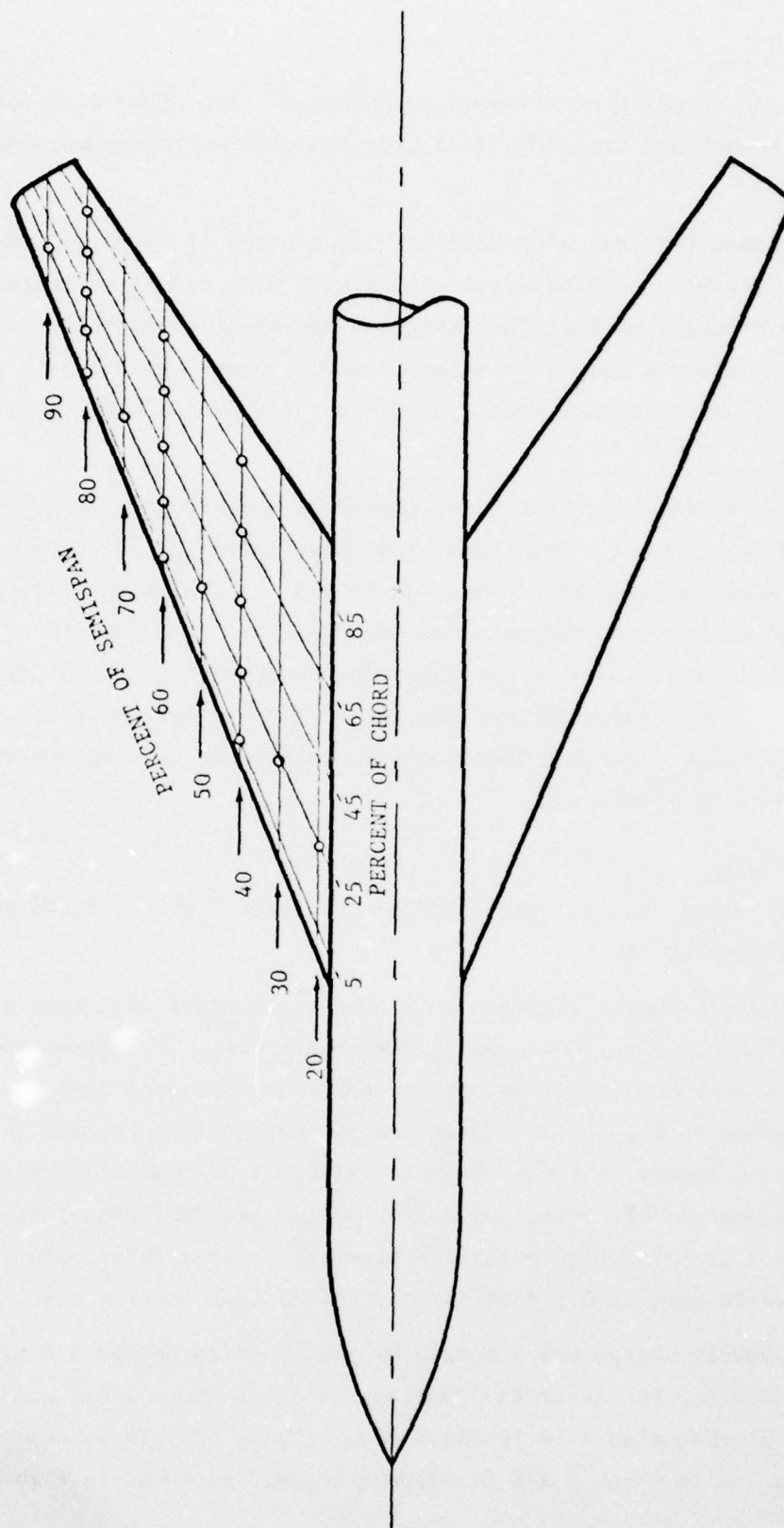


Figure 12. Sketch of Wing and Fuselage Model Showing Pressure Measurement Stations

TABLE 3

DISTRIBUTION OF AIRLOADS MEASUREMENT STATIONS OVER INSTRUMENTED (UPPER) WING

Spanwise Locations (Percent of Semispan)	Chordwise Locations (Percent of Local Chord)				
	0.05	0.25	0.45	0.65	0.85
20		X			
30		X			
40	X	X	X	X	X
50		X			
60	X	X	X	X	X
70		X			
80	X	X	X	X	X
90		X			

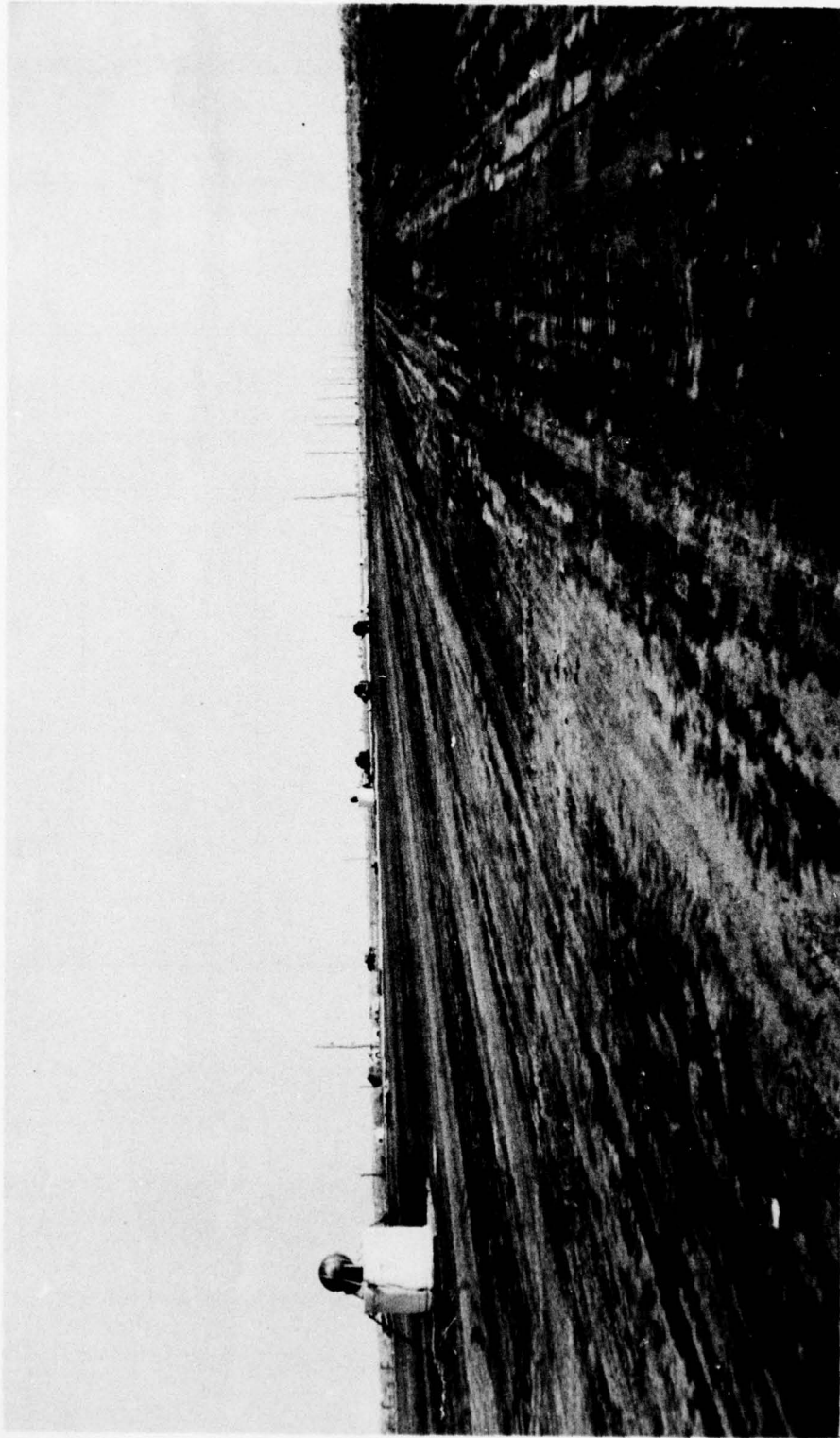


Figure 13. View of Test Setup Showing Charges in Place



Figure 14. 10,000 Pound Charge

The explosives were detonated by modified portable Reynolds Industries Exploding Bridgewire Firing Sets, using Reynolds Industries boosted RP-1 detonators.

2.7 Blast-Line Measurements

The blast-line probes employed are the standard field instruments used by BRL for the measurement of blast waves, Figure 6. The probes consist of a transducer mounted flush to the face of a circular flat disk. Each disk is beveled on the back edge around the circumference. The disks are supported by stands fabricated of 3 in-OD steel tubing, which are installed so as to be on the downstream (blast-wise) side of each disk.

Data obtained from these probes were recorded in a mobile van station on tape recorders having a frequency response of 4 kHz. The overall response time of the blast-line measurement system was about 0.2 milliseconds.

2.8 Wing Pressure Measurements

Pressures on the wing were measured using Kulite high performance pressure transducers of the XCQL-41-093-025 and XCQL-37-093-25D series. These transducers have a 25-psi range, 0.093-in diameter, low acceleration sensitivity and a 230 kHz natural frequency. All transducers were initially mounted with their surfaces flush with the wing surface, and, with a few exceptions, remained nearly flush throughout the test runs.

The transducer signals were generally connected in pairs electrically through differential amplifiers for measuring the difference in pressure between the blast-side and lee-side surfaces of the wing. The transducers were calibrated in this arrangement for matching of gains. Calibrations were carried out before and after each test.

2.9 Sled Velocity and Position Measurements

Sled position and velocity were measured with the standard HAFB VMS system. This system consists of a sled-borne photocell circuit which is interrupted generally at 13 foot intervals along the track

by ground-based bars, each of which produces a signal at the sled which is telemetered to a ground recorder station. This basic time-distance record is computer-differenced and smoothed to produce a sled velocity time history. Figure 15 presents these time histories of sled velocity in the test area for the three runs made.

In addition to the above VMS measurements, independent measurements of sled position along the track were obtained for several times from the breakwire signals used to provide firing and timing information (see Section 2.3).

2.10 High-Speed Photography

Various high-speed cameras running at speeds between 50 and 10,000 frames per second were employed in these tests. For the first intercept area of each run and the third intercept area of Run 9B-A3A, 4 x 16-ft. grid boards with parallel black and white stripes (e.g. see Fig. 6) were placed west of the track for observation of the blast shock intercept with the sled, using 10,000-fps high-speed movies. Two sled-borne 600 and 1000-fps cameras mounted in a box on the sled (Fig. 7) were used for monitoring lateral deformations of the wing model.

Various lower speed motion picture cameras were used for general surveillance of the run phenomena. Several were mounted over the track looking south for overall observation of the blast waves and sled. Additional tracking cameras, mounted on a building 1/2-mile east of the track were used for surveillance, as were also several cameras mounted in a helicopter about two miles east and 3500 feet above the track.

2.11 Telemetry

All sled-borne transducer signals were telemetered from the sled to a HAFB ground receiving station. Six transmitters were used, operating at carrier RF frequencies near 800 MHz, with 4 transducer signals generally multiplexed in each transmitter at sub-carrier frequencies of 64, 96, 128 and 160 kHz, having a frequency response of 8 kHz for each transducer signal. The overall response time of the instrumentation and telemetry system to transient pressures is estimated to be about 0.2 milliseconds.

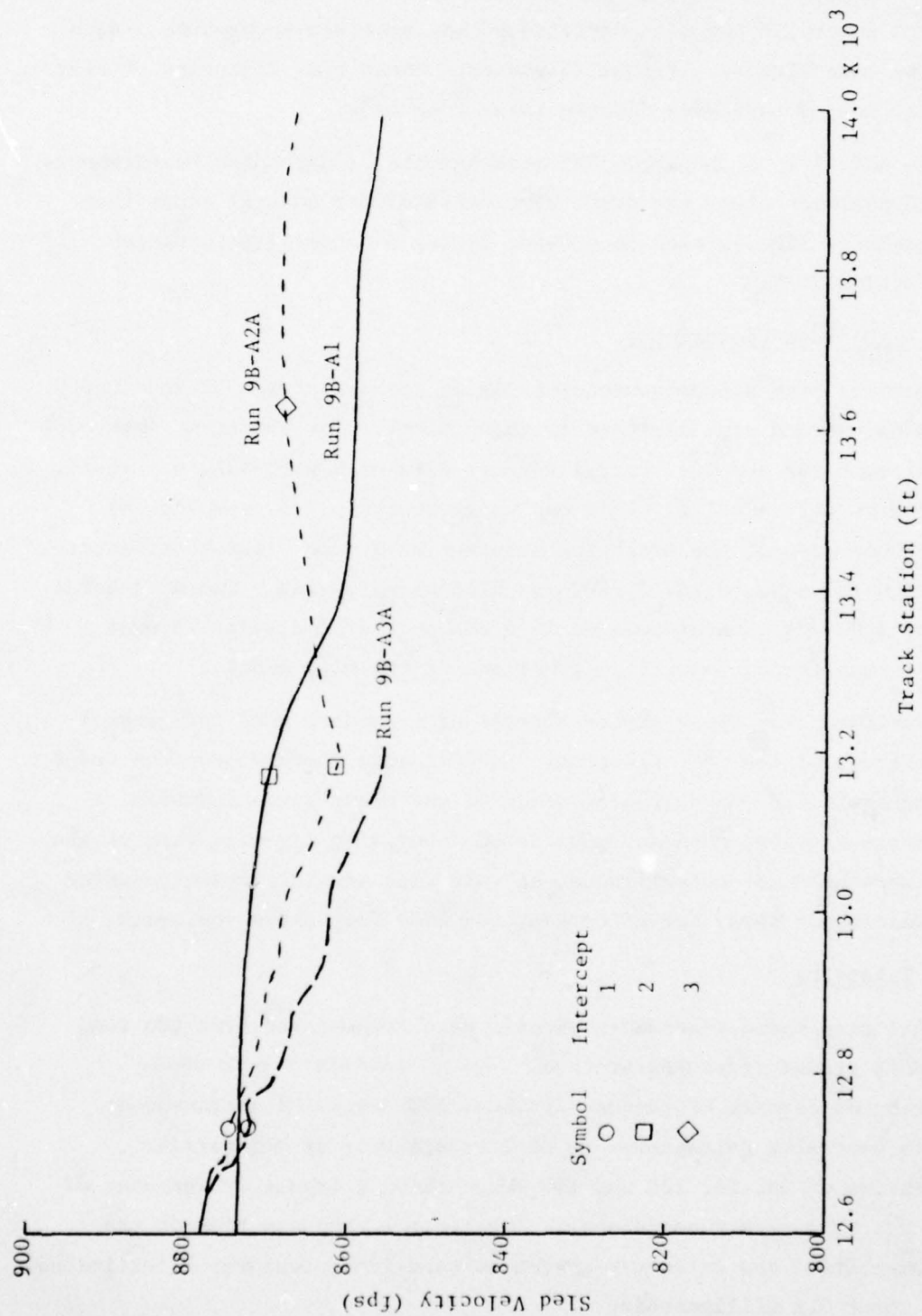


Figure 15. Sled Velocity Profiles

2.12 Model Strength and Stiffness Tests

The model and its strut-sting support were designed strengthwise to meet conservative design specifications of blast airloads. For stiffness the model and its support were designed to keep the frequencies of the wing modes and the support lateral modes well separated from the frequencies of the sled lateral modes and to keep the model deflections and motion small so the resultant airloads produced by the deflections and motion would be negligible.

Loads and vibration tests were performed on the model, model-support and sled system at HAFB during the period of May 10 to 21, 1976, prior to the test program. A test report was prepared and distributed by HAFB, Reference 9. Critical results of those tests are reviewed here.

2.12.1 Strength

The loads test of the wing indicated design goals had been met. In a loads test of the support the connector between the model and the sting deformed at about 62 percent of the design load. The connector was redesigned and the new design performed satisfactorily in the test program.

2.12.2 Deflection

Deflections of the wing, wing box and sting were measured during the loads tests. The measured deflections were compared against the predictions of the structural influence coefficient calculations performed by G. Zartarian, reported in Reference 10, and of the NASTRAN code calculations performed by D. J. Krupovage, Reference 11. In all cases the measured deflections were less than the predicted deflections.

The predicted peak incidence (angle of attack) increment of the upper wing tip by Reference 10 due to elastic deflection of the wing and support from the blast loading is only 5.5 percent of the 17.3-deg. angle of attack resulting from the design specification for the blast flow. In other words, the peak "noise" airload at the wing tip due to elastic deflection of the wing and support would be only 5.5 percent

of the peak quasi-steady airloads due to the blast. This is a conservative estimate because the wing deflection calculation was based on conservative (high) estimates of the blast airloads. Furthermore, the deflections are a maximum at the tip.

The predicted motion at the wing tip by Reference 10 due to blast-induced elastic motion of the wing and support would be only 1.6 percent of the peak blast flow of 332 fps. This means the elastic motion of the wing would contribute less than one percent to the relative velocity between the blast flow and the wing, which is negligible.

The wing incidence and motion due to elastic effects are therefore small. The deflections measured in the loads tests included deflections of the sled, support and model and the loads used are believed to be conservative, so the rigidity of the test article, support and sled are deemed quite adequate.

2.12.3 Frequencies

Shake tests were performed with the sled mounted in rails in the laboratory. The shaker force was applied in a lateral direction relative to the track. The lowest eleven frequencies measured in the tests are listed in Table 4. The measured frequencies are compared there with the NASTRAN predictions of Reference 11. In general the agreement is good.

The first three modes listed are sled modes. The first and third modes at 18.91 and 24.65 Hz are vertical motions of the sled, so they are not important to the present purposes. Mode 2 at 22.33 Hz is purely lateral motion of the longerons, resulting in essentially no lateral coupling with the model and support. The fourth mode with a frequency of 26.65 Hz does couple lateral bending of the longerons with lateral bending of the strut and sting.

Mode 5 at 34.57 Hz is a lateral motion of the bed plate of the sled which serves as a ground plane. The plate was cantilever supported by the sled substructure, and the cantilevers were weakest in the lateral direction. The sixth mode at 44.21 Hz couples strut base rocking

TABLE 4
SLED, SUPPORT AND MODEL MODES

No.	Mode Shape	Frequency Measured	NASTRAN Prediction
1	Vertical-longeron and slipper beam bending	18.91	19.11
2	Lateral-longeron bending	22.33	19.51
3	Vertical-sting bending	24.65	26.55
4	Lateral-longeron, strut and sting bending	26.65	26.61
5	Ground plane	34.57	*
6	Lateral - strut base rocking and sting bending	44.21	44.44
7	Camera pod	50.98	*
8	Sting torsion and wing bending	58.61	59.59
9	Lateral sting and wing bending	70.70	67.44
10	Pitch plane sled rocking	76.81	64.26
11	Lateral wing and model-sting connector bending	79.84	72.88

* Not modelled in NASTRAN calculation.

on the sled longerons with sting bending. The seventh mode at 50.98 Hz is essentially a pure mode of the camera support pod at the rear of the sled.

Mode 8 at 58.61 Hz is essentially sting torsion and bending of the wing. This appears to be the lowest wing elastic mode. Mode 9 at 70.70 Hz. is primarily lateral sting and wing bending. The tenth mode at 76.81 Hz is sled rocking in the pitch plane, so it is not important to this program. The eleventh mode at 79.84 Hz is bending at the sting-model connector and wing bending.

3. TEST SERIES

3.1 Intercept Conditions

The test conditions for the runs and intercepts are tabulated in Tables 5 and 6. Table 5 gives general sled test conditions for each run, including atmospheric pressure, temperature and wind conditions and the nominal sled speed. Table 6 gives specific charge and blast intercept conditions for each blast intercept, including charge weight, sled intercept velocity, charge-sled intercept geometrical relationships, blast intercept angle (ϕ), incident blast intercept overpressure (Δp_s), and the peak angle of attack produced by the blast wave.

Sled-borne pressure transducer locations were the same for all runs, as given in Figure 12 and Table 3. For most locations only the differential pressures between the two surfaces of the (upper) wing were recorded. For a few locations individual pressures on the leeward or blastward side of the model were recorded as indicated in Table 7.

The reference point on the wing which is used to define the wing-blast intercept location is defined as that point where the wing 40 - percent chordline intersects the centerline of the model fuselage. The corresponding blast intercept time for this point can be easily determined from the observed blast arrival times at the two wing transducers closest to that reference point, which are at the 20 and 30 percent semispan locations.

The track station at blast intercept time for the model reference point was estimated by three essentially independent methods for each intercept, results of which are presented in Table 8.

The first estimate made (A) was based on the sled trajectory measurements described in Section 2.9 and the blast intercept time as determined by the wing pressure transducers (t_1). The second estimate (B) was based on the timing breakwire location, the sled speed, the indicated time of wire breaking and the blast intercept time t_1 . The

TABLE 5
GENERAL SLED TEST CONDITIONS

Run No.	Date	Ambient Conditions					Nominal Sled Speed	
		Pressure		Temp. (°F)	Wind		(fps)	(Mach No.)
					Dir. (deg)	Vel. (Kn)		
		(in. Hg)	(psia)					
9B-A1	7/14/76	25.43	12.44	92.0	270	8	870	0.76
9B-A2	8/3/76	26.07	12.75	81.0	265	<5	↓	↓
9B-A3	8/26/76	25.84	12.64	85.9	240	5		

TABLE 6
BLAST INTERCEPT CONDITIONS

Run No.	Intercept No.	Charge Weight (lbs)	Sled Velocity		Distance from Charge Station to Intercept Point (ft)			Intercept Angle (deg. from head-on)	Blast Shock Overpressure (psi)	Blast Peak Angle of Attack (deg)
			(fps)	(Mach)	Parallel to Track	Perpendicular to Track	Radial Distance			
9B-A1	1 ^a	1000	-	-	-	-	-	-	-	-
	2	1000	870	0.755	-10.7	257.6	257.8	87.6	2.07	11.4
	3 ^a	1000	-	-	-	-	-	-	-	-
9B-A2	1	1000	874	.767	-240.5	88.0	256.1	20.1	2.01	5.6
	2	1000	862	.756	+ 0.8	169.9	169.9	90.3	4.02	18.0
	3	1000	868	.761	+181.7	182.4	257.5	134.9	1.97	9.4
9B-A3	1	1000	872	.761	-158.7	58.0	169.0	20.1	3.56	7.0
	2 ^b	10,000	-	-	-	349.8	-	-	-	-
	3 ^b	1000	-	-	-	120.0	-	-	-	-

^aNo detonation due to defective firing system.

^bPremature detonations (test data recorded but not analyzed)

^cIn direction of sled travel.

^dIncludes pre-blast angle of attack of 3.2 deg.

TABLE 7
PRESSURE MEASUREMENTS ON THE WING

Transducer location, %semispan/%chord (Fig. 12)	Measurement recorded ^a during Run:		
	9B-A1	9B-A2	9B-A3
20/25	D,B,L	L	D
30/25	D	D,B,L	D,B,L
40/05	D	D	D
40/25	D	D	D
40/45	D	D	D
40/65	D	D	D
40/85	D	D	D, ^{b,e}
50/25	D	D	B
60/05	D	D	D
60/25	D	D? ^{b,d}	D
60/45	D	D	D
60/65	D	D	D
60/85	D	D	D
70/25	D	D	D
80/05	D	D	D
80/25	D	D	D
80/45	D	D	D
80/65	D	D	D
80/85	D? ^{b,c}	D	D
90/25	D? ^{b,c}	L	D

^aD for differential pressure, B for blastward pressure, L for leeward pressure.

^bTransducer set up to measure differential pressure, but would indicate blastward pressure only if leeward transducer fails, or vice versa.

^cBlastward transducer inoperative after run completion; operative during pre-run calibration.

^dLeeward transducer inoperative after run completion; operative during pre-run calibration.

^eLeeward transducer inoperative just before sled run.

TABLE 8
COMPARISON OF INTERCEPT LOCATION ESTIMATES

Run No.	Intercept No.	Intercept Station Estimate (ft)*				
		A	B	C	D	av
9B-A1	2	-10.1	-10.7	-11.2	-	-10.7
9B-A2	1	2.6	1.2	1.0	-	1.6
	2	1.8	0.5	0.0	-	0.8
	3	0.5	-1.0	-1.0	-	-0.5
9B-A3	1	2.0	0.7	-	-0.3	0.8

* Distance ahead of Desired Intercept Point in the direction of sled motion (see text, Sec. 3.1, for meaning of A, B, C, D designations). The Track Station for the DIP is given in Table 1.

third method (C) was based on the location of the firing breakwire, the sled speed, the time of the detonation, and the blast intercept time t_1 . For one run, 9B-A3, where one timing breakwire did not function, an alternative third estimate (D) was made from the blast-line transducer locations, the average estimated shock velocity between the transducers and the sled-blast intercept point, the time of blast arrival at the transducers, and the blast intercept time t_1 . Values of intercept conditions obtained by these three methods differ somewhat due to the associated experimental uncertainties. It is recommended that the intercept conditions presented in Table 6, based on the average values presented in Table 8, be used for any calculations relevant to the test program.

3.2 Run 9B-A1

This test was performed to obtain blast intercepts for three different intercept angles of 20° , 90° and 135° at a blast shock overpressure level of 2 psi. Weather conditions were good with the temperature 92 deg. F. and a light 8-knot wind recorded from 270 degrees which is a cross wind of 8 knots from the blast side. The second intercept in this run was successful in that the desired intercept angle and overpressure were obtained and useful data were obtained from all blast-line and wing pressure transducer locations. The sled speed at blast intercept was satisfactory, but somewhat lower than planned, Mach 0.76 compared to 0.80 planned, due to inaccuracies in pre-test estimates of the sled drag. No blast intercept data were obtained for the 20° and 135° intercept conditions since the charges for these intercepts failed to detonate, due to faulty firing systems. However, some useful data were obtained on sled interaction effects on a blast-line transducer from the blast-line transducers set up for these two intercept locations.

3.3 Run 9B-A2

This run was performed to obtain 20° and 135° blast intercept data at a 2 psi overpressure, as had been intended to be obtained in the previous run, and to obtain data for one side-on (90°) blast intercept at a 4 psi overpressure level. Weather conditions were excellent. The temperature was 81 deg. F and the wind was essentially zero. This run was successful in that all three charges detonated as scheduled, all three intercepts occurred at the scheduled intercept angles and overpressure levels, and the intercept sled speed was close to the planned value of Mach 0.76. Useful pressure data were obtained from all sled-borne pressure transducer locations and from all but three of the twelve blast-line transducers. Blast-line pressures were not obtained from three of the four blast-line transducers set up for the second intercept because one transducer experienced mechanical damage and two experienced electrical interference problems. Some pitting of the leading edge of the sled on the blast side appeared to indicate some sand and small particles were picked up by the first blast, but no damage was noted to the model.

3.4 Run 9B-A3

This test was performed to obtain blast intercepts at a 4-psi overpressure level for blast intercept angles of 20° , 90° and 135° . Weather conditions were very good. The temperature was 85.9 deg. F with only a 5-knot wind registered at 240 degrees, for a cross wind of half that. The second intercept condition was intended to be the same as that for the previous run except having a longer duration blast produced by a 10,000 lb. TNT charge as compared to 1000 lb. charges for all other intercepts.

The first intercept of this run was successful in that the desired sled speed, intercept angle and intercept pressure level were obtained

and all wing transducer locations and all blast-line pressure transducers produced useful data. No blast intercept data directly useful for the present program were obtained from the second- and third-intercept charges due to premature firing of the second and third charges, believed to have been caused by the electromagnetic pulse produced by the first detonation acting on the firing circuits for the other two charges.

In the case of the second intercept, this detonation occurred so close after the first detonation that the blast wave from the second detonation had to travel through the fireball from the first detonation, thereby causing a considerable distortion of the blast front before it reached the sled. Intercept was determined as having taken place within the fireball of the first burst.

Due to the premature firing of the third charge, the blast pressure at the third intercept was too weak to be of interest for the present program. Some useful data of sled aerodynamic interference on the blast-line probes were obtained from the blast-line transducers set up for the second and third intercepts, which proved useful in evaluation of the test results for the previous runs.

4. TEST DATA

4.1 A/D Data Processing

Six types of event data were obtained as a function of time during a run:

1. Sled position and velocity.
2. Blast-line pressure.
3. Total pressure at the model.
4. Wing pressure.
5. Wing acceleration.
6. Lateral bending moment at the sting root.

All data were processed to digital form by HAFB and were provided to KA as tabular data. In addition Items 2 to 6 were provided in graphical form and on magnetic tapes.

The sled-borne transducer data (items 2 to 6) were taken from the analog tapes at 0.1 millisecond intervals for about 20,000 times.

4.2 Data Presentation

Graphical time history plots of most of the measured blast-line and sled-borne transducer measurements are presented in this report according to the index of figures given in Table 9. Wing differential pressure time histories for each intercept are presented as composite reduced-size figures in Section 6 of this volume and also as individual page-size plots in Volume 2. A sample differential pressure time history is presented in Figure 16.

Time histories of blast-line pressures, blastward and leeward wing pressures, total pressure at the model and model acceleration are presented in Appendix A. Sample blast-line time histories are presented in Figure 17.

In all figures presenting time histories of sled transducer pressures, transducer locations are identified by a four digit code, e.g., 60/05, where the first two digits (60) give the spanwise distance from the model centerline as a percent of the semi-span (e.g., 60%) and the last two digits (05) give the percentage chordwise distance from the leading edge of the wing.

TABLE 9
INDEX OF TEST DATA FIGURES

Run Number	Intercept Number	Figure Number			
		Blast-Line Pressures	Wing Pressures Differential*	Blastward/Leeward	Total Pressure at Model Acceleration
9B-A1	2	32	27	33	34 35
9B-A2	1	36	29	37	38 39
9B-A2	2	40	28	41	42 43
9B-A2	3	44	31	45	46 47
9B-A3	1	48	30	49	50 51

*These data are also presented in Volume 2 as individual page-size time history plots for all transducers.

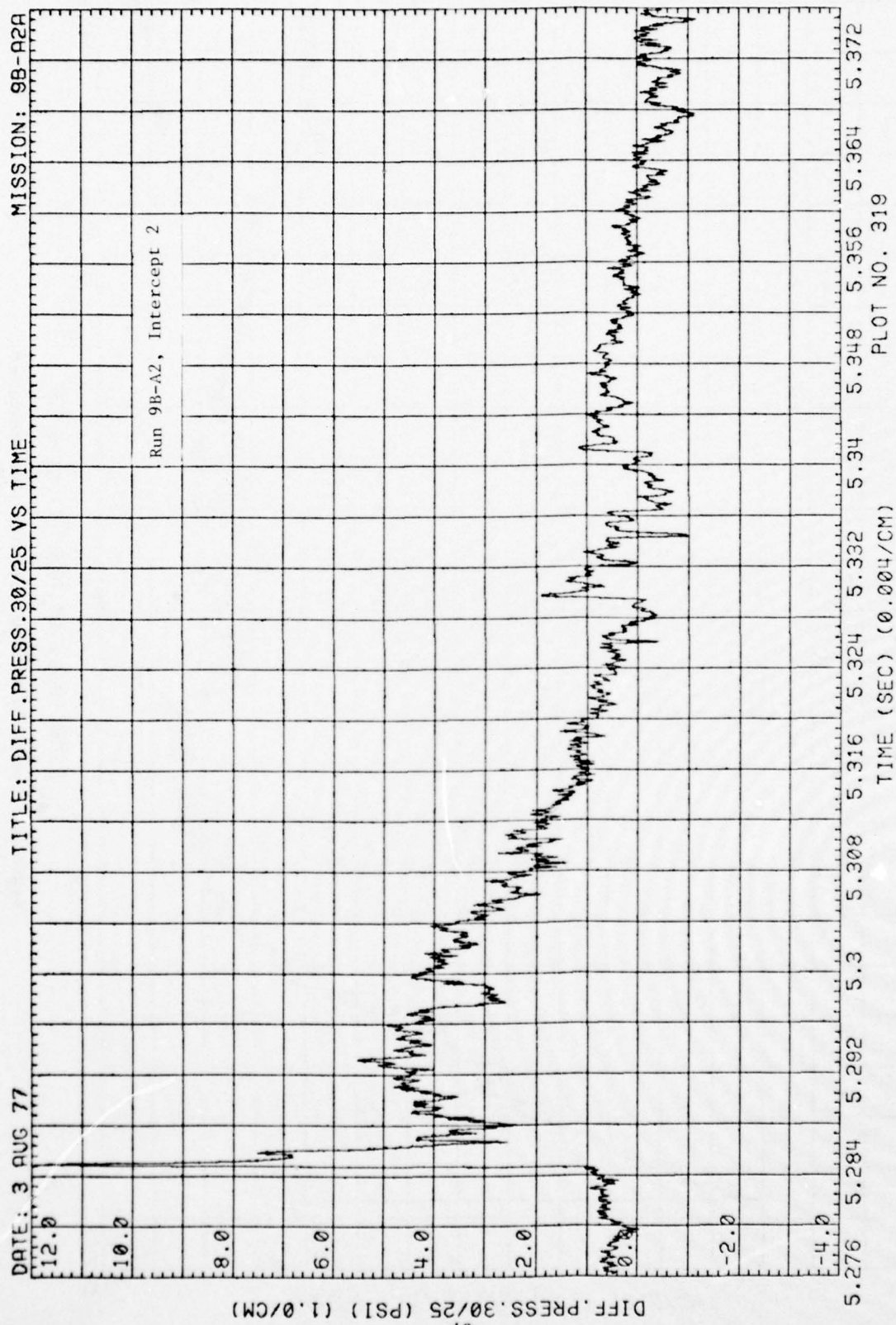


Figure 16. Sample Wing Differential Pressure Time History

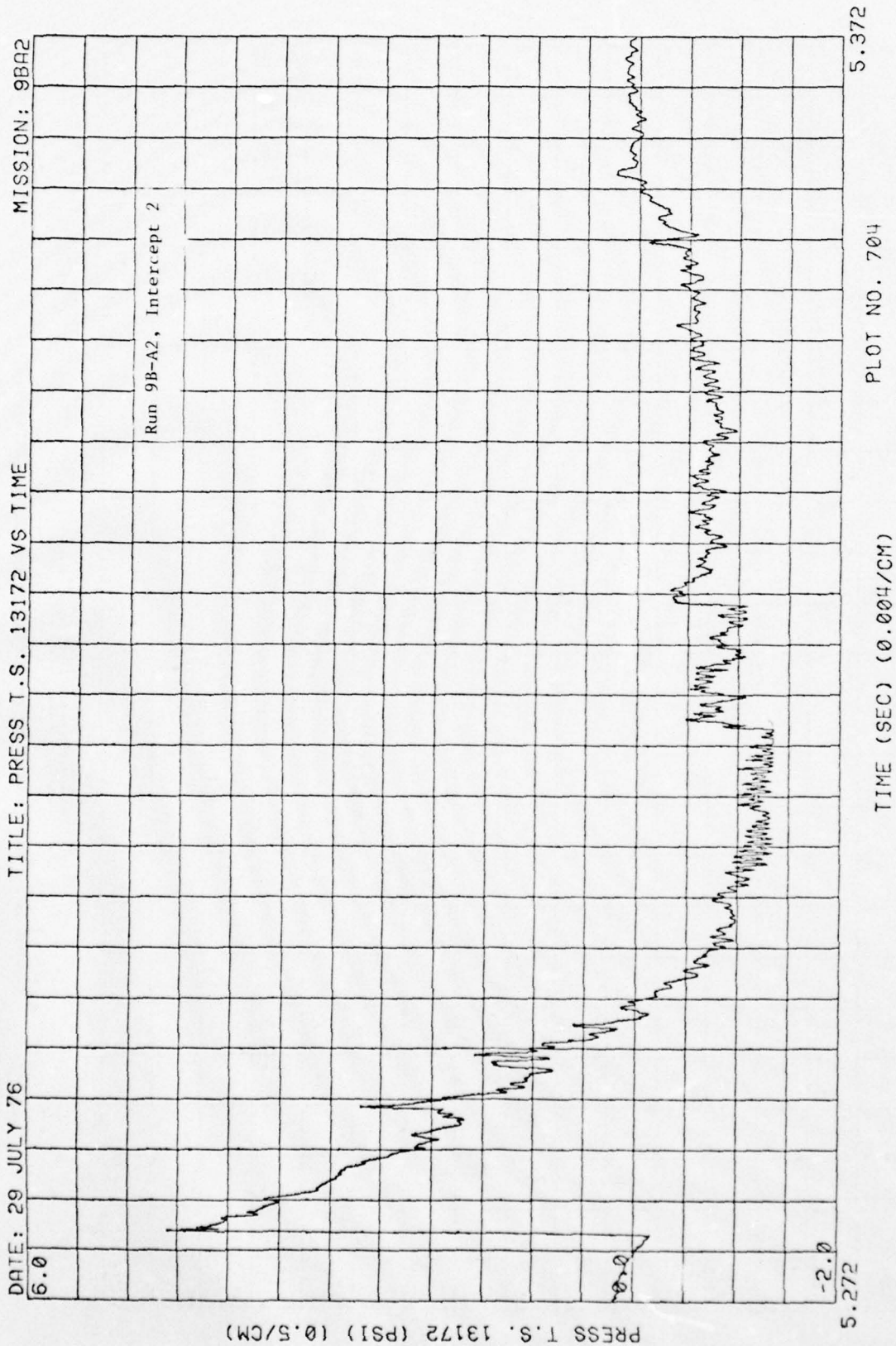


Figure 17. Sample Blast-Line Pressure Time Histories

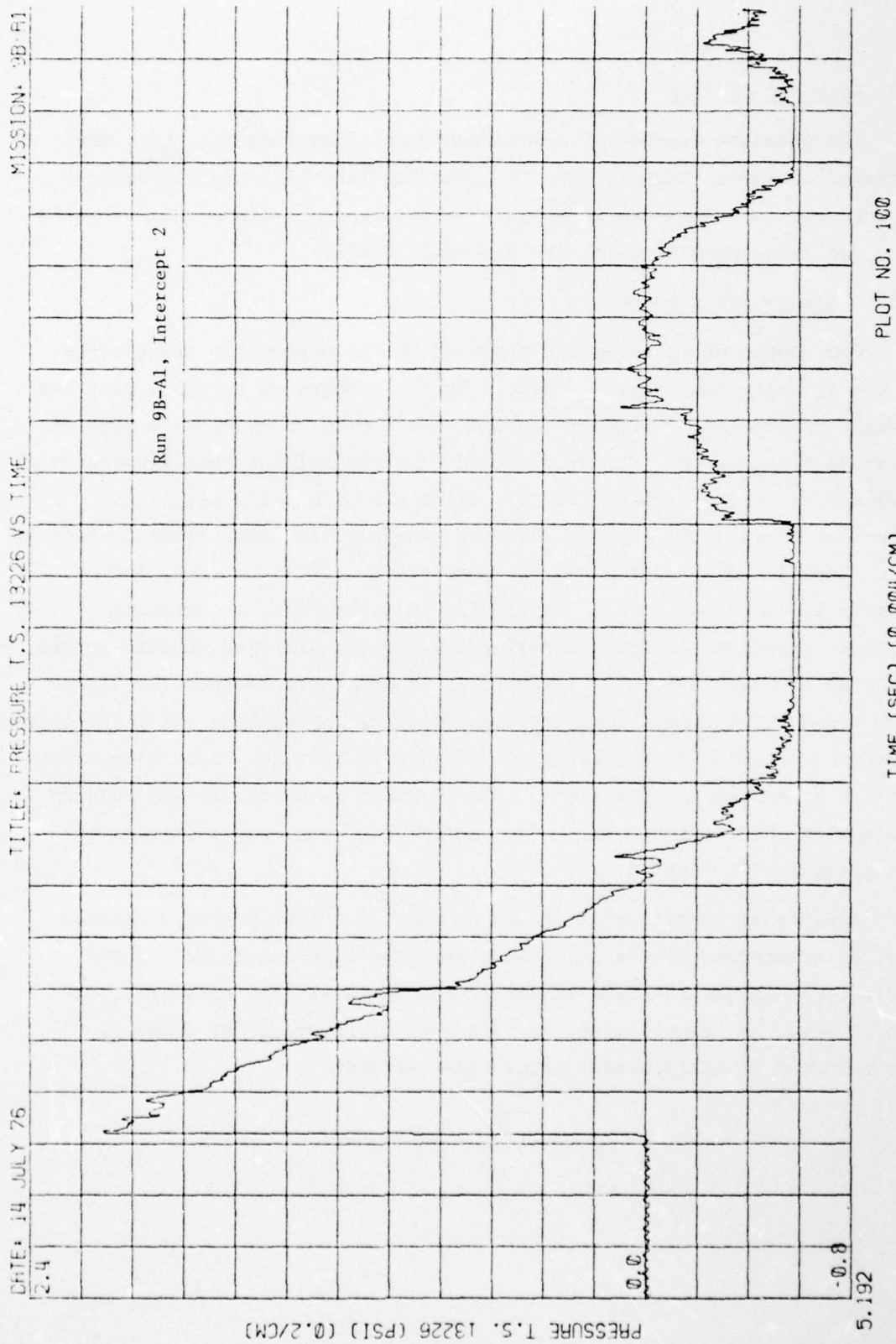


Figure 17. (Concluded)

4.3 Accuracy of Data

The pressure transducer measurements obtained from the tests are degraded at least slightly from the true "undisturbed" blast pressures at the same locations due to various interference, noise and instrumentation problems, some of which are discussed below.

4.3.1 Blast-Line Transducers

One source of interference observed on the blast-line transducers is the pressure disturbance produced by the passage of the sled past the transducer location. Figure 18 presents a typical plot of this type of pressure disturbance. It may be noted that the peak of this interference pressure can be as high as 0.5 psi, which can be significant if it occurs at the same time as the blast wave passes the blast-line transducer. This situation did occur for a few conditions, as can be seen, for example in the first part of Figure 17, where there is a noticeable pressure transient on the blast-line transducer, starting shortly before the time of blast arrival. However, it is simple to correct the blast-line pressures for this interference effect by subtracting the interference pressures obtained from records like Figure 18 from the basic blast-line data as presented in Appendix A. This correction procedure was used in estimating the blast pressure time histories at the sled as described and presented in Section 5.

Additional interference occurs on the blast line pressure records due to reflections of the blast wave from the sled and track. These reflections appear as broad spikes in the pressure time histories, as can be seen, for example, in the last part of Figure 17 at times of about 10 and 20 milliseconds after blast arrival.

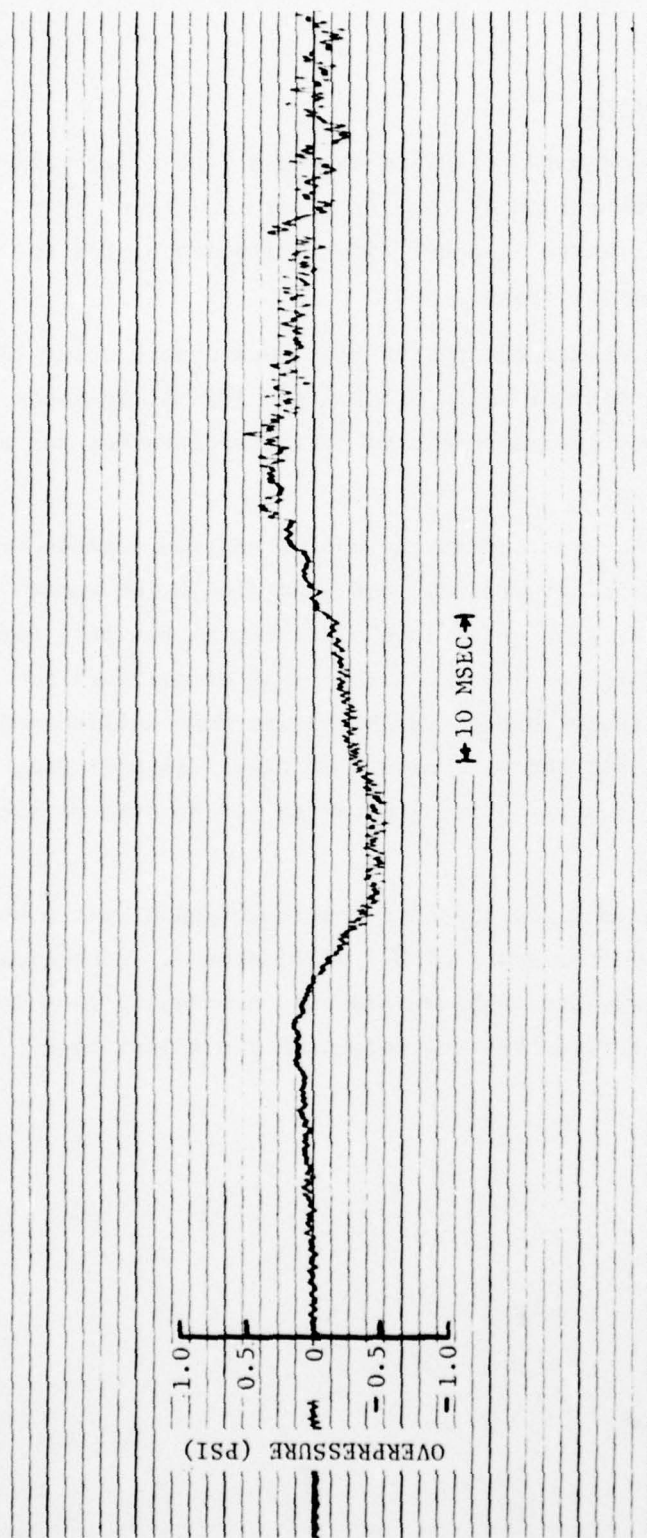


Figure 18. Sample Blast-Line Pressure Variation Produced as the Sled Passes a Blast-Line Probe

4.3.2 Sled-Borne Transducers

Degradation of the sled-borne pressure data can result from the noise level of the instrumentation system, from zero shifts of the instrumentation, from the finite response time limitation of the instrumentation, and from other causes.

Instrumentation zero shifts during the test period were observed to be small, generally being near or below 0.1 psi per 100 milliseconds of sled travel, which is about the largest time period of interest for any intercept.

The noise level on the transducers, as estimated from transducer transients observed before blast arrival, was generally below about ± 0.2 psi, but occasionally peak noise levels of about ± 0.4 psi, were encountered and a few as high as ± 0.7 psi. By peak noise level is meant here occasional pressure changes taking one or more milliseconds to occur and lasting at least the same amount of time. In addition, higher frequency noise of a more obvious character is observed on most transducer records.

As was noted in Section 2.11, the sled instrumentation system has a limiting response time on the order of 0.2 milliseconds. Consequently, the transducers are not expected to have responded accurately to a few very high frequency diffraction pressure pulses of the spiked type observed in Figure 16.

5. BLAST VARIABLES AT SLED

5.1 General Procedure

In order to utilize the blast-line pressure data presented in Appendix A for the comparison of experimental and theoretical wing pressures, it is necessary to interpolate or extrapolate the experimental blast-line pressures to obtain the blast pressure time history at the sled as a function of time, and to also estimate the corresponding blast density and velocity time histories as well. The blast pressures at the sled were obtained as indicated in Section 5.2 below and the corresponding densities and velocities were obtained by using the method described in Reference 12, as discussed in Appendix B of this report. The resulting time histories of pressure, density and velocity at the sled are presented in Section 5.2.

5.2 Overpressure, Density and Velocity Time Histories

For each blast line transducer time history, a corresponding time history of the blast overpressure at the sled was determined by assuming that the shapes of the overpressure time histories at a blast line transducer location and at the sled location are the same, if the overpressure is expressed as a fraction of the shock overpressure at the location and the time is expressed as a fraction of the positive duration of the blast wave, or

$$\Delta p / \Delta p_s = f(\Delta t / t_{\Delta p+}) \quad (1)$$

where

Δp_s is the shock overpressure

Δp is the overpressure at time t

Δt is time after shock arrival ($t - t_s$)

t is time

t_s is shock arrival time

$t_{\Delta p+}$ is the positive duration time of the overpressure, as determined theoretically from Brode's analysis (Fig. 36 of Reference 13).

$f(\Delta t/t_{\Delta p+})$ is the experimental variation of $\Delta p/\Delta p_s$ with $\Delta t/t_{\Delta p+}$ as obtained from a blast line transducer, after fairing out some obvious interference pulses and noise.

The shock overpressure corresponding to any position of the sled was interpolated or extrapolated from the corresponding blast line transducer value with the equation

$$\Delta p_s(r_r) = \Delta p_s(r_b) [\Delta p_s(r_r)^*/\Delta p_s(r_b)^*] \quad (2)$$

where

r_b designates the radius from the burst point to the blast line transducer.

r_r designates the instantaneous radius from the burst point to the model reference point, as determined from the problem geometry and the experimental sled trajectory.

$\Delta p_s(r)$ designates the shock overpressure at a point at a radial distance r from the burst.

$\Delta p_s(r_b)$ is the experimental shock overpressure at the blast line transducer

and the *'s designate theoretical values as obtained from Brode's theory (Reference 13), using the curves presented in Reference 12.

Using the above equations, overpressure time histories at the sled were calculated for each intercept for all of the blast line transducers for which useful data were obtained. Then all time histories obtained for each intercept were averaged to obtain a best estimate of the true

time history for that intercept. The following weighted average equation was used for this purpose.

$$p = \frac{w_1 p_1 + w_2 p_2 + \dots + w_n p_n}{w_1 + w_2 + \dots + w_n} \quad (3)$$

where

p is the weighted average pressure at any time

p_i is the pressure estimate from the i -th transducer

n is the number of transducers

w_i is a weighting factor given by

$$w = A(\Delta\theta) \times B \quad (5)$$

$$A(\Delta\theta) = 0.1 + 0.9 \exp(-(\Delta\theta/7.5^\circ)^2) \quad (6)$$

$$B = \exp[-20(\Delta p_{s, \text{sled}}^* / \Delta p_{s, \text{blast line}}^* - 1)^2] \quad (7)$$

$\Delta\theta$ is the circumferential angle between a ray from the burst to the blast line transducer and a ray from the burst to the sled reference point.

The factor $A(\Delta\theta)$ gives maximum weight to blast line transducers lying on a radial line between the burst and the sled and the factor B gives maximum weight to transducers located at the same radial distance from the blast as the sled. The particular expressions for these two weighting factors A and B given above, while somewhat arbitrary, were considered satisfactory since several other choices of weighting factors gave about the same end results.

The time histories of the blast overpressure at the sled obtained by the above procedure for all intercepts are shown in the first parts of Figures 19 to 23. These time histories cover the time period from initial shock arrival up to the time of second shock arrival.

The corresponding time histories of blast density and velocity, as obtained as described in Appendix B, are also presented in Figures 19 to 23.

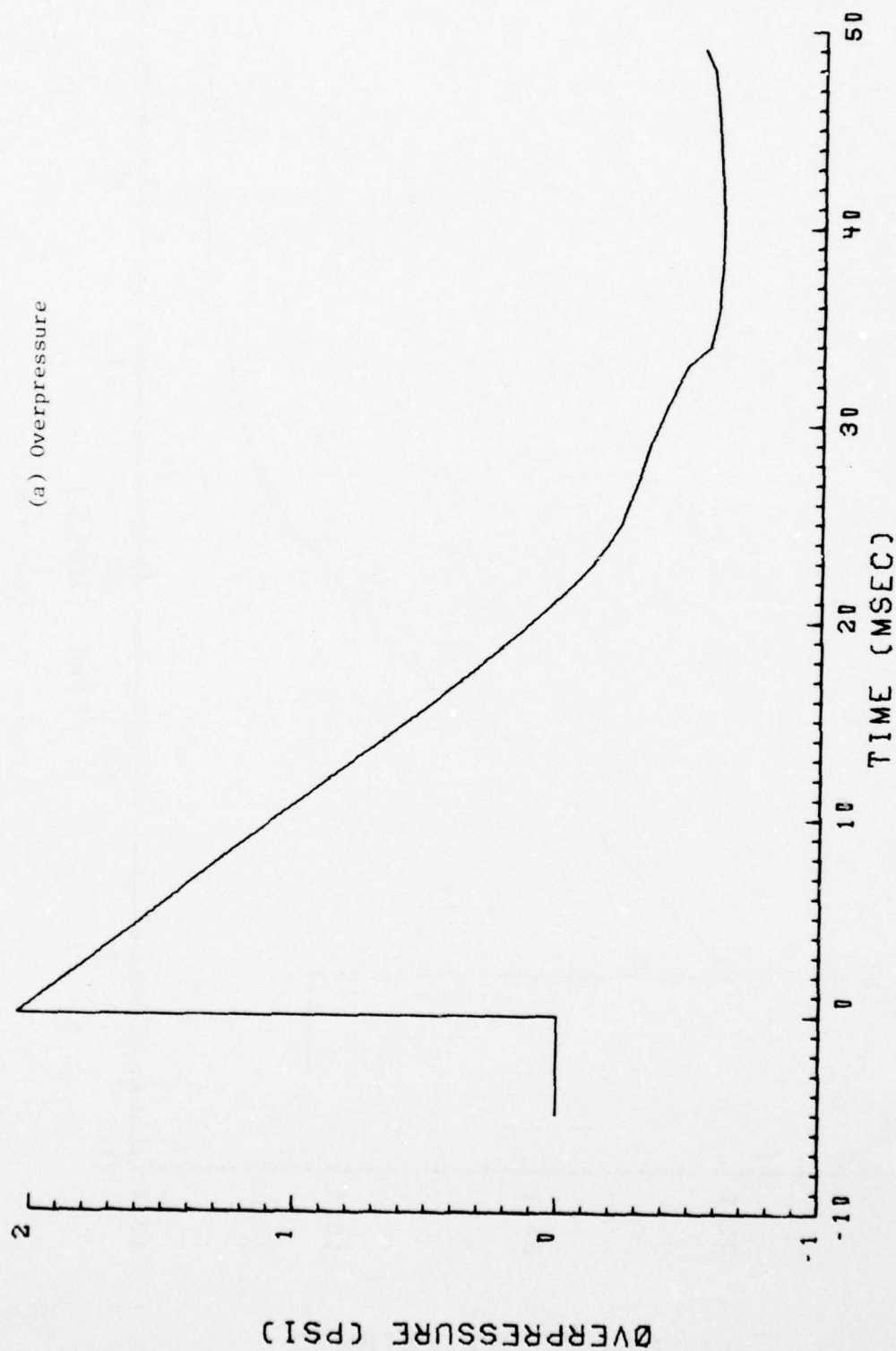


Figure 19. Blast Flow Conditions at the Sled for Run 9B-A1, Intercept 2

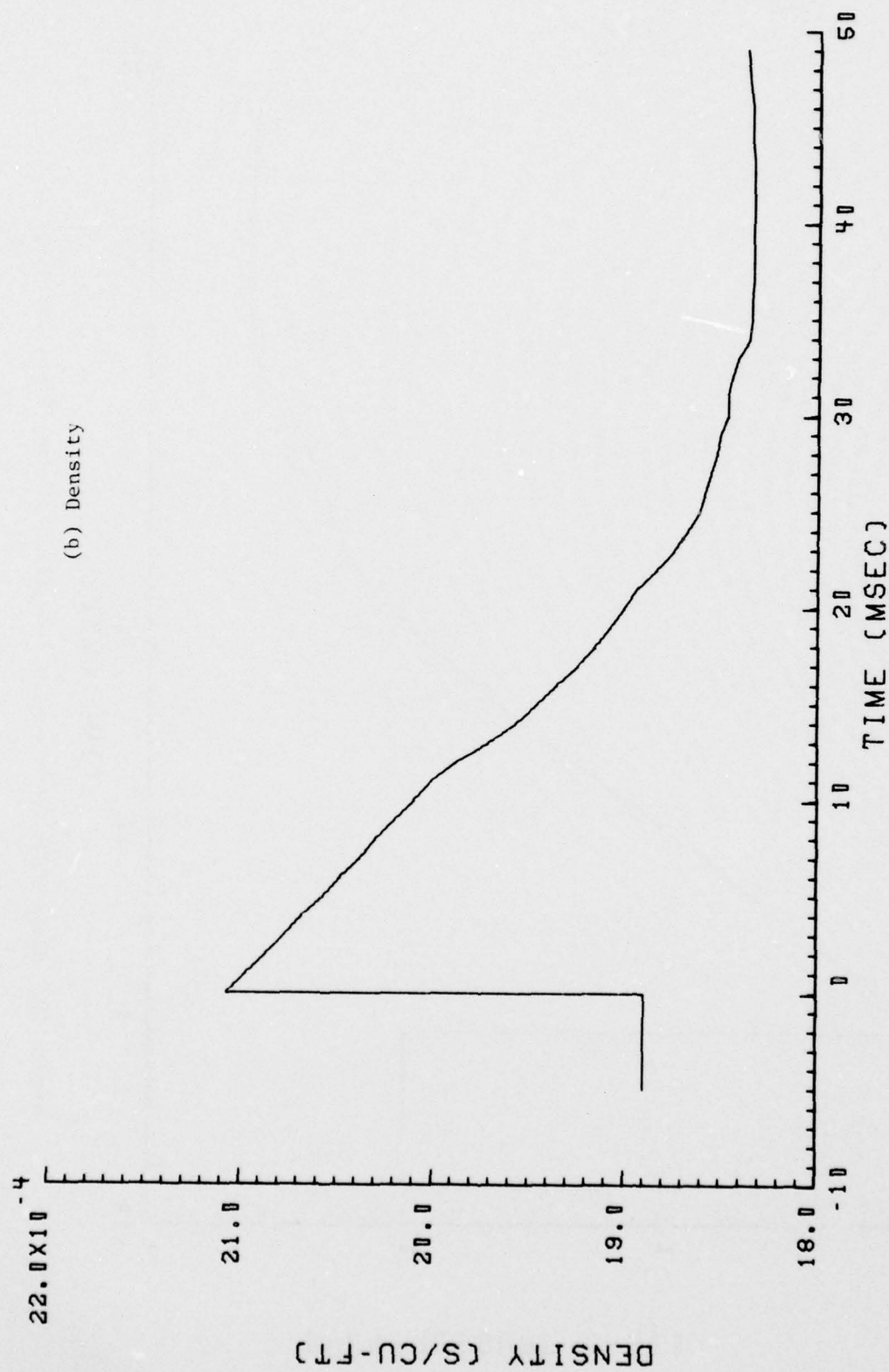


Figure 19. (Continued)

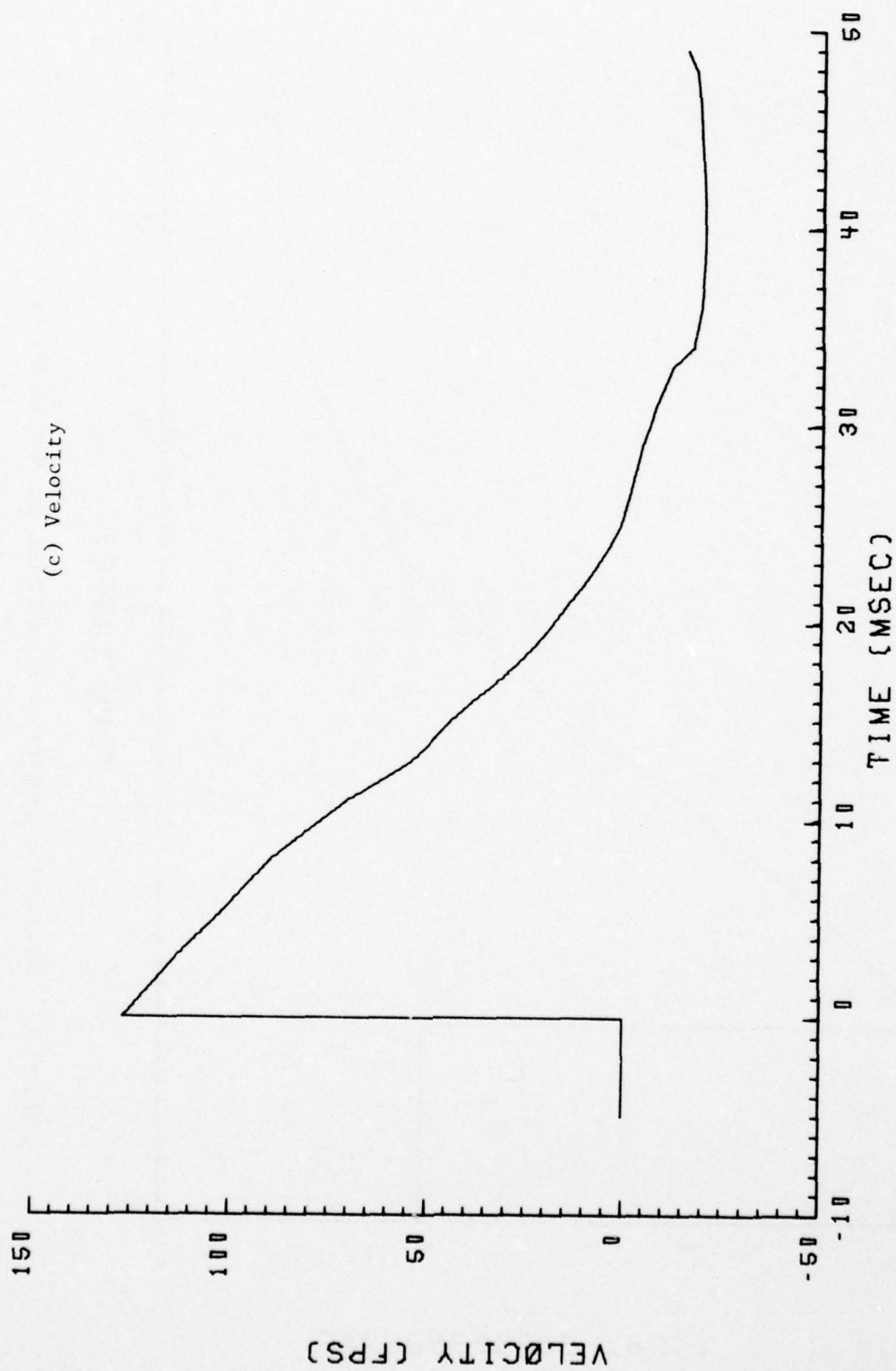


Figure 19. (Concluded)

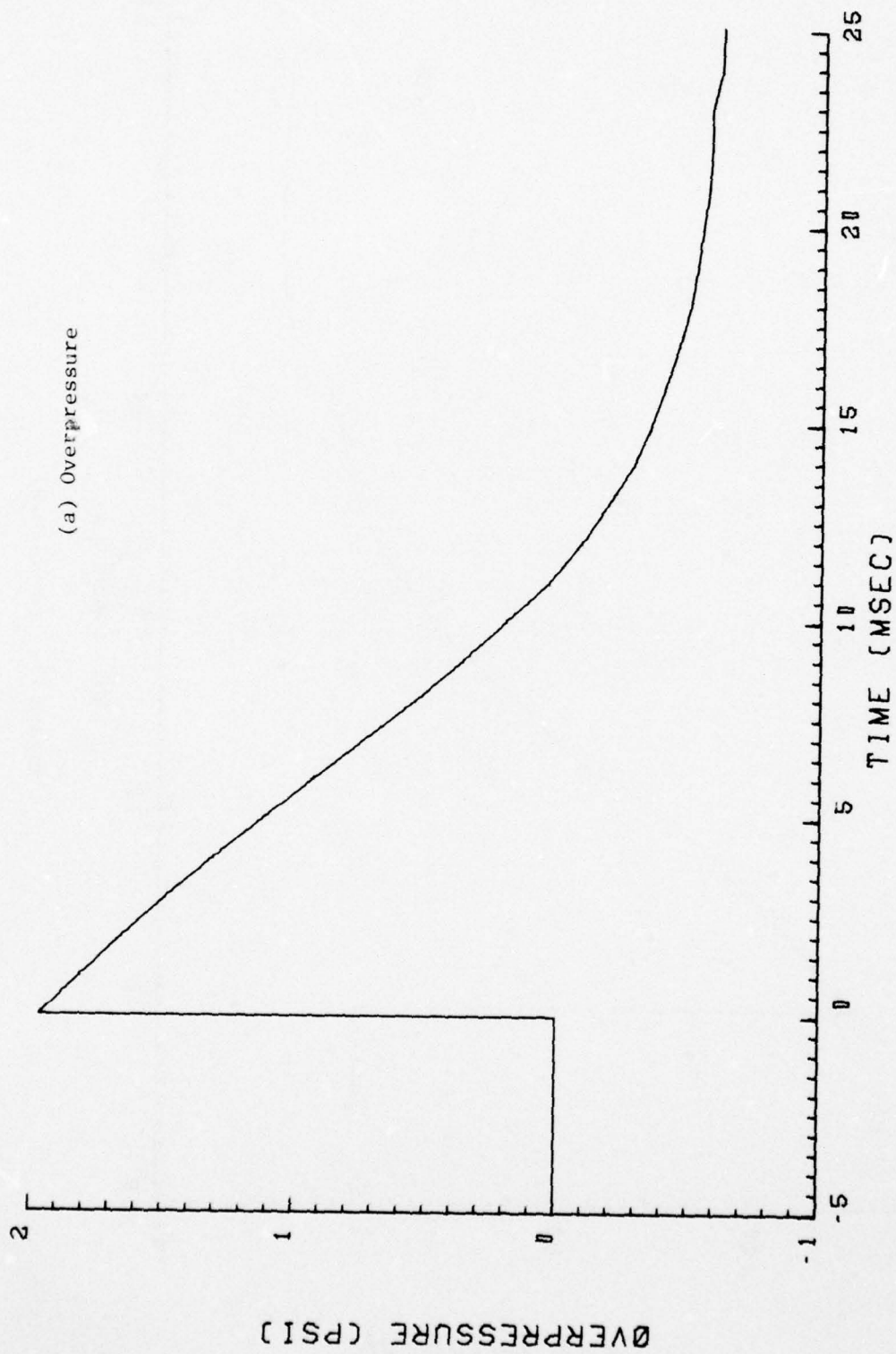


Figure 20. Blast Flow Conditions at the Sled for Run 9B-A2, Intercept 1

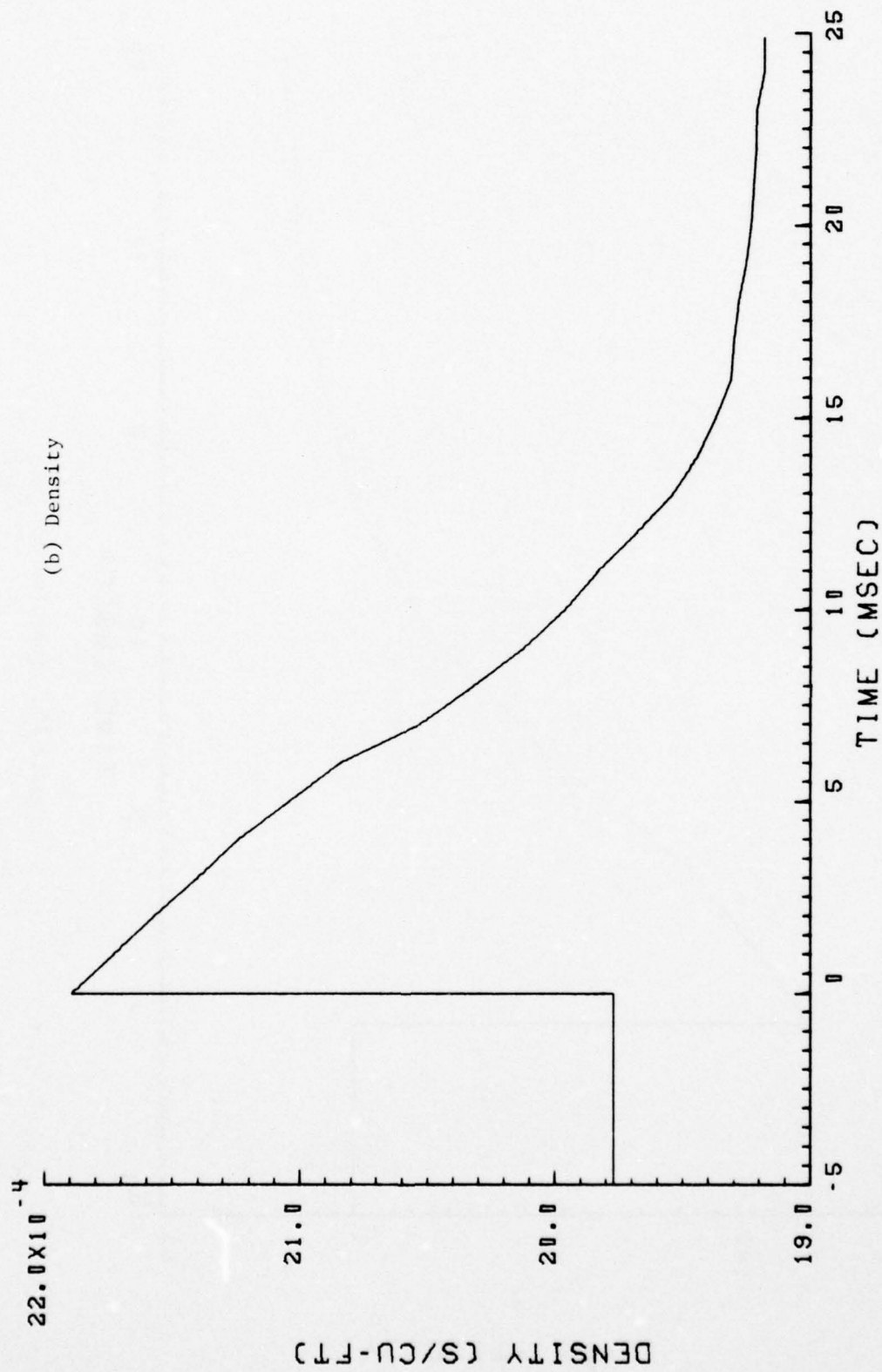


Figure 20. (Continued)

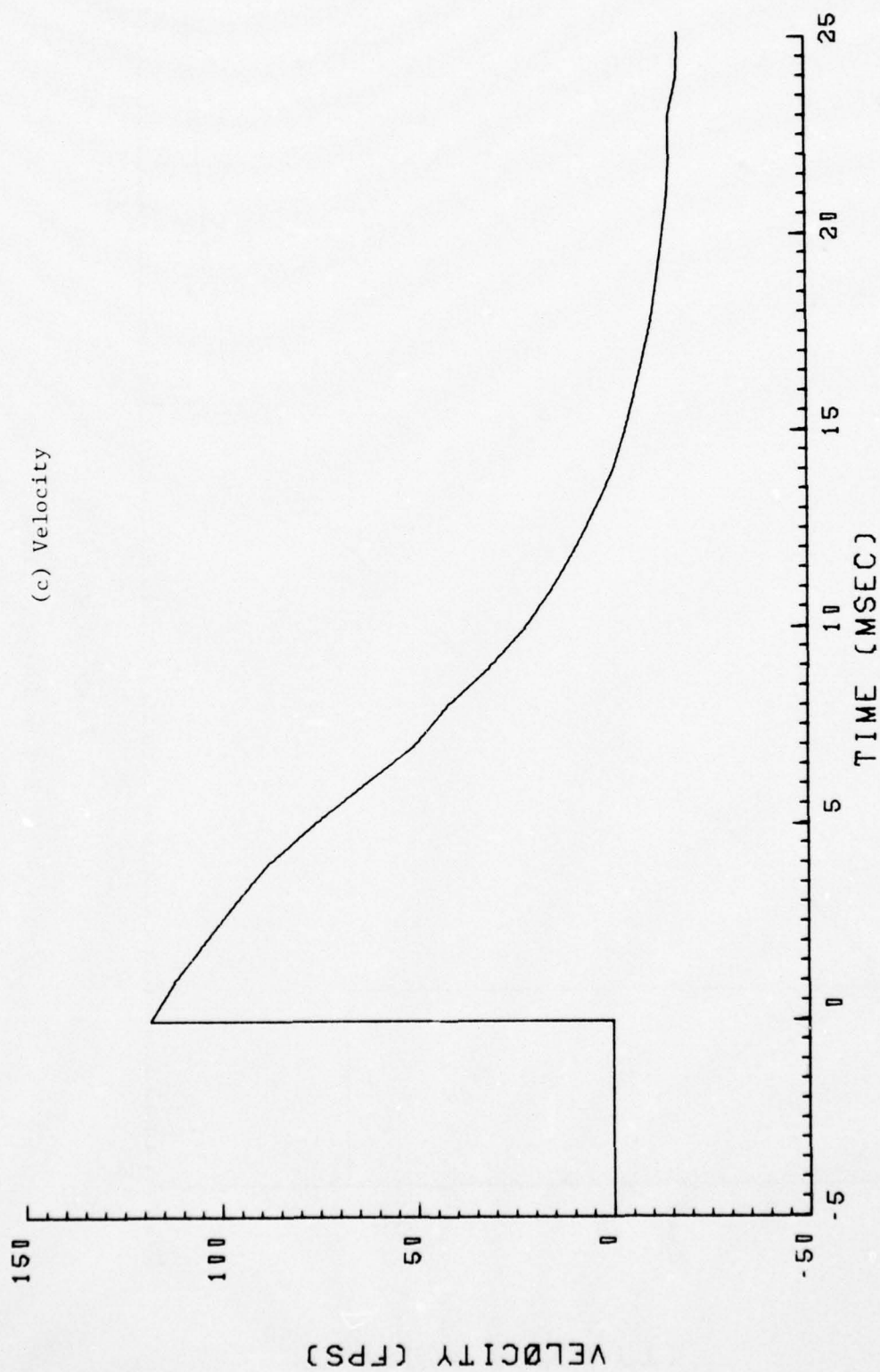


Figure 20. (Concluded)

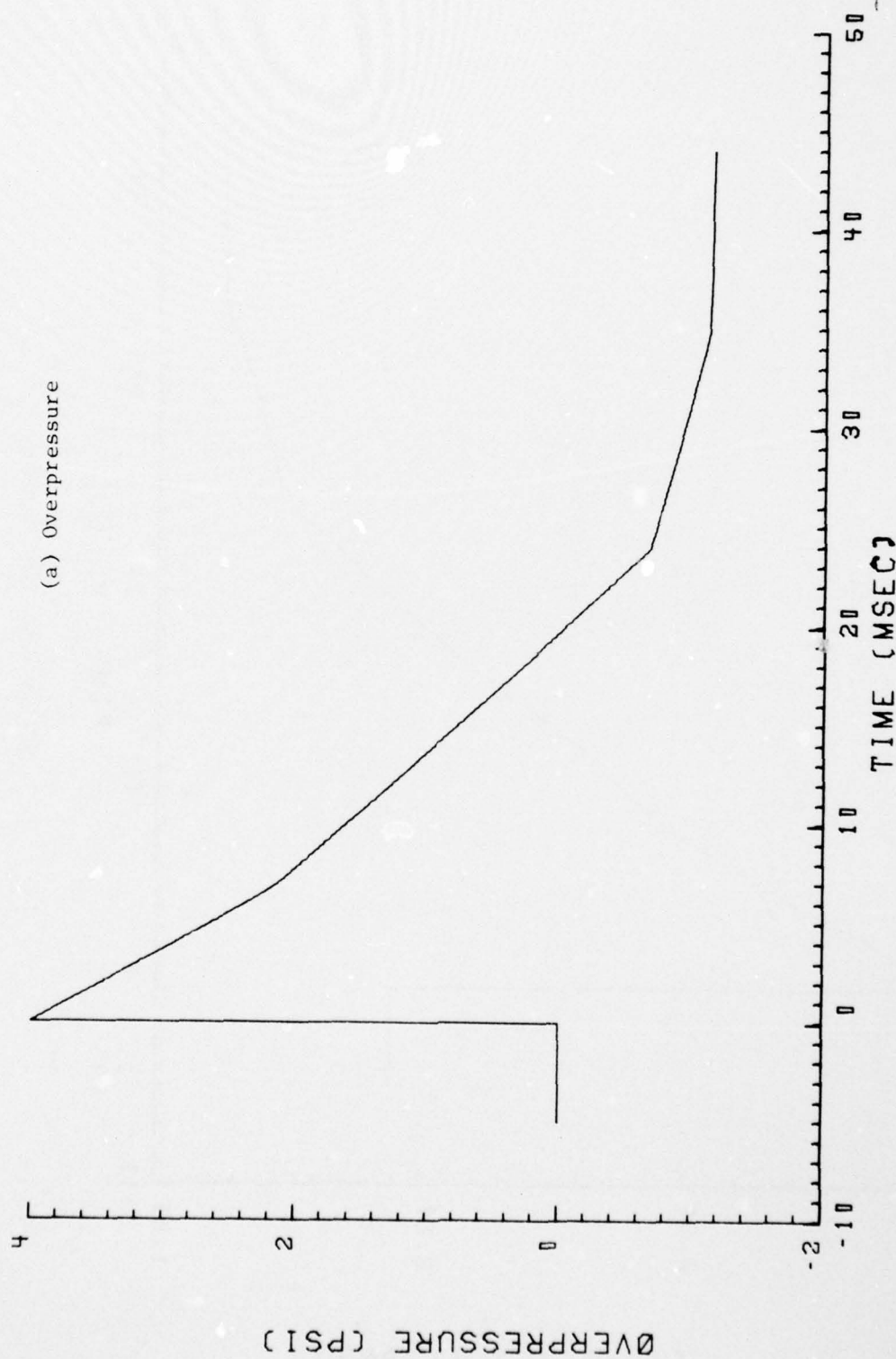


Figure 21. Blast Flow Conditions at the Sled for Run 9B-A2, Intercept 2

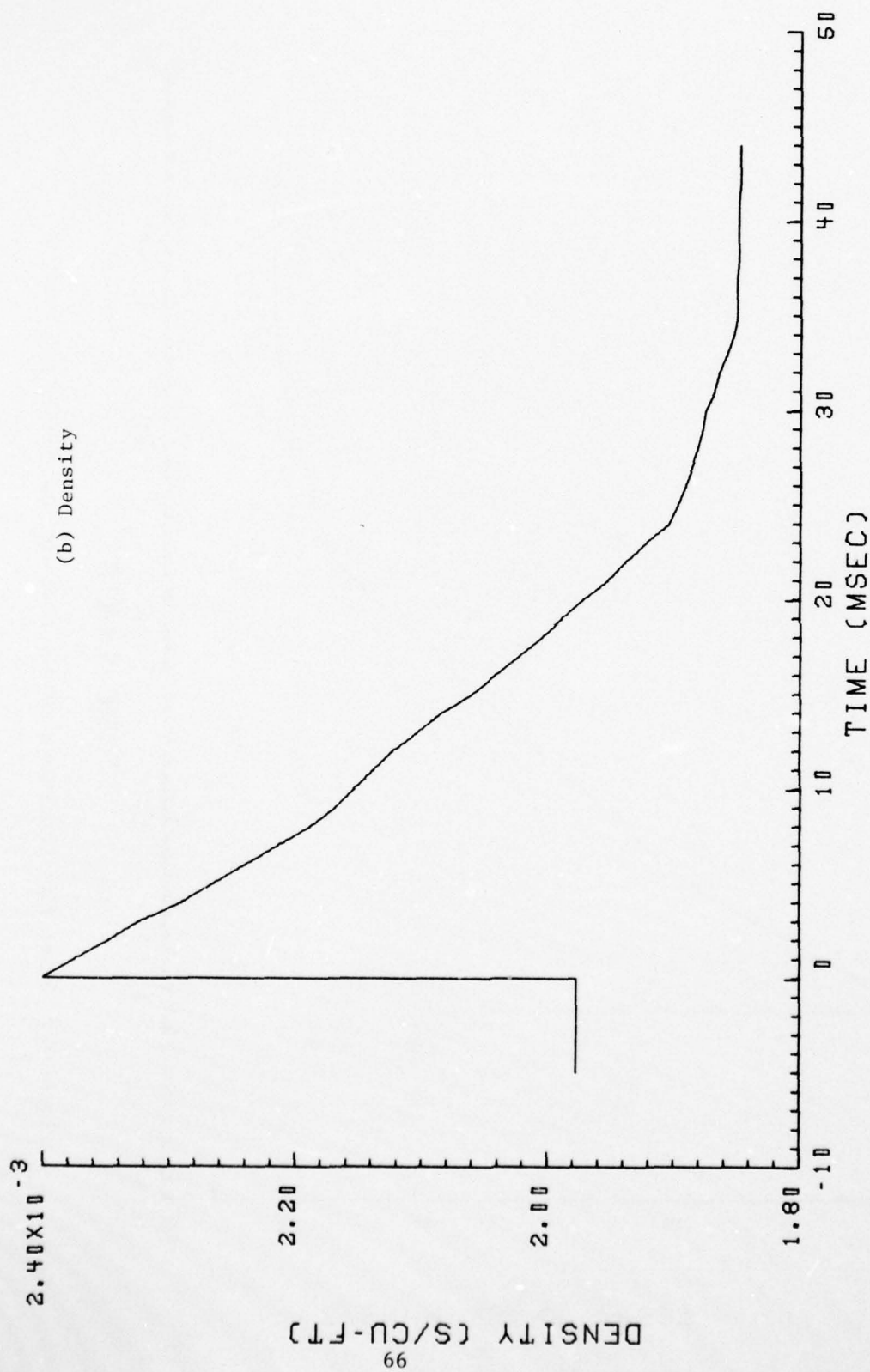


Figure 21. (Continued)

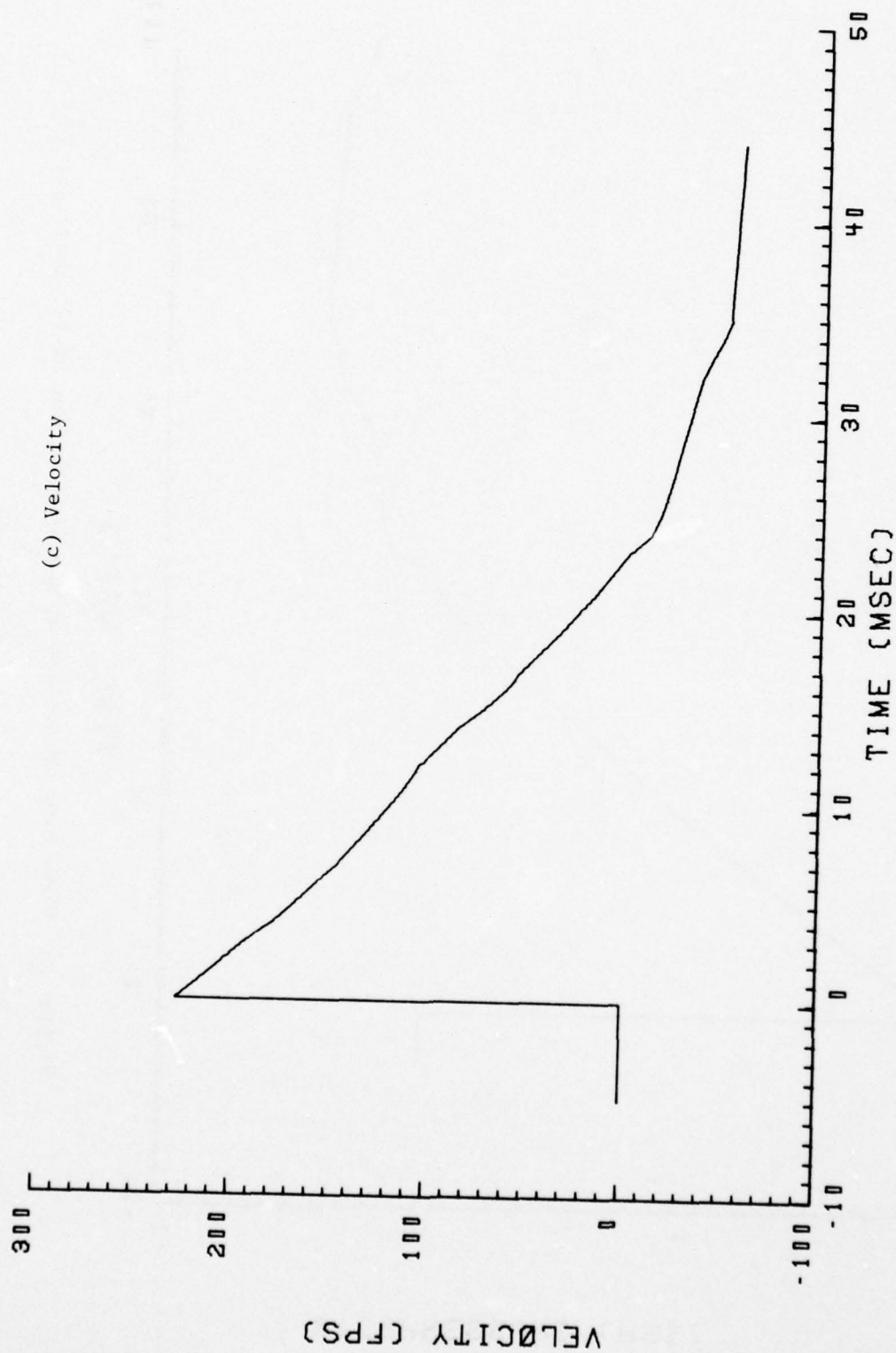


Figure 21. (Concluded)

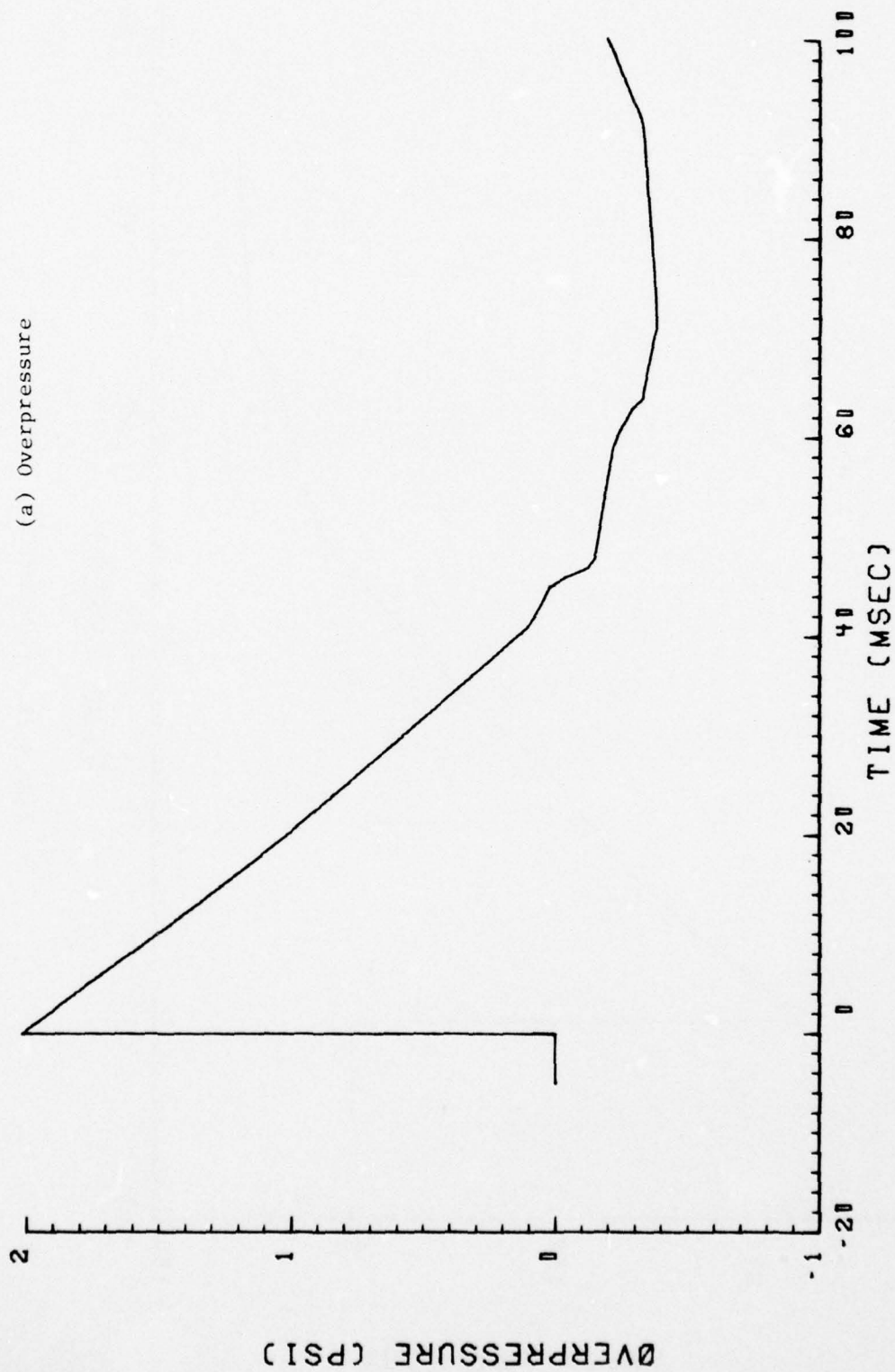


Figure 22. Blast Flow Conditions at the Sled for Run 9B-A2, Intercept 3

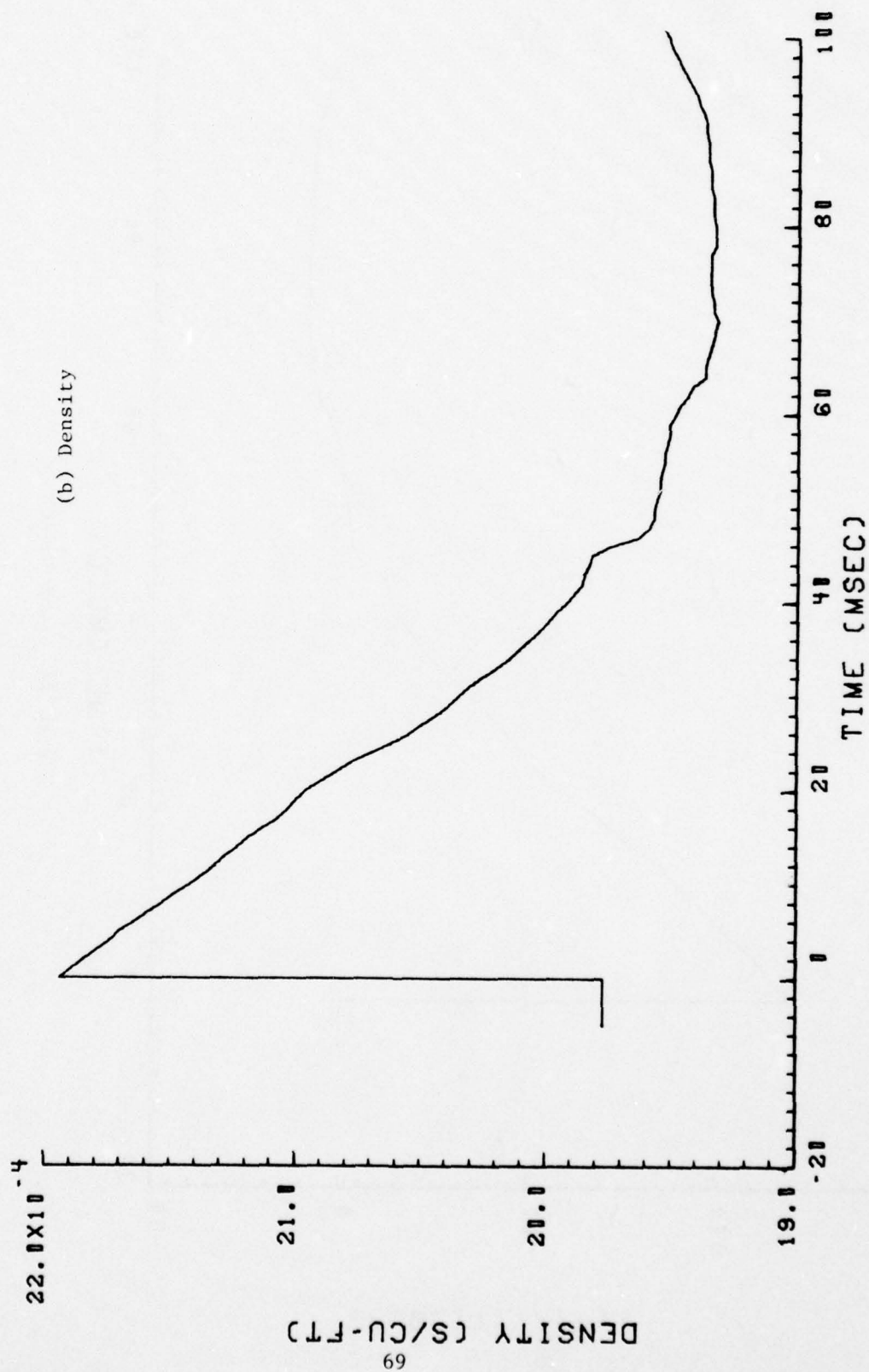


Figure 22. (Continued)

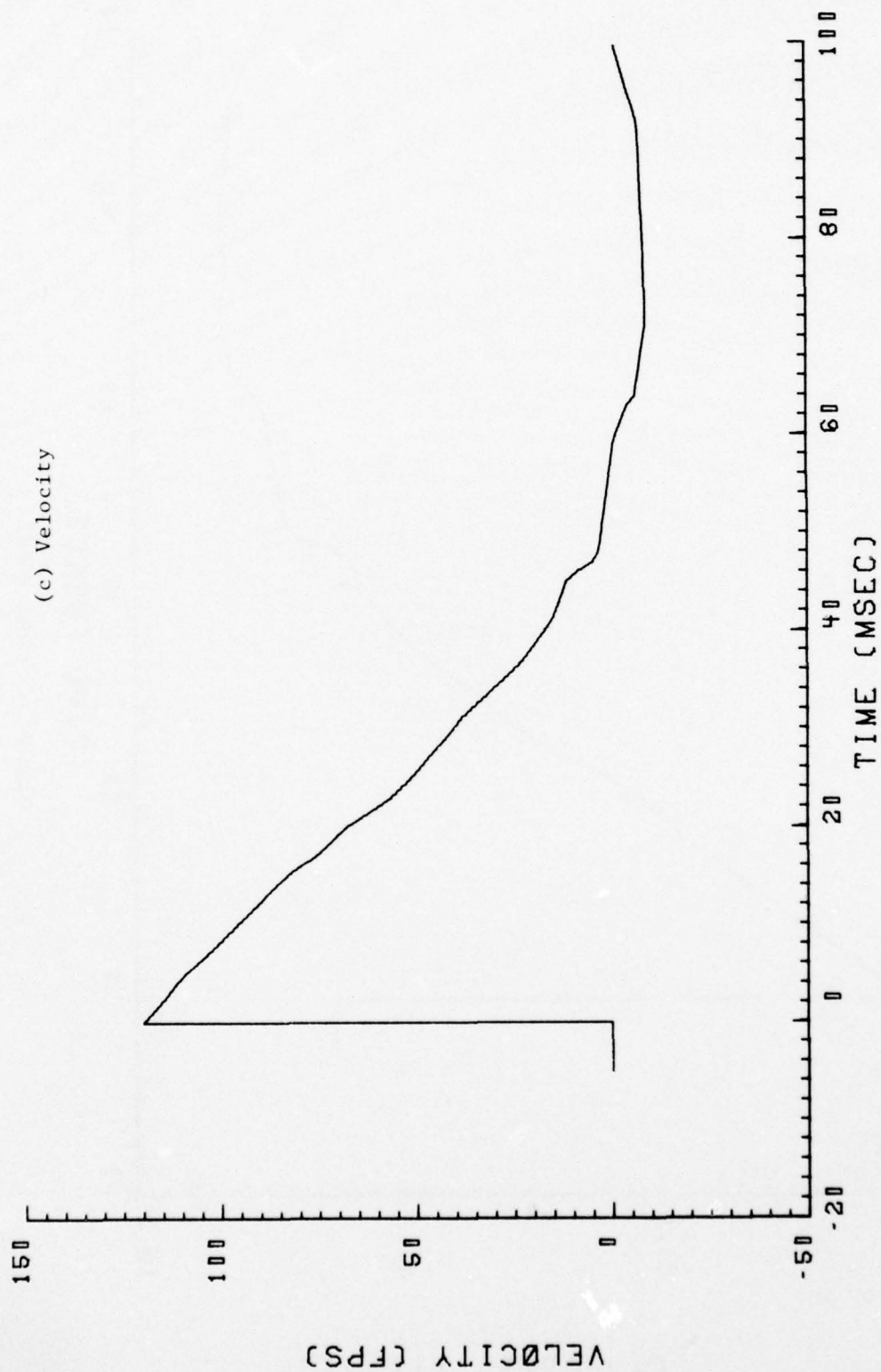


Figure 22. (Concluded)

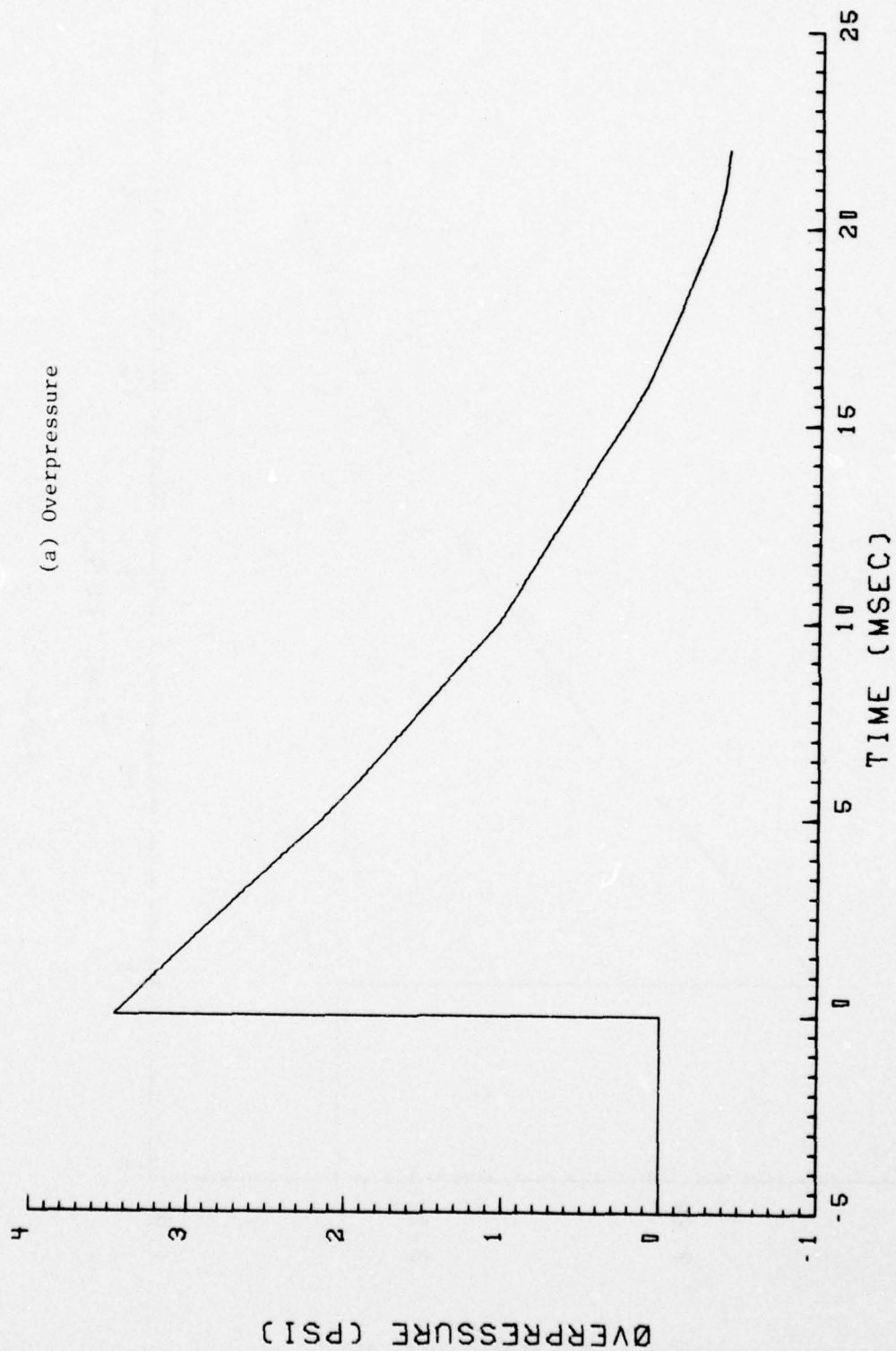


Figure 23. Blast Flow Conditions at the Sled for Run 9B-A3, Intercept 1

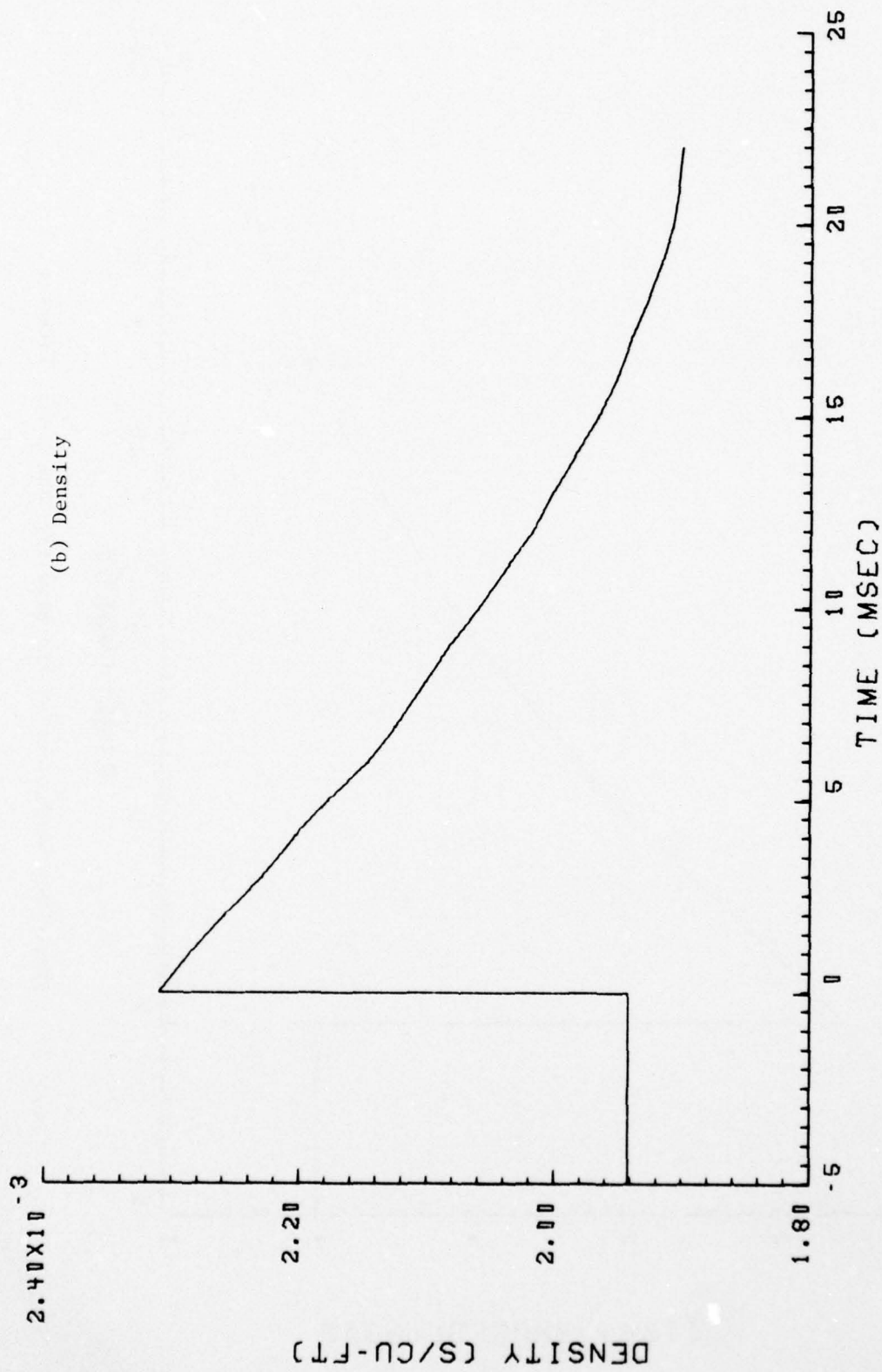


Figure 23. (Continued)

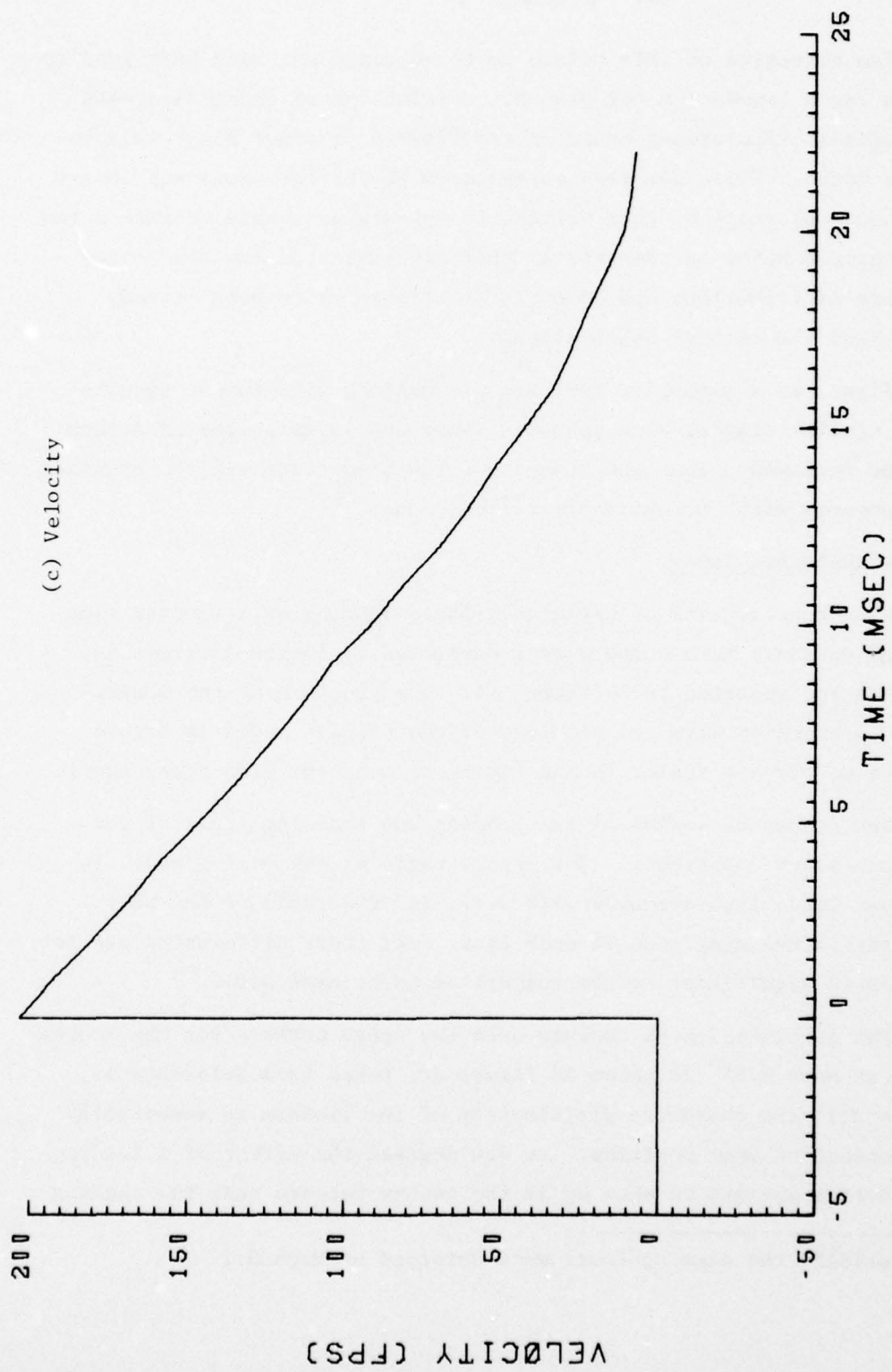


Figure 23. (Concluded)

6. DISCUSSION

The objective of this volume is to document the sled test results and to lay a foundation for planned correlations of these data with theoretical calculations based on the VIBRA-6 or other blast vulnerability codes. While detailed correlation of the test data and theory is beyond the scope of this volume, it appears desirable to make a few observations below on the general characteristics of the sled-borne pressure distributions and on their relationships to quasi-steady linearized theoretical calculations.

First, as a guideline for this discussion, wind-tunnel results for a similar wing at high subsonic speed and large angles of attack will be reviewed. Then the results of the sled tests will be examined and compared with the available calculations.

6.1 Wind-Tunnel Tests

Wind-tunnel tests of the steady-state loading on a similar wing at high subsonic Mach numbers were performed by Boeing Aircraft Co. for NASA and reported in Reference 14. The planform of the Boeing model is compared with the planform of the present model in Figure 24; the models are scaled in the figure to make the plan areas equal.

The sweepback angles of the leading and trailing edges of the two models are comparable. The aspect ratio of the Boeing model is somewhat less, 1.65 compared with 2.47, and the ratio of the body diameter to the wing span is much less. But these differences are not considered significant to the comparison to be made here.

The distribution of isobars over the upper surface for the Boeing model at Mach 0.85^{*} is shown in Figure 25, taken from Reference 14. At $\alpha = 2.1^\circ$ the chordwise distribution of the isobars is essentially independent of span position. At 4.0 degrees the effect of a leading-edge vortex appears to show up in the isobar pattern near the leading

* Essentially the same contours were obtained at Mach 0.7.

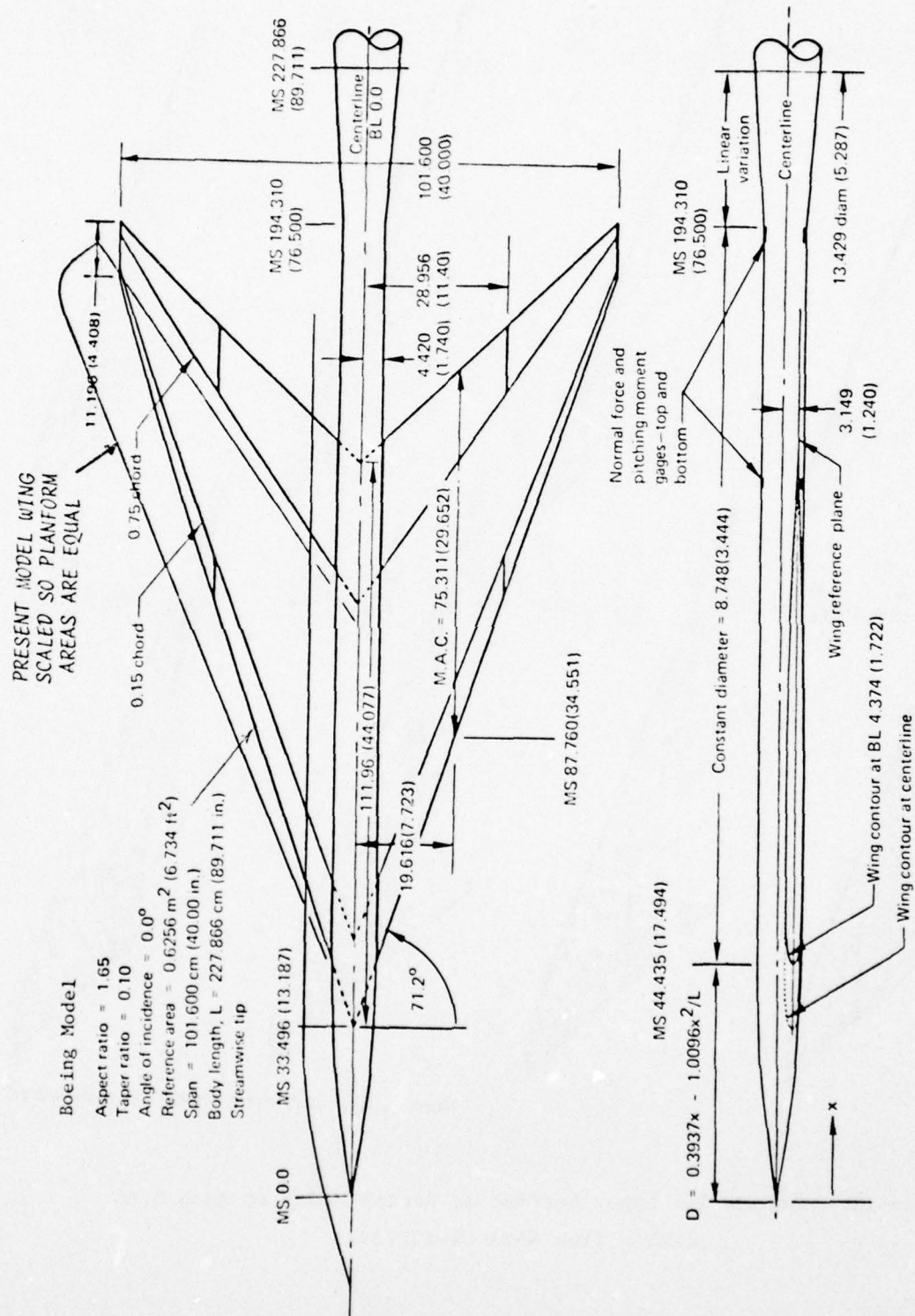
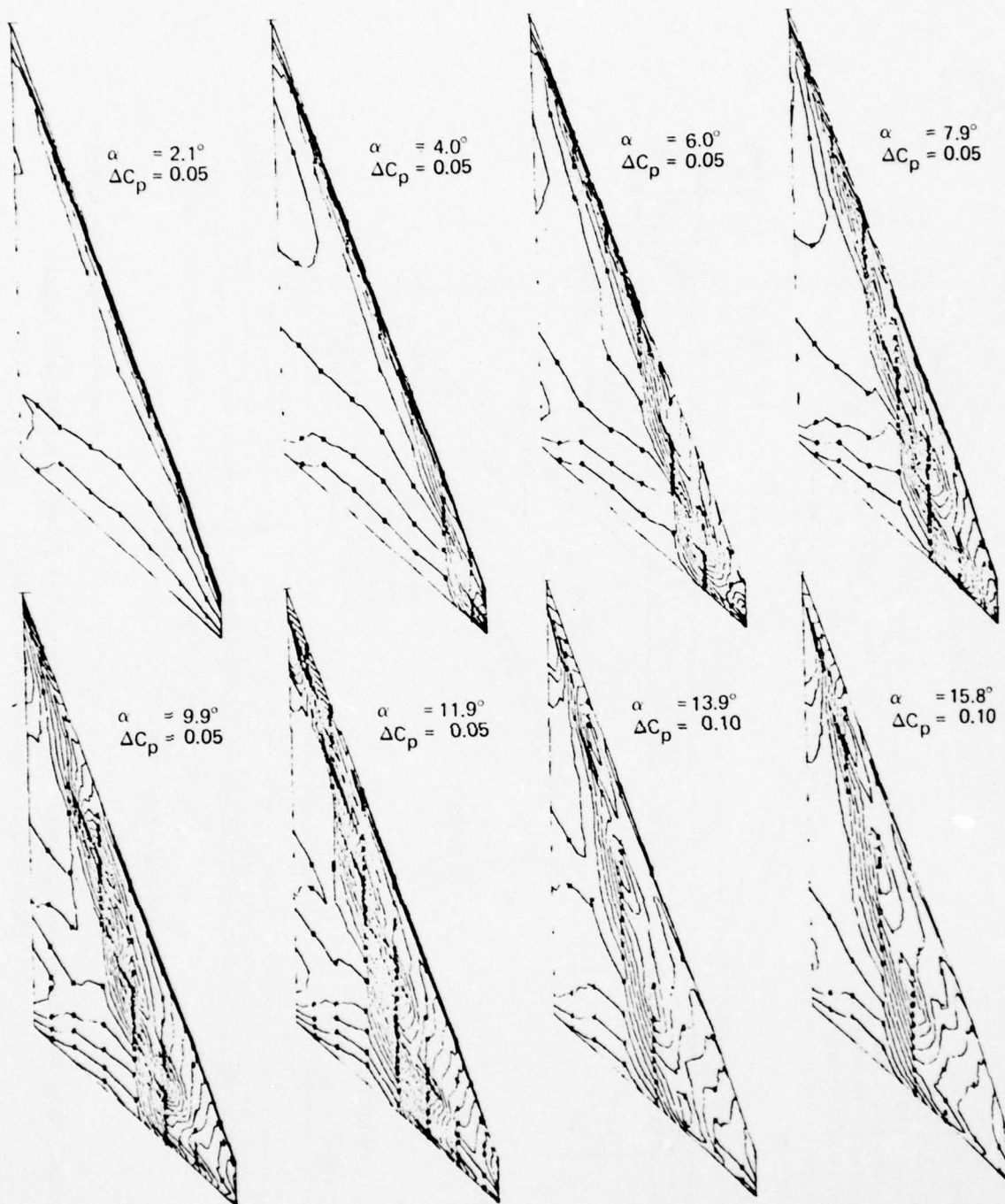


Figure 24. Wing Details of Boeing Model and Comparison With Planform of Present Model
(Boeing data from NASA CR-132727)



Note: ΔC_p = increment between adjacent isobars

Figure 25. Isobars for Upper Surface of Boeing Model at Mach 0.85
(Taken from NASA CR-132727)

edge. Shock waves may be present, but they are difficult to identify in the isobar pattern. At the 6.0-deg angle of attack, the vortex sweep angle is a little greater. As the angle of attack increases further, the sweepback-angle of the leading-edge vortex increases and the effect on the pressure distribution becomes more marked.

The general effect of the leading-edge vortex on the loading can be deduced from the upper surface isobars. In the vicinity of the vortex the upper-surface pressure is reduced so the loading is increased. Inboard of the vortex the loading, based on the isobars, is maintained fairly well, because the flow does not separate there, whereas outboard the loading is reduced by the vortex, due to separation of the flow from the wing. So the effect of the vortex is essentially to increase the loading at the vortex, maintain it inboard and decrease it outboard. For this reason, when the vortex sweepback angle is relatively small, the lift tends to be increased by the vortex from the linearized value, and, when the vortex sweepback is increased further, at some point the loading increment relative to the linearized value falls off, possibly going negative.

The chordwise distribution of loading for the Boeing wing is shown in Figure 26 for seven stations along the semispan. At an angle of attack of 2.1 degrees, the loading distributions have the classical shape with a suction peak near the leading edge. At 4.0 degrees the classical shape is maintained except near the tip, $0.93b/2$, where the peak is gone and the distribution is essentially flat over the whole chord due to the leading edge vortex. The section normal force at $0.93b/2$ is a maximum, however, at four degrees. At six degrees the suction peak of the leading edges of the wing is absent from $0.65b/2$ outward and the section normal force at $0.80b/2$ is at a maximum. This trend, of the spanwise extent of the leading-edge suction decreasing and the chordwise section having its maximum normal force being further inboard, continues as the angle of attack increases.

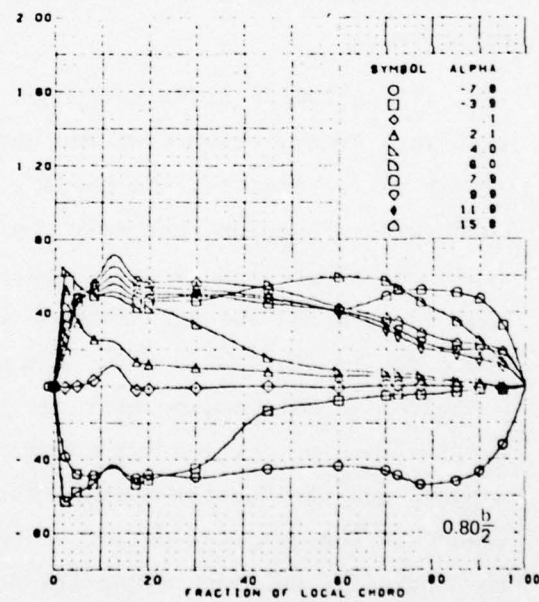
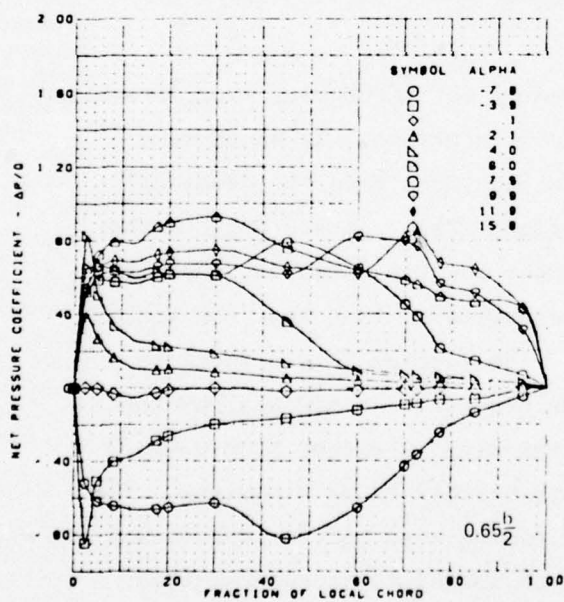
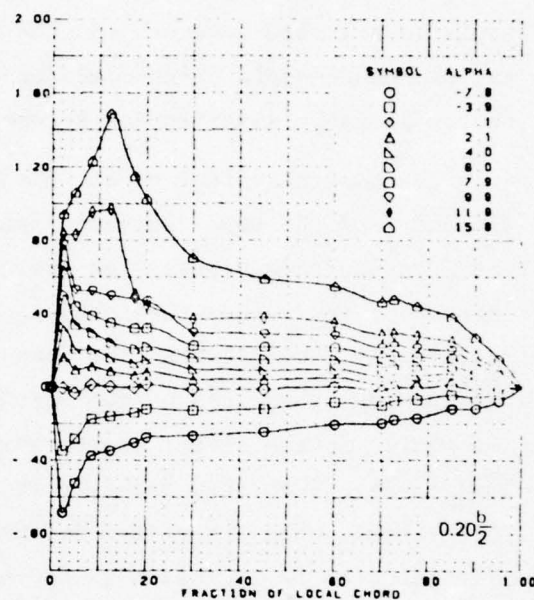
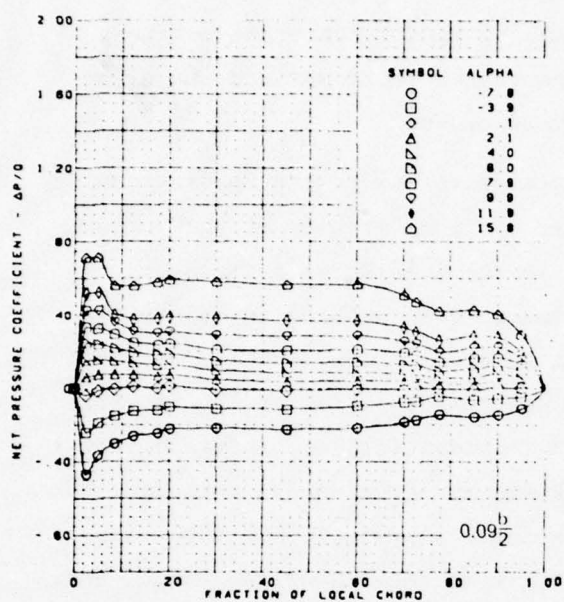
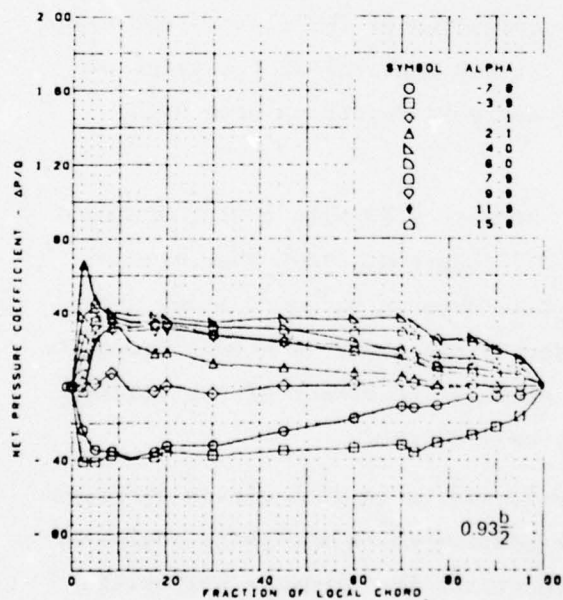
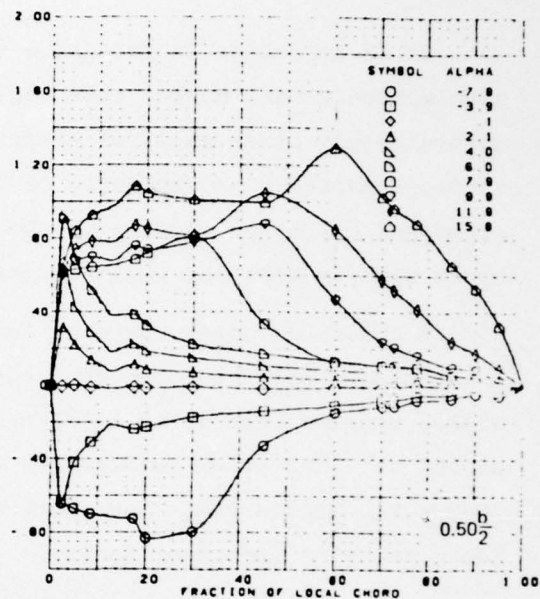
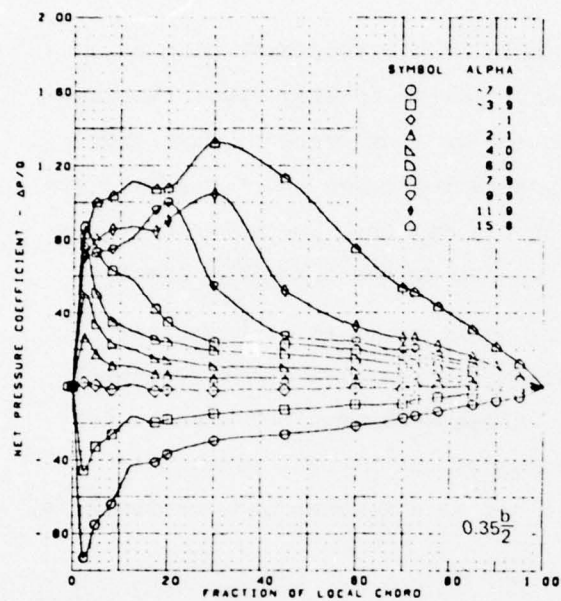


Figure 26. Net Chordwise Pressure Distributions for Boeing Model at Mach 0.85
(Taken from NASA CR-132727)



$M = 0.85$ (run 267)
 Flat wing, round L.E.
 L.E. deflection, full span = 0.0°
 T.E. deflection, full span = 0.0°

Figure 26 (Concluded)

It is important to recognize for this highly sweptback wing at a high subsonic Mach number that nonlinearities in loading start showing up noticeably at an angle of attack as low as four degrees, that they increase markedly as the angle of attack is increased and first have the strongest effect on loading in the wing tip region. The question for a blast wave is what the nonlinear effects are on the transient loading.

A number of other tests on loading nonlinearities at high subsonic Mach numbers have been reported for wings with quarter-chord sweepback angles ranging from 25 to 45 degrees. These tests are believed to be useful for indicating qualitative trends for the present wing, even though the latter has a sweepback angle of 64.8 degrees and sweepback is known to be an important factor.

Taylor (Reference 15) presents results of tests for a quarter-chord sweepback angle, $\Lambda_{c/4}$, of 40 degrees and thickness ratios of 0.09 to 0.11. The results show shock-induced separation of the flow on the upper surface to be important for angles of attack approaching the point of nonlinear lift (very roughly about 10 degrees, depending upon Mach number and many other factors).

Smith (Reference 16), from tests at Mach 0.78 with a wing having a quarter-chord sweepback angle of about 35 degrees, shows that at an angle of attack of 8.8 degrees a shock is present outboard along about the 30-percent shortline. At 10.1 degrees the shock is strong enough to separate the flow. At 12.6 and 16.0 degrees the effect of the leading-edge vortex on the flow is apparently well defined.

Ray and Taylor (Reference 17) performed tests with eleven different wings having different platforms with quarter-chord sweepback angles of 25 to 45 degrees and various airfoil sections for studying buffeting (unsteady loads due to boundary-layer separation). The onset of buffeting is shown to be a function of a number of factors, but near Mach 0.8 it occurs at an angle of attack very roughly of about five to eight degrees.

6.2 VIBRA-6 (Doublet Lattice) Correlation

It is intended to correlate the test results of the present tests with the VIBRA-6 doublet-lattice computer code as soon as this code is developed to an operational stage. As yet the code has not reached this stage but it is possible to make a few observations here based on some preliminary runs with the code.

First, it should be emphasized that the VIBRA-6 code is based on linearized theory. Second, it should be noted that the test wing has a relatively low aspect ratio so that code predictions would be expected to behave in a relatively quasi-steady manner after a short few milliseconds diffraction period while the blast wave front is crossing the wing. This rapid transition to the quasi-steady condition can be seen from preliminary unpublished VIBRA-6 runs made elsewhere. Consequently, it can be anticipated that the VIBRA-6 code predictions will not differ greatly from quasi-steady predictions at late time, say for times after blast arrival of 5 or more milliseconds.

In view of these observations, theoretical calculations of quasi-steady differential pressure time histories were made for transducer locations where differential pressures were measured and the resulting pressure time histories are shown together with the sled test data in Figures 27 to 31. These quasi-steady pressures are based on steady-state lift coefficients for the model, which were calculated with the VIBRA 6 code, and from transient pressure, density and velocity variations at the model which were determined from the blast-line test data as discussed in Section 5 and Appendix B.

6.3 Analysis of Blast Loading Histories

The transient blast loadings at the 20 locations on the wing are examined below for the five blast intercepts of the present sled-test program. The wind-tunnel test results and the VIBRA-6 quasi-steady loading calculations (V6QS) of Sections 6.1 and 4.2 are used as a basis for comparison. The side-on, near-90-deg., blast intercept tests will be discussed first, followed by the tests at blast intercepts at angles, ϕ , of about 20 and 135 degrees. ϕ is defined as the angle between the

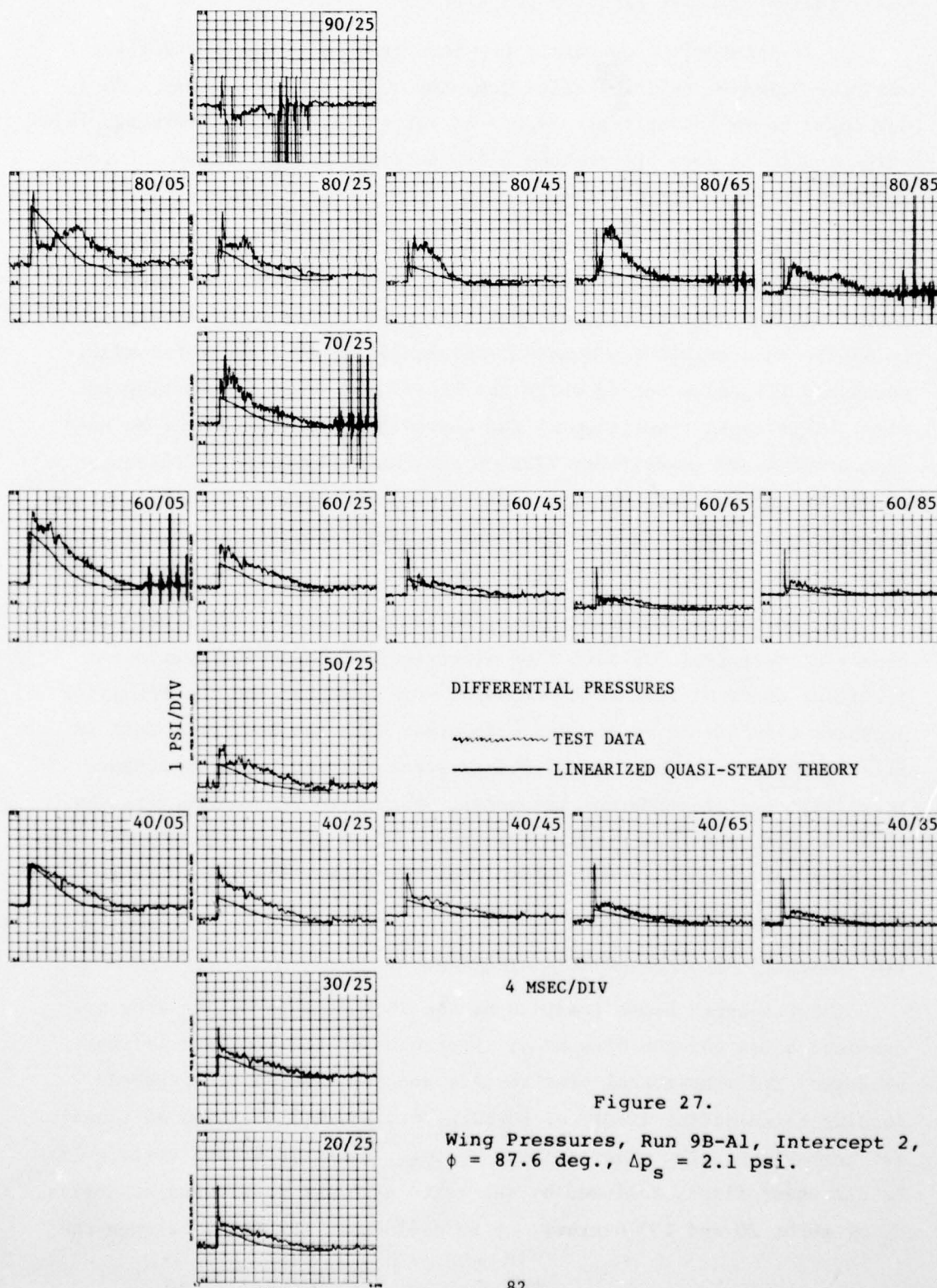


Figure 27.

Wing Pressures, Run 9B-A1, Intercept 2,
 $\phi = 87.6 \text{ deg.}$, $\Delta p_s = 2.1 \text{ psi.}$

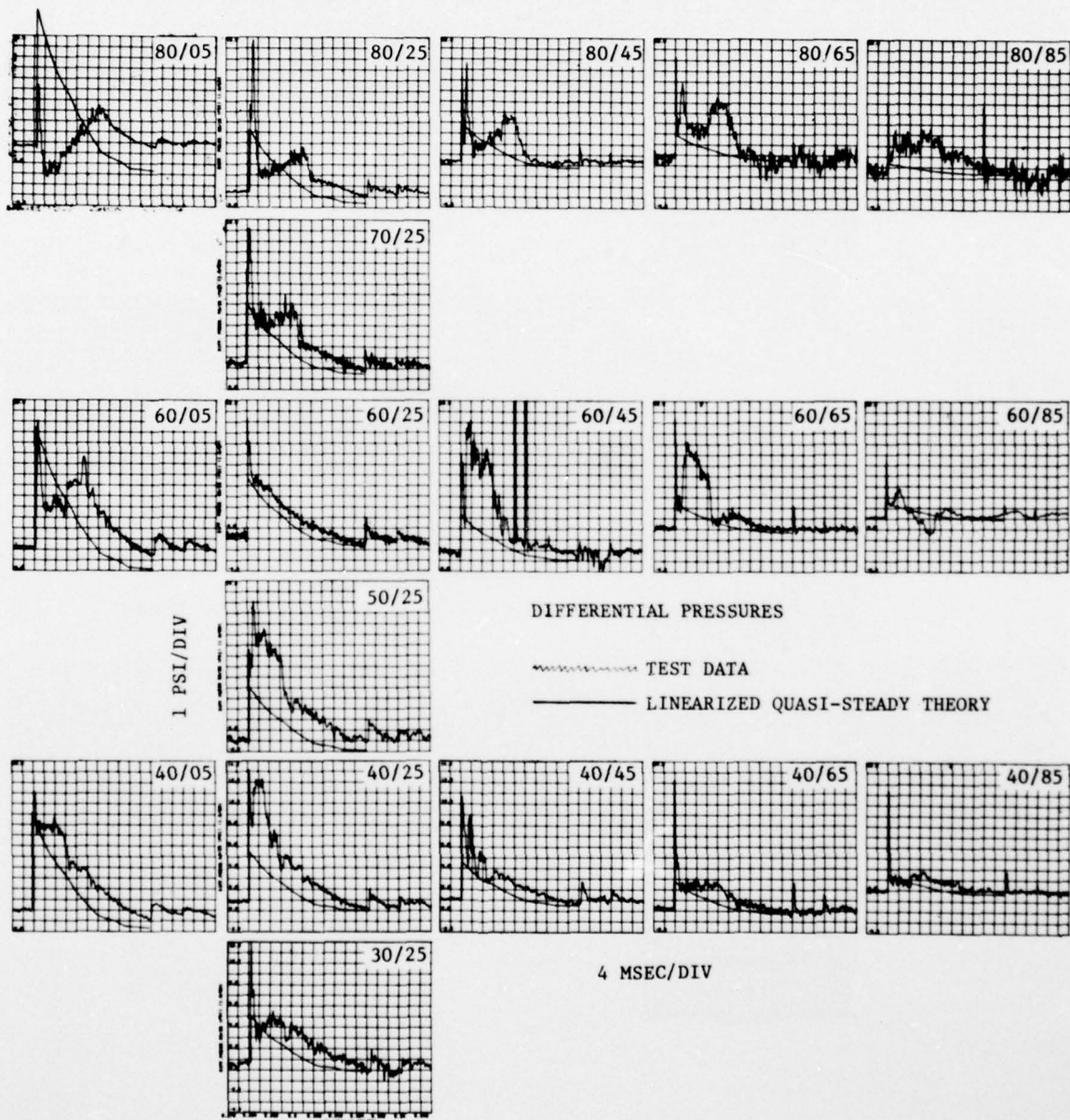


Figure 28. Wing Pressures, Run 9B-A2, Intercept 2,
 $\phi = 90.3$ deg., $\Delta p_s = 4.0$ psi.

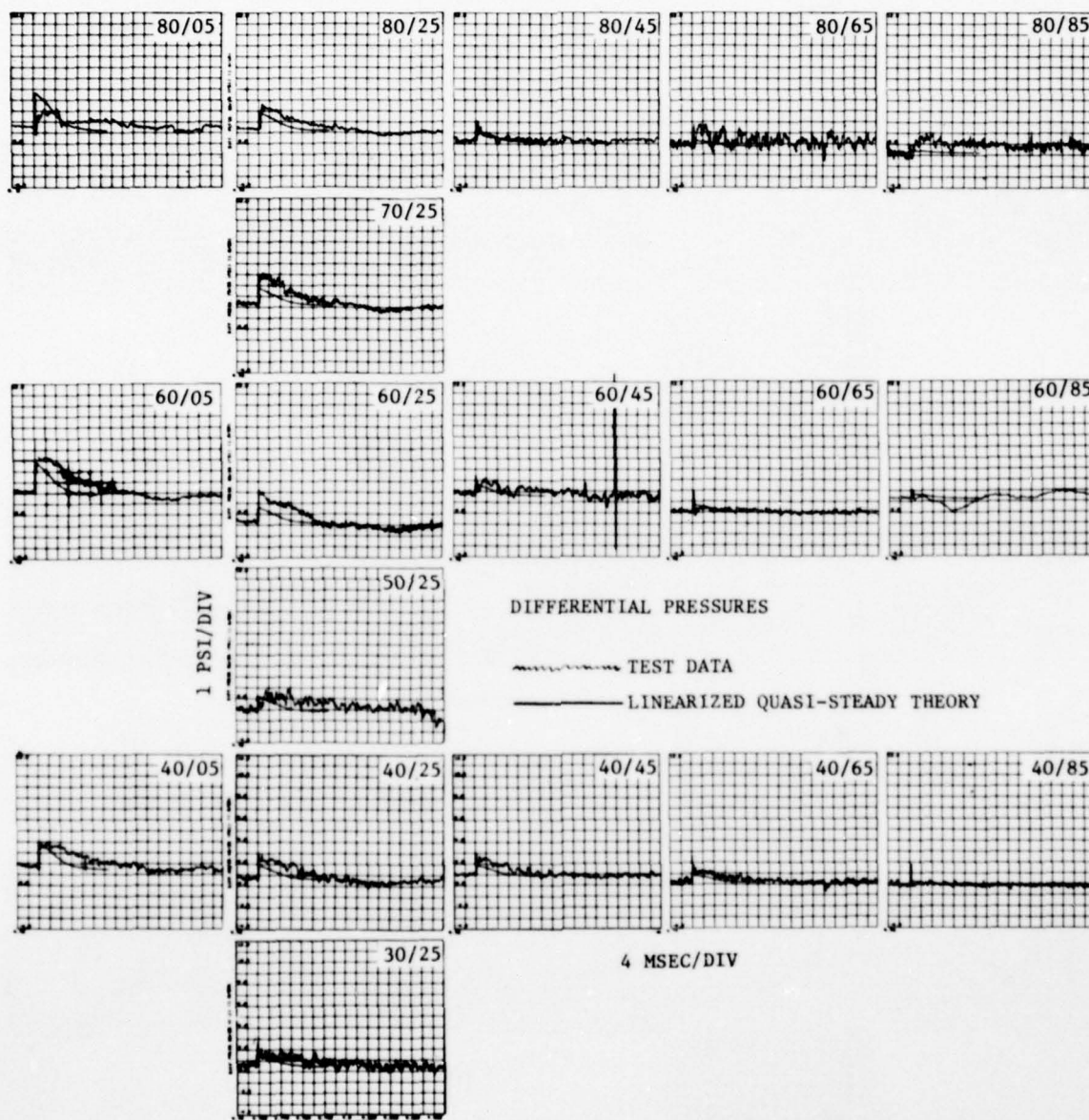


Figure 29. Wing Pressures, Run 9B-A2, Intercept 1,
 $\phi = 20.1$ deg., $\Delta p_s = 2.0$ psi.

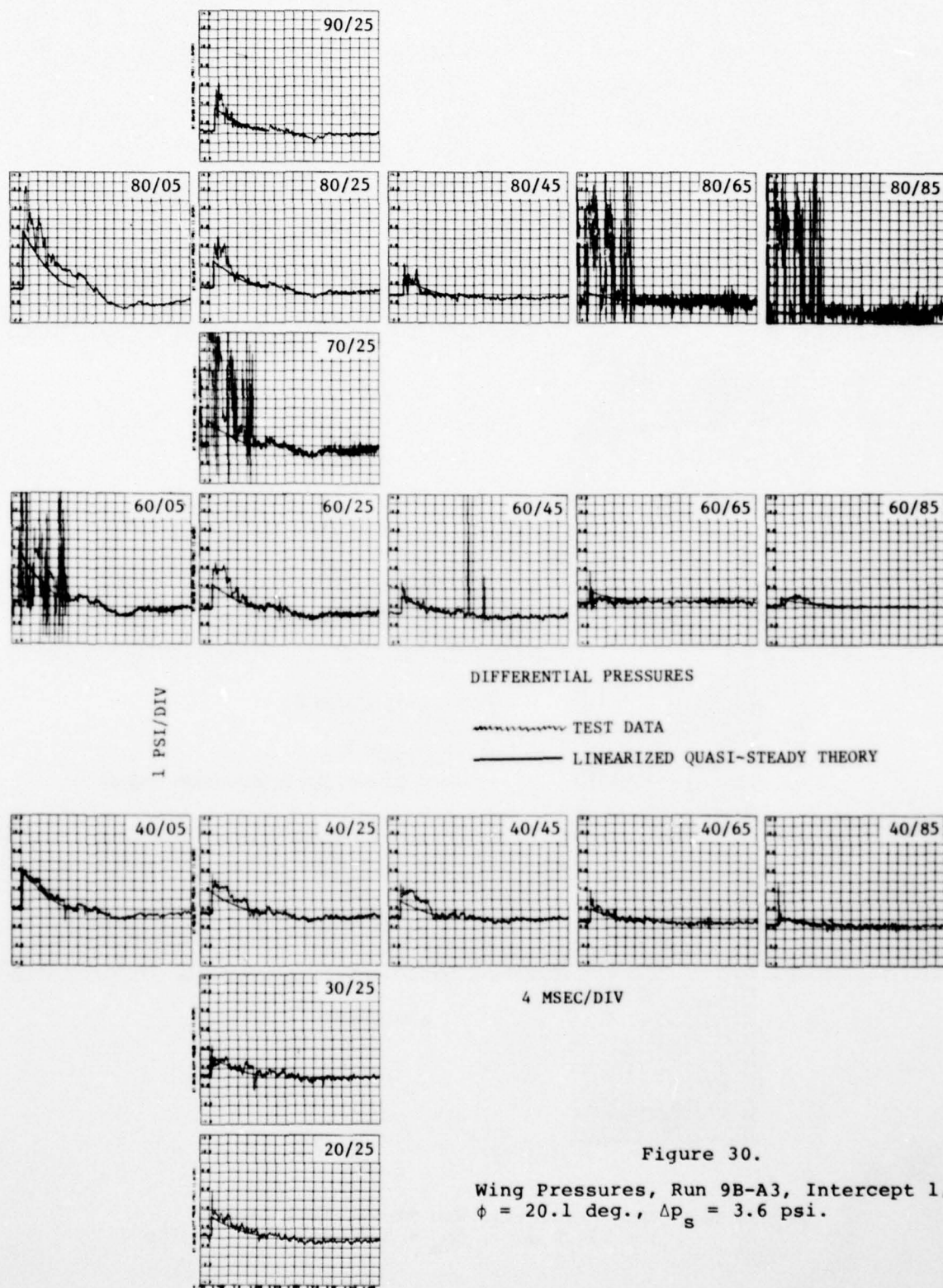


Figure 30.
Wing Pressures, Run 9B-A3, Intercept 1,
 $\phi = 20.1$ deg., $\Delta p_s = 3.6$ psi.

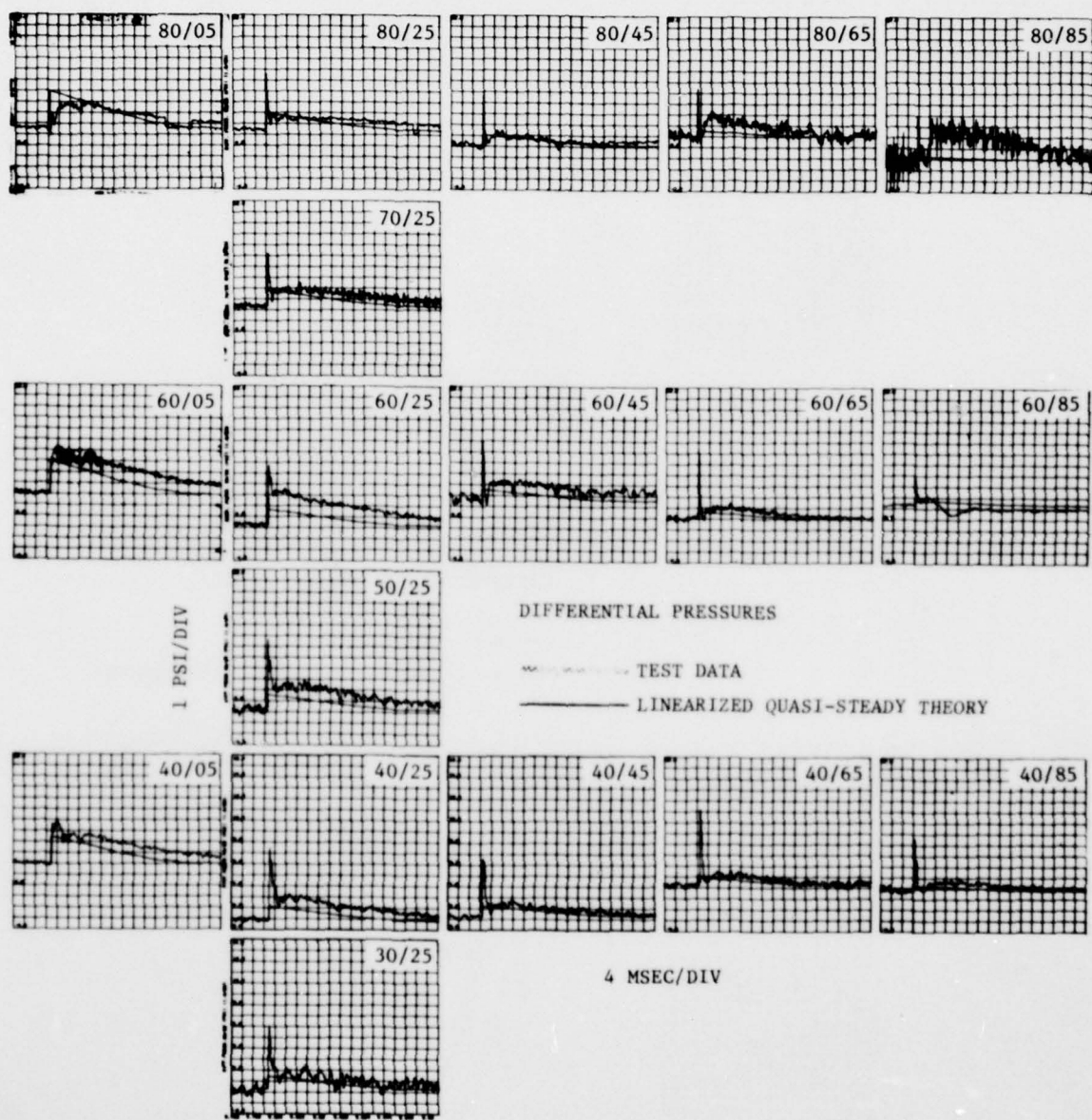


Figure 31. Wing Pressures, Run 9B-A2, Intercept 3,
 $\phi = 134.9$ deg., $\Delta p_s = 2.0$ psi.

sled velocity vector and a line from the model reference point (intercept of wing 40-percent chordline at the model axis) at blast intercept to the ground point of the charge center.

The loading histories and the V6QS loadings are presented together in Figures 27 to 31. It should be noted that the ordinates of the V6QS loadings have been shifted to match the preintercept level of the test data, and their time scales have been shifted to match the observed shock-induced jump. The time for the measured shock-induced jump will be taken as the time-origin in the discussion.

6.3.1 Intercept 9B-A1; $\phi = 87.6$ deg., $\Delta p_s = 2.1$ psi (Fig. 27)

For the 2.1 psi intercept at 87.6 degrees from head-on, the angle of attack at blast intercept, α_I , was 11.4 degrees and the positive velocity duration at the sled, t_{v+} , was 25.7 milliseconds for this near-side-on blast intercept. The shock diffraction period apparently lasts about one to two milliseconds. The diffraction loading is most apparent for the inboard and rearward stations where the post-diffraction loadings are small. Otherwise the diffraction loadings on an impulse (time integrated) basis are relatively small compared with the post-diffraction loadings.

During the post-diffraction period the loading histories for the wing area from $0.60b/2$ inboard roughly follow V6QS predictions, although the level of the measured loadings is generally noticeably higher, particularly for the region towards the leading edge. Using the shock-induced jump of the quasi-steady VIBRA-6 predictions as a basis for comparison, the measured loadings range from 25 to 100 percent greater than the V6QS shock-jump predictions.

Over the outboard region of the wing from $0.70b/2$ to $0.90b/2^*$, the loading histories have a distinctly different signature from the V6QS predictions with differences in magnitude even greater than inboard, by up to five times the shock jump in V6QS. Here there is a noticeable

* b is wing span and c is wing chord.

indication of a leading-edge vortex. At $0.70b/2$ and $0.25c^*$ (70/25), 80/45 and 80/65 the loading tends to be high during the period from four to twelve milliseconds (after the shock-induced jump). This indicates the vortex apparently sweeps back along that line essentially during that period. At station 80/05 the loading is significantly less than V6QS during the same period, and thereafter it rises to reach a maximum at 20 milliseconds, indicating that the vortex sweepback is then less. From these observations it can be concluded that the leading-edge vortex has a sweepback angle that decreases with time beginning at about six milliseconds.

The effect of the vortex-induced loading on the bending of a wing could be significant even for this 2.1-psi blast because it appears to be greatest near the wing tip. Estimation of the vortex effect on structural response however, requires a means for prediction of the vortex-induced loading distribution over the wing.

There is a significant apparent lag in the decay of the measured loading relative to the decay in the blast flow. Over a substantial part of the wing the loading remains well above the preintercept value for 30 to 40 milliseconds, whereas the blast flow decays completely to zero by 25.7 milliseconds.

6.3.2 Intercept 9B-A2-2; $\phi = 90.3$ deg., $\Delta p_s = 4.0$ psi (Fig. 28)

For the 4.0 psi intercept at 90.3 degrees from head-on α_I was 18.0 degrees and t_{v+} was 22.9 milliseconds for this second near-side-on blast intercept. Again, the loading impulse during the shock-diffraction period is relatively small over most of the wing compared with the post-diffraction loading history, except for the inboard rearward stations, where the magnitude of the post-diffraction loading is small.

The loading during the post-diffraction period differs considerably from V6QS essentially all over the wing. Over a large part of the wing, particularly where the vortex effects are marked, the loadings are higher than the V6QS values by two to three times the shock-induced V6QS jump. These higher loadings are largest along a line passing through

40/05 and 60/45, which is believed to be about the leading-edge vortex line at maximum sweepback. The period of higher loading generally lasts 10 to 15 milliseconds, depending upon the location on the wing.

The effect of the apparent leading-edge vortex on the loading history is quite marked at nearly all the stations, but particularly at the forward and outboard stations. The initial rearward sweeping back of the vortex can be traced by following the second peak in loading (after shock arrival) along the 0.80b/2 line; at stations 80/25, 80/45 and 80/65 the second peak occurs at about 1, 2 and 3 msec after shock arrival, respectively. The subsequent movement of the vortex can be seen along the 0.60b/2 chordline where the loading histories are essentially similar timewise to those for $\Delta p_s = 2.1$ psi (Run 9B-A1). At maximum sweepback the vortex would appear to leave the trailing-edge of the wing inboard of 0.80b/2. Later, increased loading is reached at stations 60/05 and 80/25 to 80/65 indicating the vortex sweepback is decreasing; this occurs between 20 to 25 milliseconds after shock arrival.

The general motion of the apparent vortex, in summary, from the measured loadings appears to be to sweep back from the leading edge to its most rearward sweep in about 4 milliseconds. It remains there for 8 milliseconds or so, and then gradually decreases its sweepback at a slow rate. The blast flow at the sled decreases to zero in 22.9 milliseconds, which is about the time the loading at the forward and tip stations 60/05, 80/25, 80/45 and 80/65 peak. So it can be seen that there is a considerable lag in the loading, which is attributed to the vortex-type flow pattern.

The loadings are again considerably higher than the V6QS values at the shock jump, being greater by up to three times the jump.

6.3.3 Intercept 9B-A2-1, $\phi = 20.1$ deg, $\Delta p_s = 2.0$ psi. (Fig. 29)

For the 2.0 psi intercept at 20.1 degrees from head-on, α_I was 5.6 degrees and t_{v+} was 13.8 milliseconds for this frontal blast intercept. Because the intercept is nearly head-on, the diffraction period is very short. The diffraction-period loading is, again, very small in terms of

impulse (time integral) in comparison with the post-diffraction loading for all stations, with a few exceptions such as at 40/85 where the post-diffraction loading is small.

Any vortex effect on the loading is not as readily identifiable as for $\phi \approx 90$ degrees, although there is significant difference in loading from the V6QS values forward of 0.65c between 0.40b/2 and 0.70b/2 and along the 0.80b/2 chordline. A leading-edge vortex may be present, as indicated by the tests of Reference 12 (See Sect. 6.1), but any effect on transient loading may be difficult to identify because of the small peak angle of attack (5.6 deg.).

The shape of the loading history generally is similar to the V6QS loading although the measured loadings are significantly higher over large areas of the wing, as noted. The biggest loading excesses over V6QS are about equal to the V6QS jump at the shock. These loadings continue to be higher than V6QS well beyond the 13.8 milliseconds for the blast flow to decay to zero.

There are marked oscillations in the loading at positions along the 0.80b/2 and 0.90b/2 chordlines which are believed to be indicative of buffeting. The test data by Ray and Taylor (Ref. 17) indicate buffeting may occur in this range of Mach number and angle of attack, although it must be recognized that the wing used differs significantly in sweepback angle, thickness ratio and aspect ratio. The significance of these unsteady airloads to an aircraft structure remains to be examined.

6.3.4 Intercept 9B-A3-1, $\phi = 20.1$ deg, $\Delta p_s = 3.6$ psi (Fig. 30)

For the 3.6 psi intercept at 20.1 degrees from head-on, α_I was 7.0 degrees; t_{v+} was not determined because the second blast shock arrived before the blast particle velocity decayed to zero at the sled. This was the second frontal blast intercept. The results are quite similar to those of Intercept 9B-A2-1 for the same intercept angle but a 2.0-psi blast shock. This might be expected as the peak angle of attack is only increased to 7.0 degrees from 5.6 degrees of the 2.0-psi intercept. The diffraction loading, in terms of impulse, also generally appear to be

comparatively small relative to the post-diffraction loading, except possibly for near the trailing edge and the wing root where the post-diffraction loadings are small.

The post-diffraction loading compares fairly well near the trailing edge with V6QS except near the tip. Outboard of $0.30b/2$ the measured loading is significantly greater than V6QS for stations between the leading edge and $0.45c$. The largest excesses are, as for $\phi = 20.1$ degrees and $\Delta p_s = 2.0$ psi, about equal to the V6QS jump at the shock. Where the loading is greater than V6QS, it remains greater until well after the blast flow decays to zero, as for the 2.0 psi test.

There is no clear indication of a leading-edge vortex, but the peak angle of attack is only 7.0 degrees. Along the $0.80b/2$ chordline there are again large fluctuations in loading indicative of buffeting, particularly at the rearward stations.

6.3.5 Intercept 9B-A2-3, $\phi = 134.9$ deg, $\Delta p_s = 2.0$ psi. (Fig. 31)

For the 2.0 psi intercept at 134.9 degrees from head-on, α_I was 9.4 degrees and t_{v+} was 56.5 milliseconds for this intercept from the rear quadrant. The magnitude of the peak loading during the diffraction period for this intercept from the rear sector is higher than during the post-diffraction period at nearly all locations on the wing. The duration of the diffraction loading is longer than in the other intercepts because the blast shock overtakes the wing.

The post-diffraction loading roughly seems to follow V6QS although tending to be higher, except in the region from the leading edge to about $0.65c$ between $0.40b/2$ to $0.70b/2$ and at 80/65 and 80/85 where it is significantly higher, by as much as 100 percent of the V6QS jump at the shock. It remains higher than V6QS in the inner forward region well beyond the 56.5 millisecond blast velocity positive duration at the sled. Along the $0.80b/2$ chordline the loading near the trailing edge is definitely higher than V6QS, until about 40 to 60 milliseconds, and at 80/25 it is somewhat higher than V6QS during the period from about 20 to 80 milliseconds.

A leading-edge vortex might reasonably be expected for the 9.4-degree peak angle of attack and the long blast duration as the evidence of a vortex is fairly strong for Intercept 9B-A1 at 11.4 degrees. There is some indication of one where the loadings exceed the V6QS predictions, but the characteristic signature of a vortex on the peak loading is not as distinct as for the intercepts near 90 degrees, where the peak angle of attack was 11.4 and 18.0 degrees.

7. SUMMARY OF OBSERVATIONS

The most significant features of the preceding discussion of the test results may be summarized as follows;

7.1 Effects of Blast-Induced Angle of Attack

The measured blast-induced loadings at the wing for blast-induced peak angles of attack up to 9.4 degrees generally exceeded the quasi-steady VIBRA-6 predictions by an amount as large as the jump in the predictions at blast shock arrival. At larger peak angles of attack the measured loadings frequently exceeded the quasi-steady VIBRA-6 predictions by two to three times the jump. The largest differences between measured loadings and these predictions occurred in a region of the wing between the leading edge and the 65-percent chordline from 40-percent semispan outboard.

7.2 Relative Importance of Diffractive Loading

At the blast intercept angle near 20 degrees from head-on, relative to the track, the measured peak loadings during the shock diffractive period generally were about equal to or less than the peak values during the post-diffractive period, except near the root and inner trailing-edge region. The diffractive period here is arbitrarily defined as the first millisecond following blast intercept ($0 \leq at/c \lesssim 1$). In the intercepts near 90 degrees the results were similar, except that the loading attributed to the leading-edge vortex has its highest peak during the diffractive period in many cases for transducers near the leading edge. In the 135-degree intercept, the diffractive-period peaks were significantly greater than the post-diffractive peaks nearly everywhere on the wing. The loading impulse (time integration) for the 20 and 90-degree intercepts was very small during the diffractive period compared with the post-diffractive period; at 135 degrees the loading impulse during the diffractive period by comparison was relatively more significant.

AD-A053 468

KAMAN AVIDYNE BURLINGTON MASS

F/G 19/4

MEASUREMENTS OF BLAST PRESSURES ON A RIGID 65 DEG. SWEEPBACK WI--ETC(U)

JUN 77 J R RUETENIK, R F SMILEY

DNA001-76-C-0106

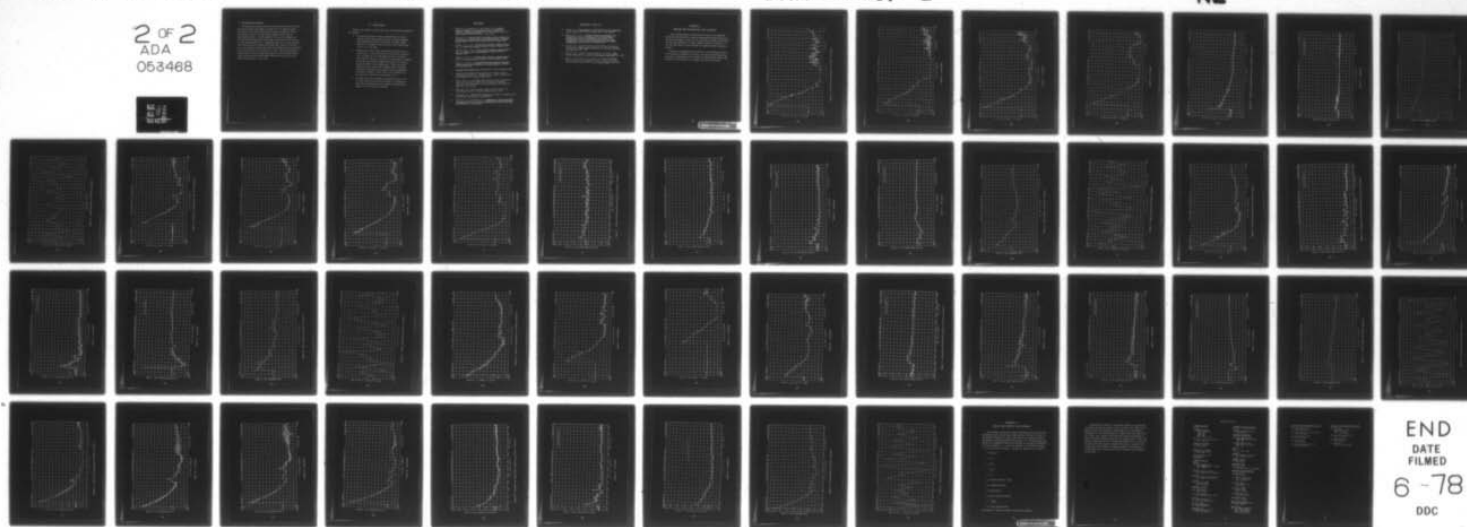
UNCLASSIFIED

KA-TR-137-VOL-1

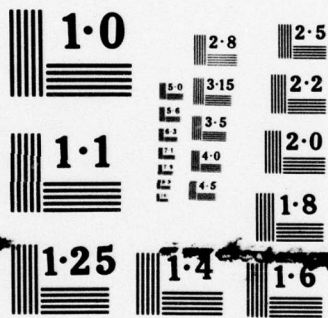
DNA-4400F-1

NL

2 OF 2
ADA
053468



END
DATE
FILMED
6-78
DDC



NATIONAL BUREAU OF STANDARDS

7.3 Nonlinear Vortex Effects

The loading histories during the post-diffractive period in tests with blast-induced peak angles of attack up to 9.4 degrees roughly followed the quasi-steady VIBRA-6 predictions, although the level of the loadings over the forward outboard regions of the wing was significantly higher. At peak angles of 11.4 and 18.0 degrees the post-diffractive loadings had large peaks with features indicative of a strong leading-edge vortex; a sweptback region of the wing extending from a position on the leading edge appreciably inboard of the wing tip to the outboard trailing edge had high loadings that were maintained until the blast flow at the sled went to zero. The post-diffractive loading histories at the large peak angles of attack differed significantly from the quasi-steady VIBRA-6 predictions over all but the inner rearward region of the wing.

8. CONCLUSIONS

Based on the results of these sled tests, the following conclusions are reached:

1. The multiple-intercept rocket-propelled-sled tests have provided useful blast pressure data for a highly sweptback wing travelling at Mach 0.76 for blast intercept angles from 20 to 135 degrees from head-on for blast overpressures in the 2 to 4 psi range.
2. Comparisons of quasi-steady linearized calculations with the test data in the post-diffraction period have indicated that, although there is some agreement over the inboard rear region of the wing, frequently the experimental loadings exceed the quasi-steady loadings appreciably, particularly toward the wing tip and leading edge. There are strong indications that these larger loadings reflect basically non-linear aerodynamic effects which cannot be adequately predicted by simply a linear theory of the VIBRA-6 type for the blast conditions of the present tests.
3. The peak diffractive loadings were generally equal to or less than the post-diffractive loadings for intercepts at about 20 and 90 degrees and were generally significantly greater for the 135-degree intercept.

REFERENCES

1. Hobbs, N.P., Zartarian, G., and Walsh, J.P., A Digital Computer Program for Calculating the Blast Response of Aircraft to Nuclear Explosions, Air Force Weapons Laboratory Report AFWL-TR-70-140, Volume I, April 1971.
2. Zartarian, G., Application of the Doublet-Lattice Method for Determination of Blast Loads on Lifting Surfaces at Subsonic Speeds, Kaman Avidyne TR-91, AFWL-TR-72-207, January 1973.
3. McGrew, J.A., et al., Nuclear Blast Response Program Vibra 6, Vol. I, Program Description, Douglas Aircraft Company, 1976.
4. Giesing, J.P., et al., Nuclear Blast Response Program Vibra 6, Vol. II, Doublet Lattice Aerodynamics, Douglas Aircraft Company, 1976.
5. McGrew, J.A., et al., Nuclear Blast Response Program Vibra 6, Vol. III, Program Listing, Douglas Aircraft Company, 1976.
6. Wolf, I. O., et al., An Experimental Investigation of Blast-Induced Airloads and Response of Lifting Surfaces, AFFDL-TR-64-176, March 1965.
7. Holloman Track Capabilities, MDC-TDR-62-9, HAFB, September 1962.
8. Engineering Drawings of Wing Construction, Kaman Sciences Corporation Drawings Nos. X-400163 Rev F, dated 24 March 1976, and X-400165 Rev C, dated 26 March 1976.
9. Valle, Joe, Jr., Test Event Report Aircraft Blast Interaction Test, Job Order No. 921DST01, Central Inertial Guidance Facility, Hdq. 6585th Test Group, Environmental Test Section, HAFB, NM, 10 June 1976.
10. Ruetenik, J.R., Load-Deflection Tests for Model, Mount and Sled, Memorandum No. 10, Kaman Avidyne, May 3, 1976.
11. Krupovage, D.J., NASTRAN Code Calculations, HAFB, 18 December 1975, Revised March and May 1976, unpublished.
12. Ruetenik, J.R., and Lewis, S.D., Computation of Blast Properties for Spherical TNT or Pentolite from Measured Pressure Histories, AFFDL-TR-66-47, October 1966.

REFERENCES (CONCL'D)

13. Brode, H.L., A Calculation of the Blast Wave from a Spherical Charge of TNT, RAND RM-1965, August 1957. (AD 144302).
14. Manro, M.E., et al., Transonic Pressure Measurements and Comparison of Theory to Experiment for an Arrow-Wing Configuration, Vol. I: Experimental Data Report - Base Configuration and Effects of Wing Twist and Leading-Edge Configuration, NASA CR-132727, October 1975.
15. Taylor, C.R., Aircraft Stalling and Buffeting, Introduction and Overview, AGARD Lecture Series No. 74, Aircraft Stalling and Buffeting, Feb. 1975.
16. Smith, A.M.O., Remarks on Fluid Mechanics of Stall, AGARD Lecture Series No. 74, Aircraft Stalling and Buffeting, Feb. 1975.
17. Ray, E.J., and Taylor, R.T., Buffet and Static Aerodynamic Characteristics of a Systematic Series of Wings Determined from a Subsonic Wind-Tunnel Study, NASA TN D-5805, June 1970.

APPENDIX A

PRESSURE AND ACCELERATION TIME HISTORIES

This appendix presents time histories of most of the measured blast-line and sled-borne transducer measurements obtained during the present test program, except for wing differential pressure data which are presented separately as small composite figures in Section 6 of the text and which are also presented as larger individual figures in Volume 2.

Material is presented here according to the chronological order of intercepts as indicated in Table 6. For each intercept blast-line pressures are presented first, followed by blastward and leeward wing pressures, total pressure at the model, and wing acceleration.

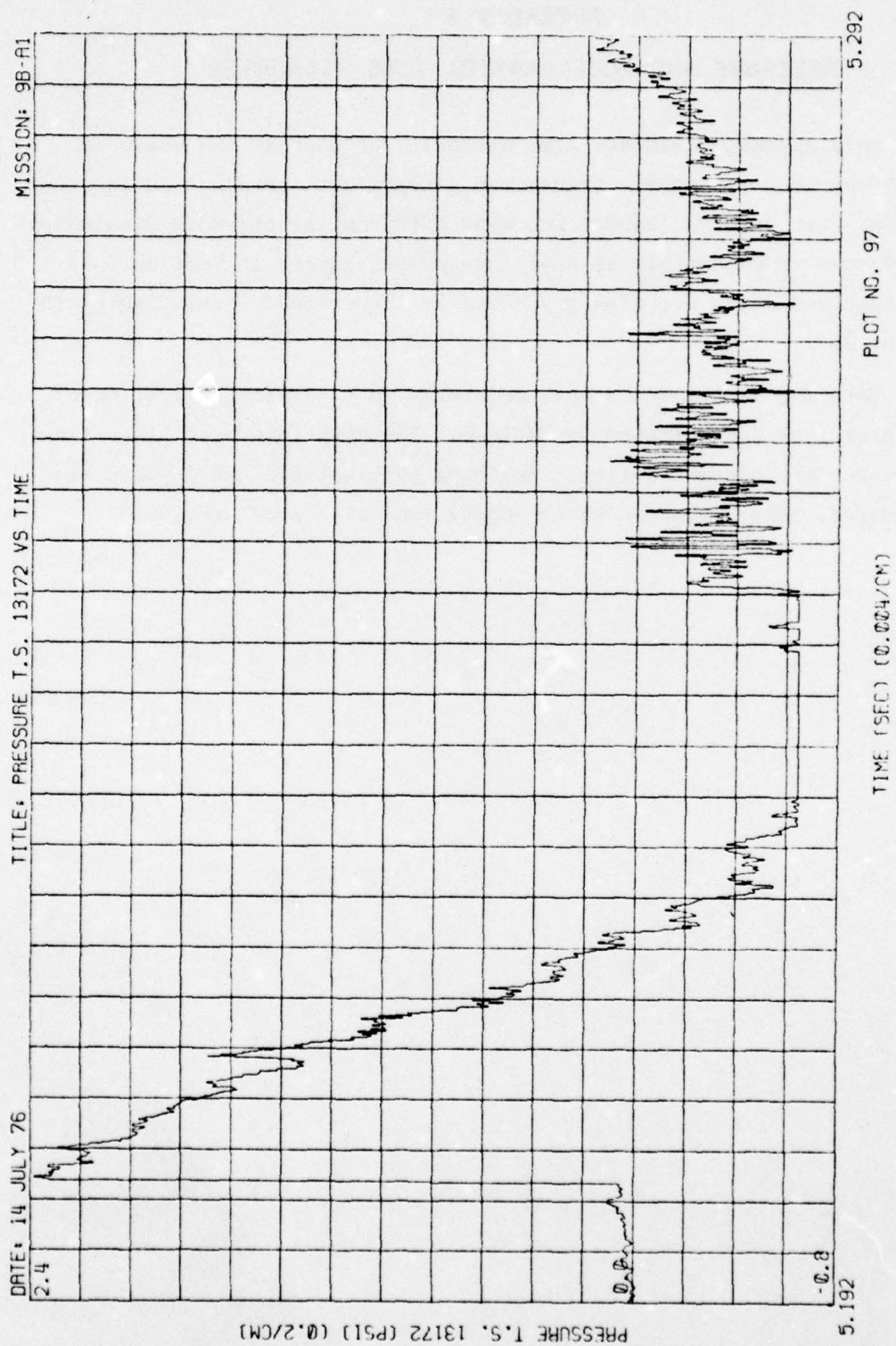


Figure 32. Blast-Line Overpressures, Run 9B-A1, Intercept 2

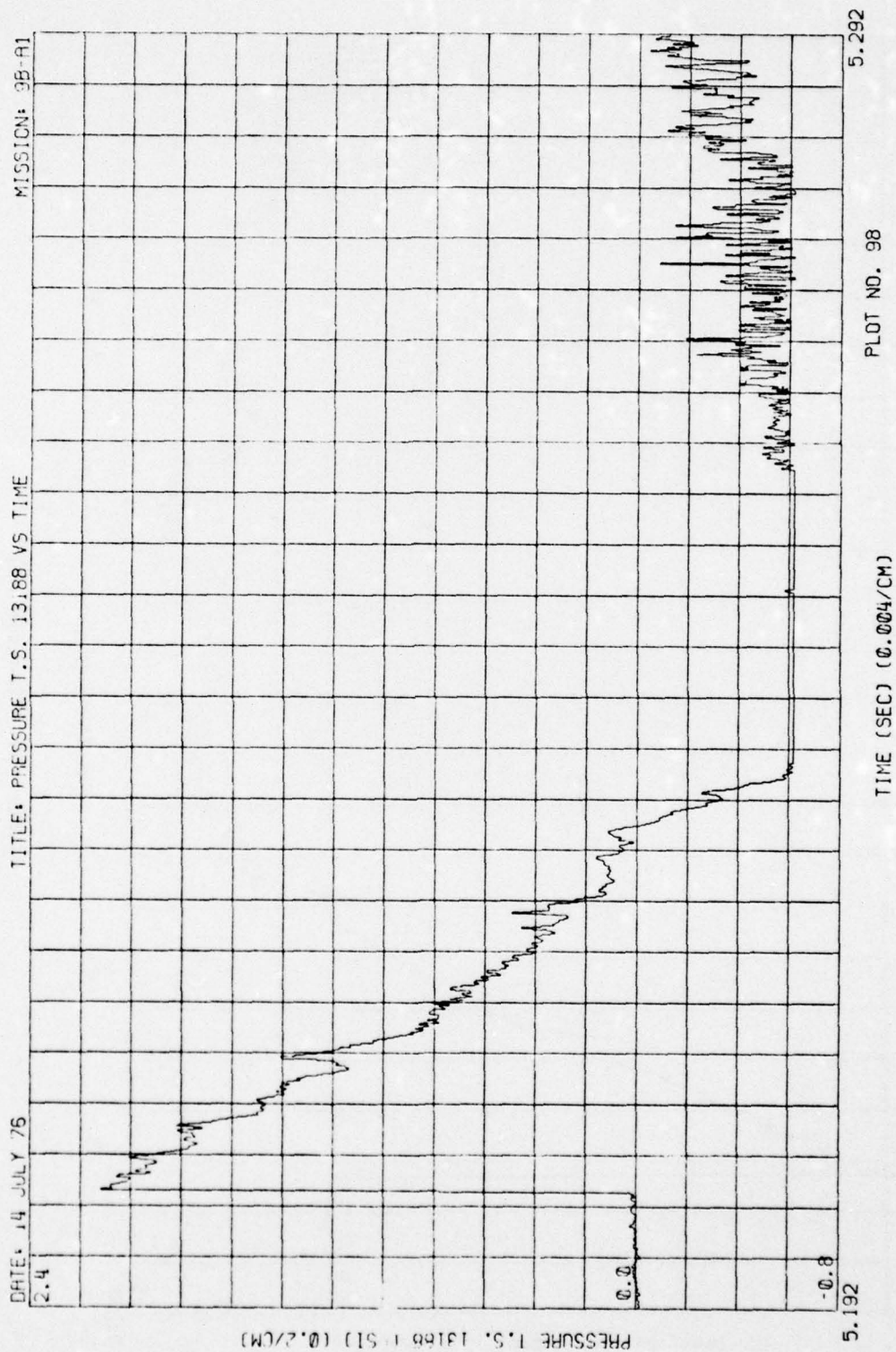


Figure 32. (Continued)

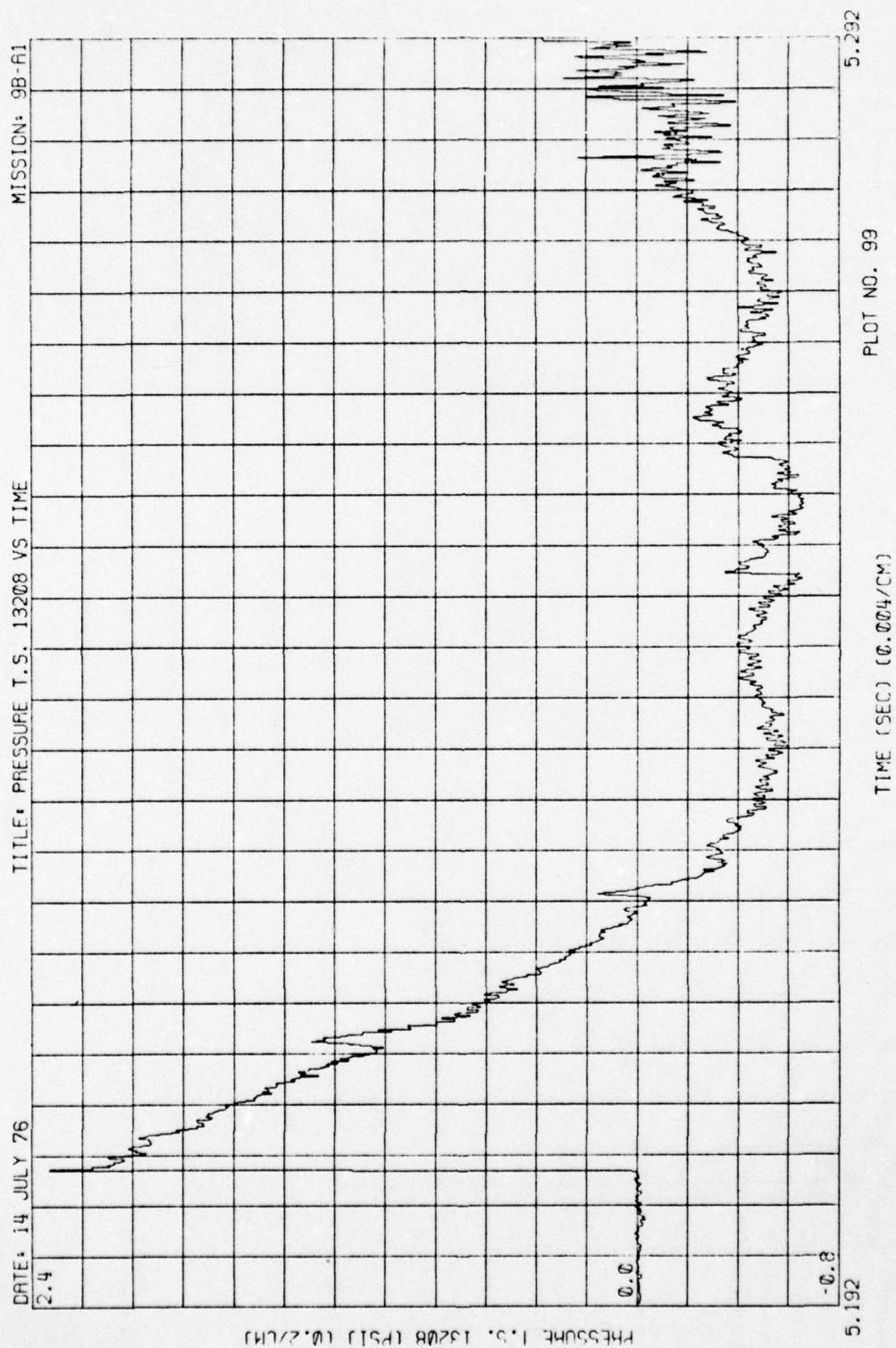


Figure 32. (Continued)

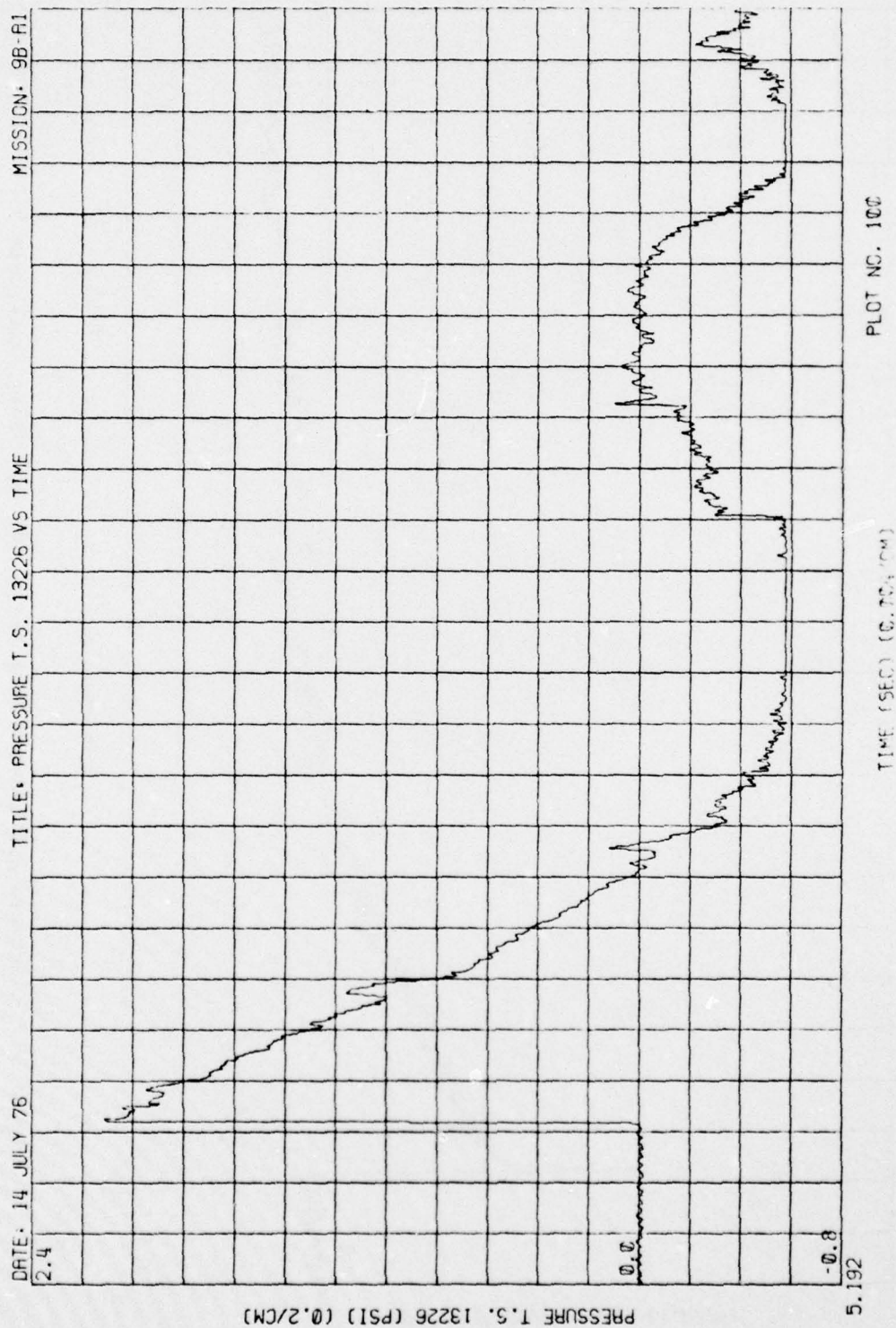


Figure 32. (Concluded)

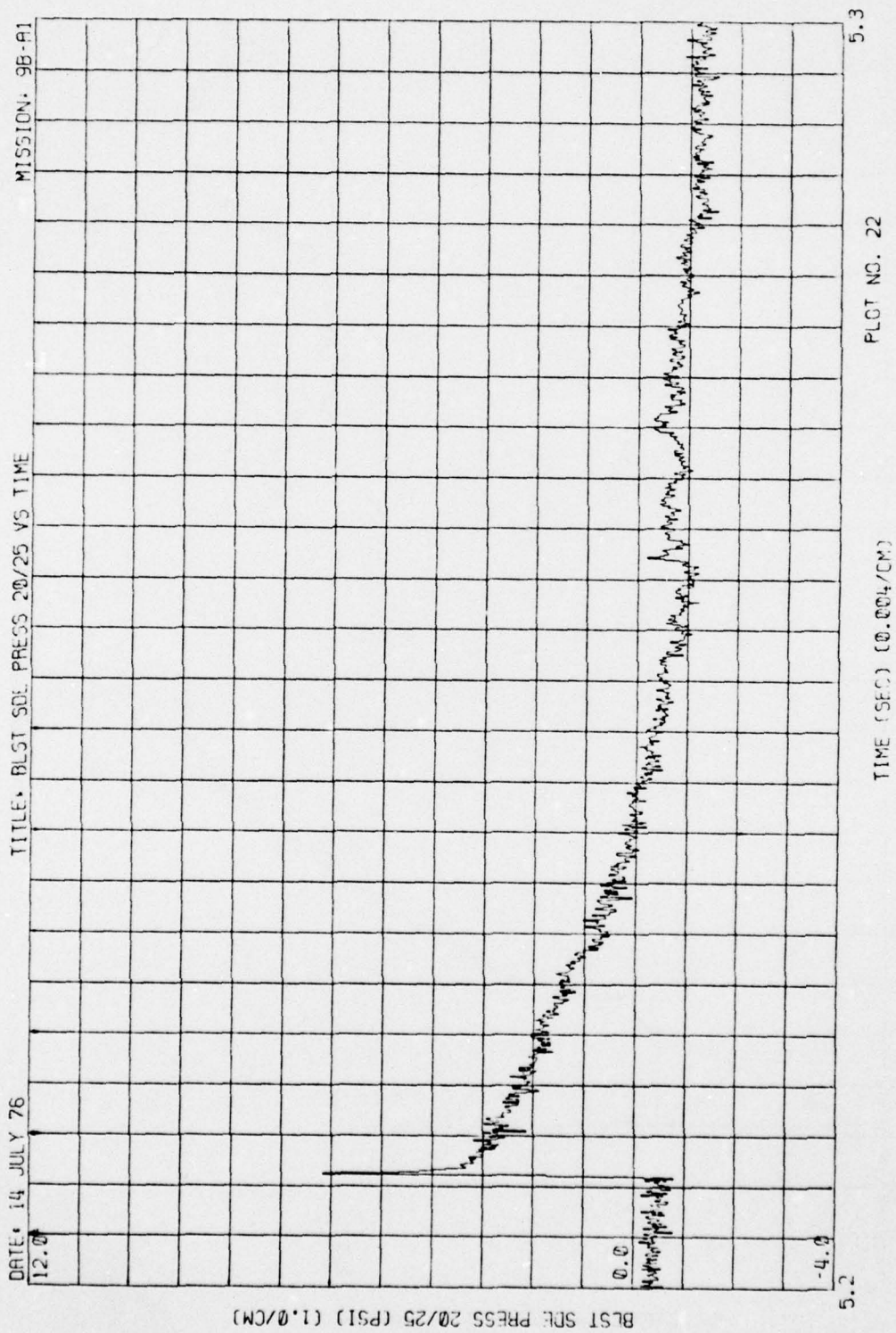


Figure 33. Blastward and Leeward Wing Pressures, Run 9B-A1, Intercept 2

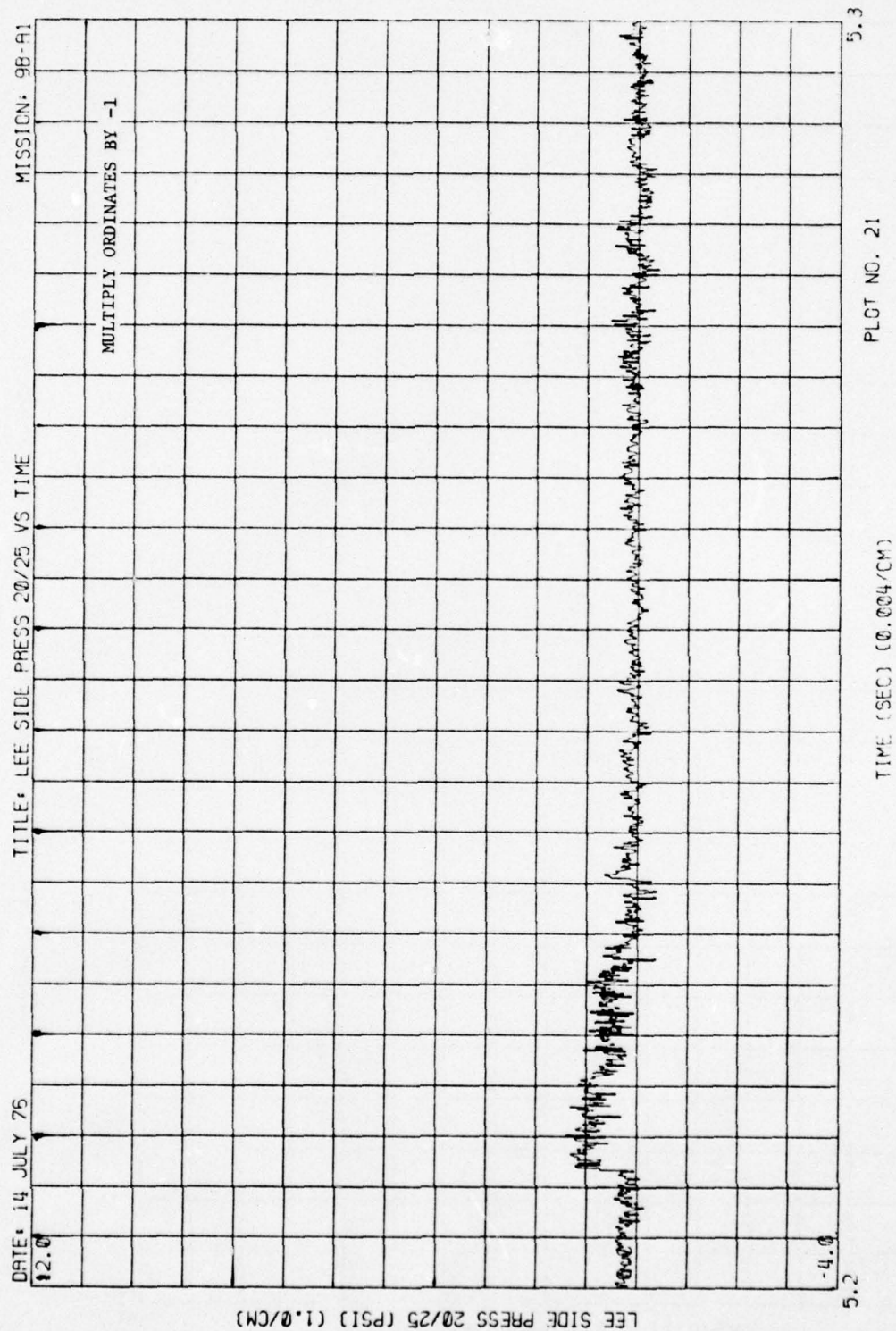


Figure 33. (Continued)

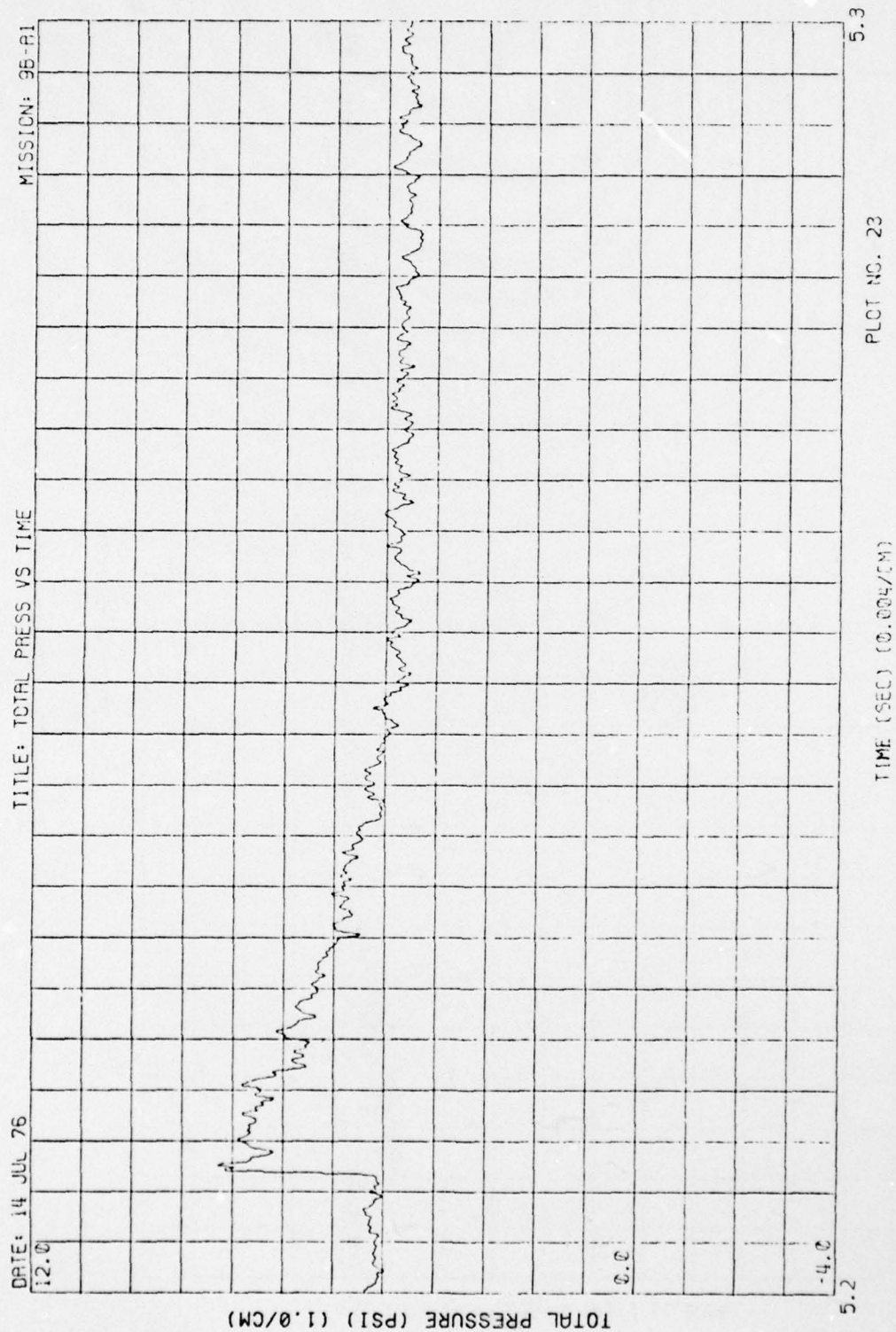


Figure 34. Total Pressure, Run 9B-A1, Intercept 2

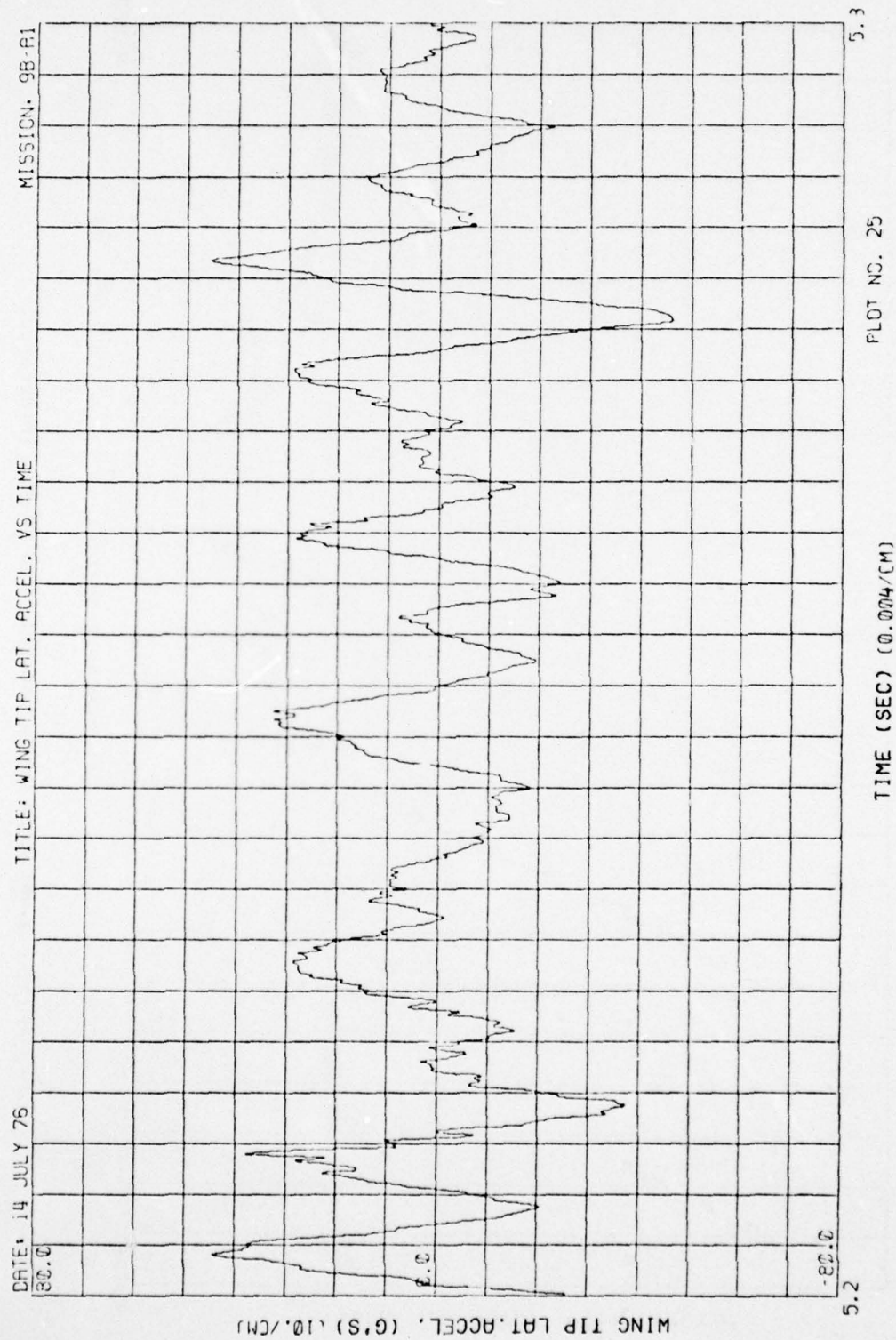


Figure 35. Wing Acceleration, Run 9B-A1, Intercept 2

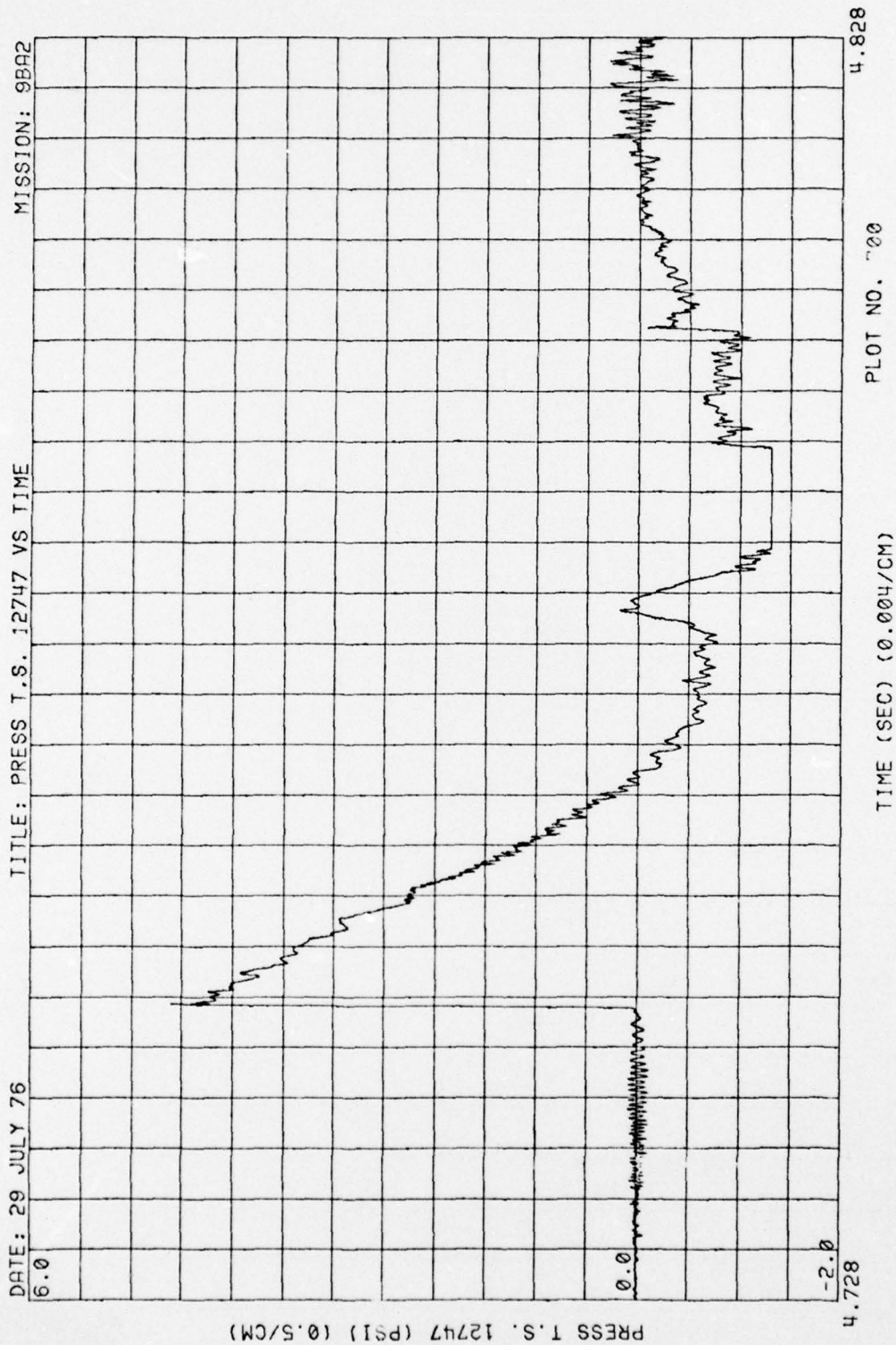


Figure 36. Blast-Line Overpressures, Run 9B-A2, Intercept 1

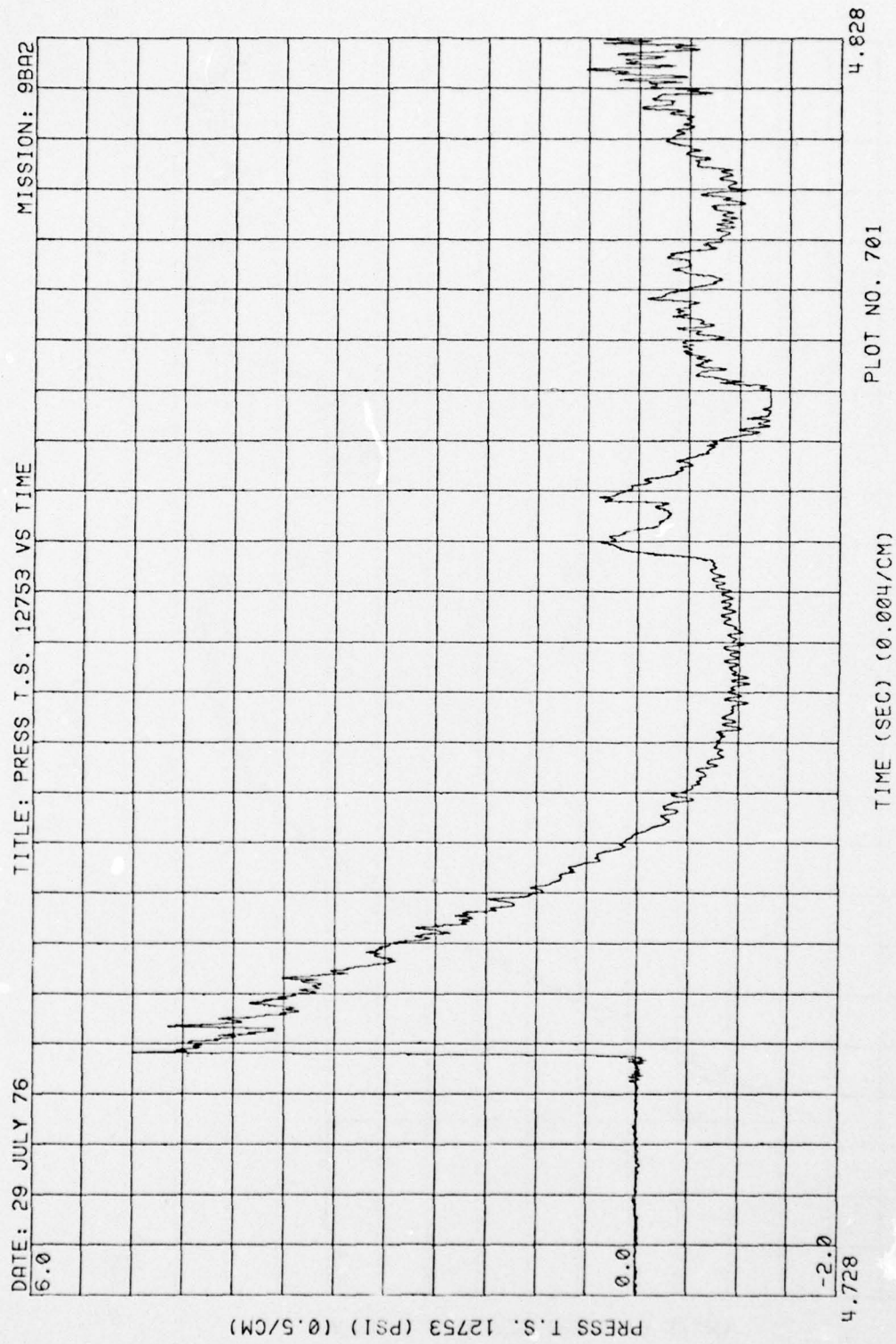


Figure 36. (Continued)

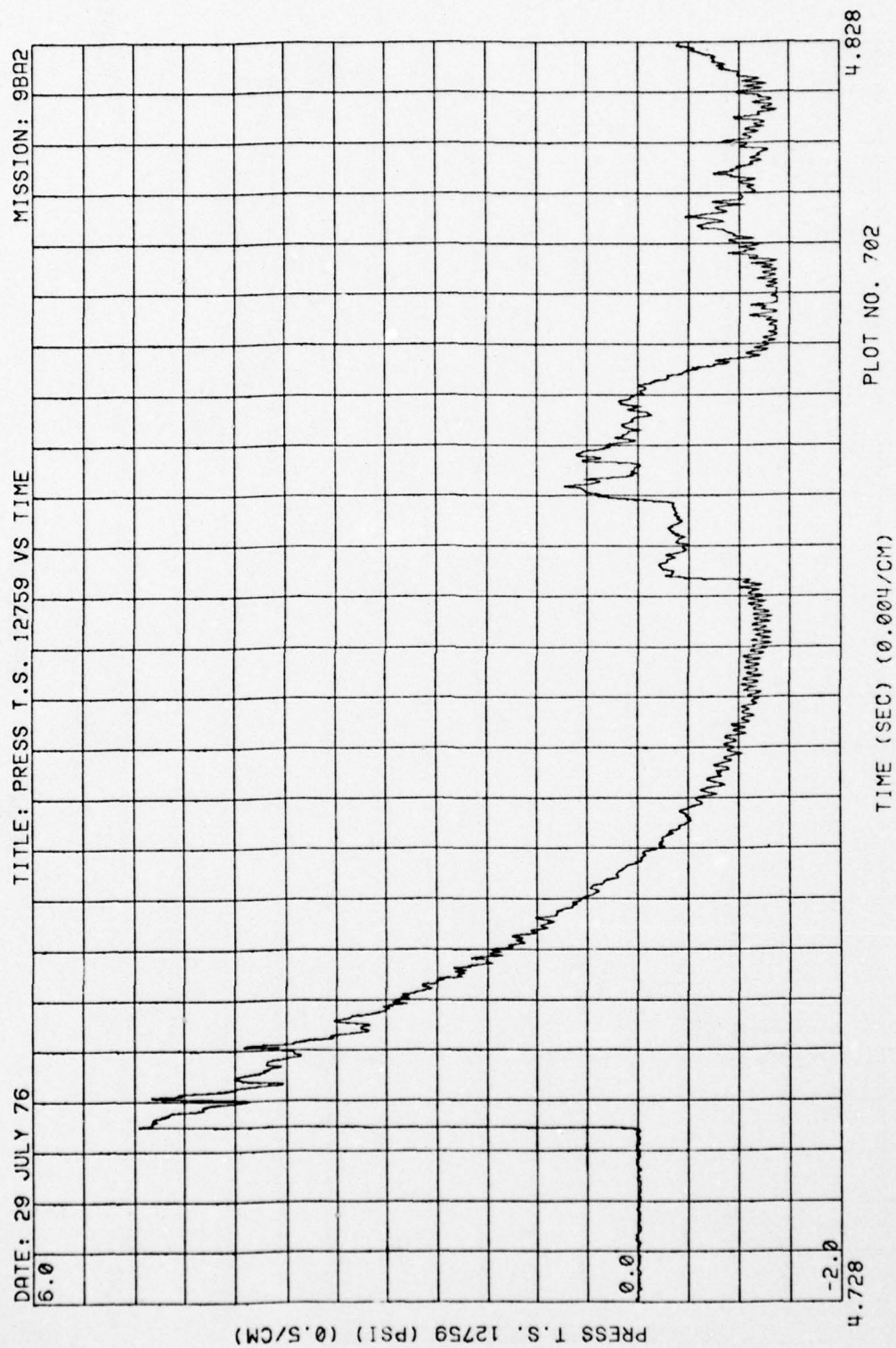


Figure 36. (Continued)

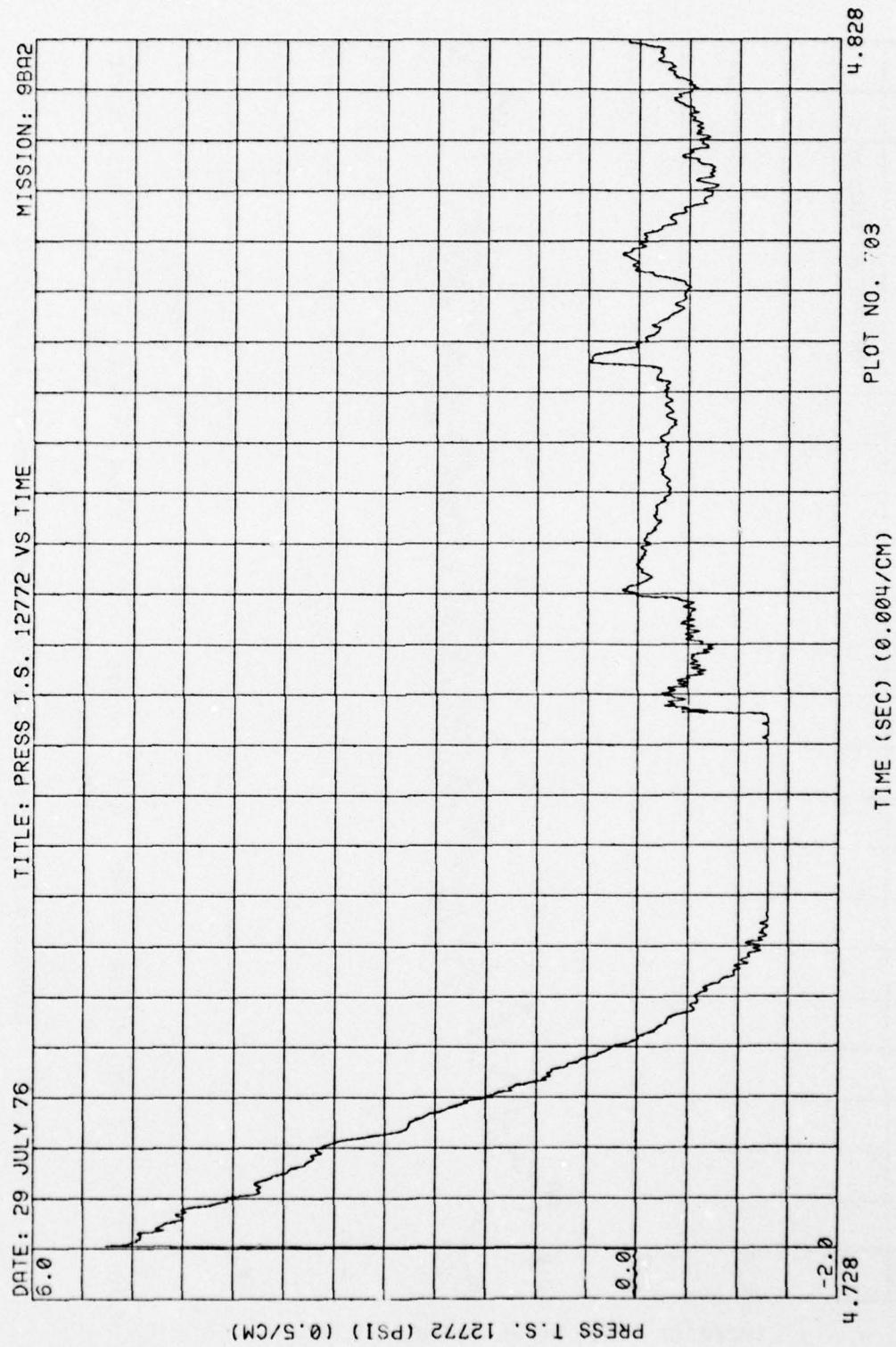


Figure 36. (Concluded)

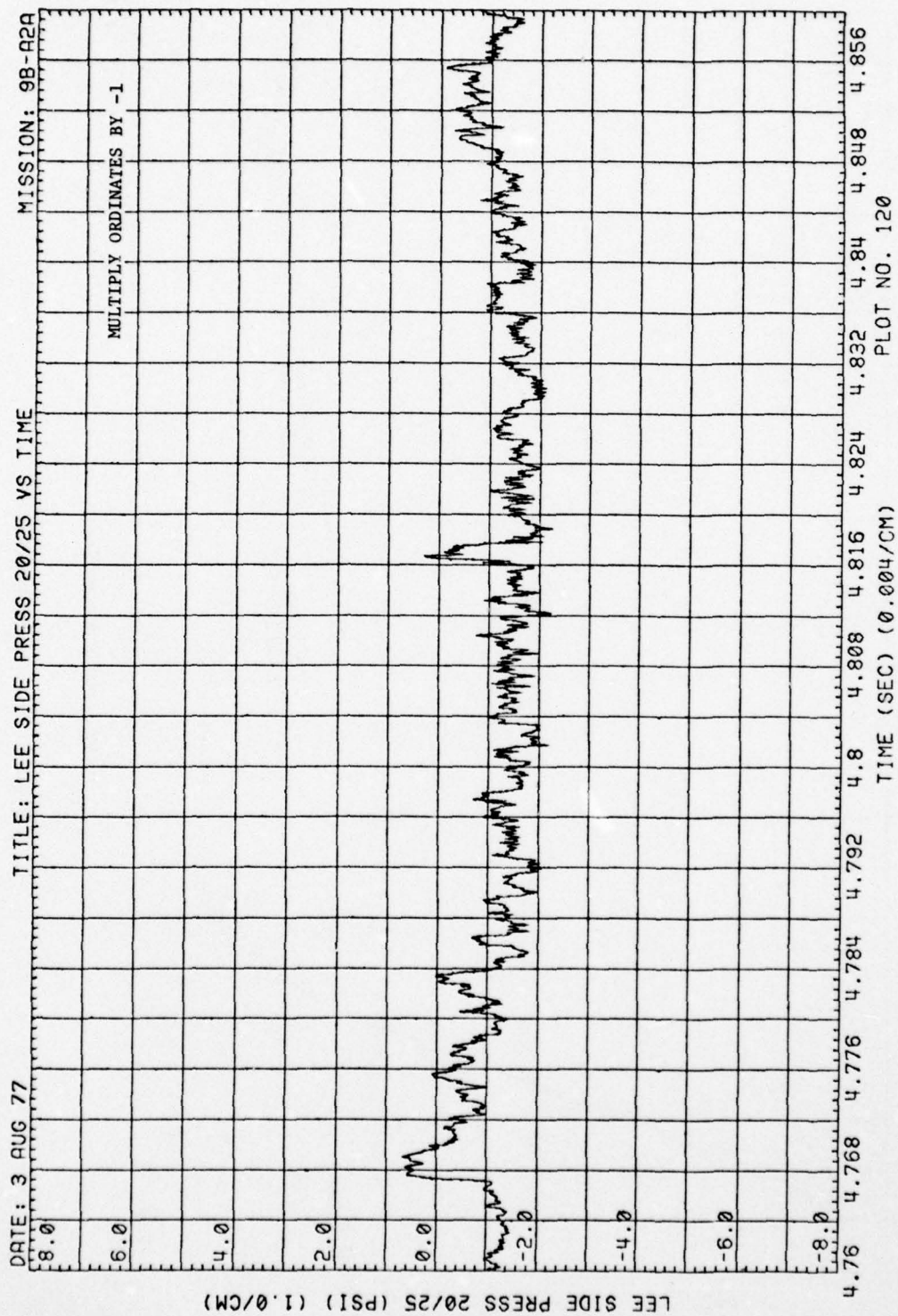


Figure 37. Blastward and Leeward Wing Pressures, Run 9B-A2, Intercept 1

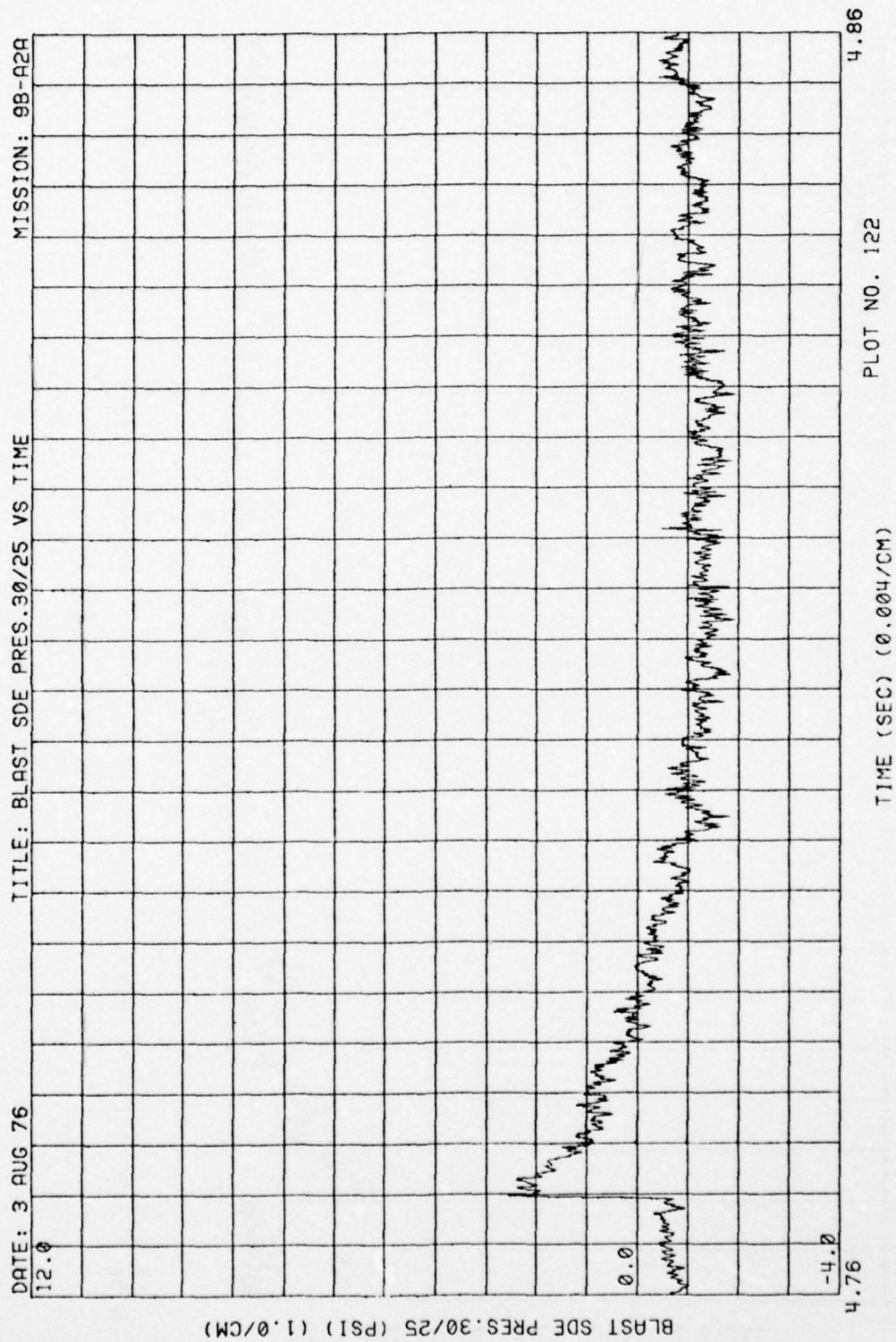


Figure 37. (Continued)

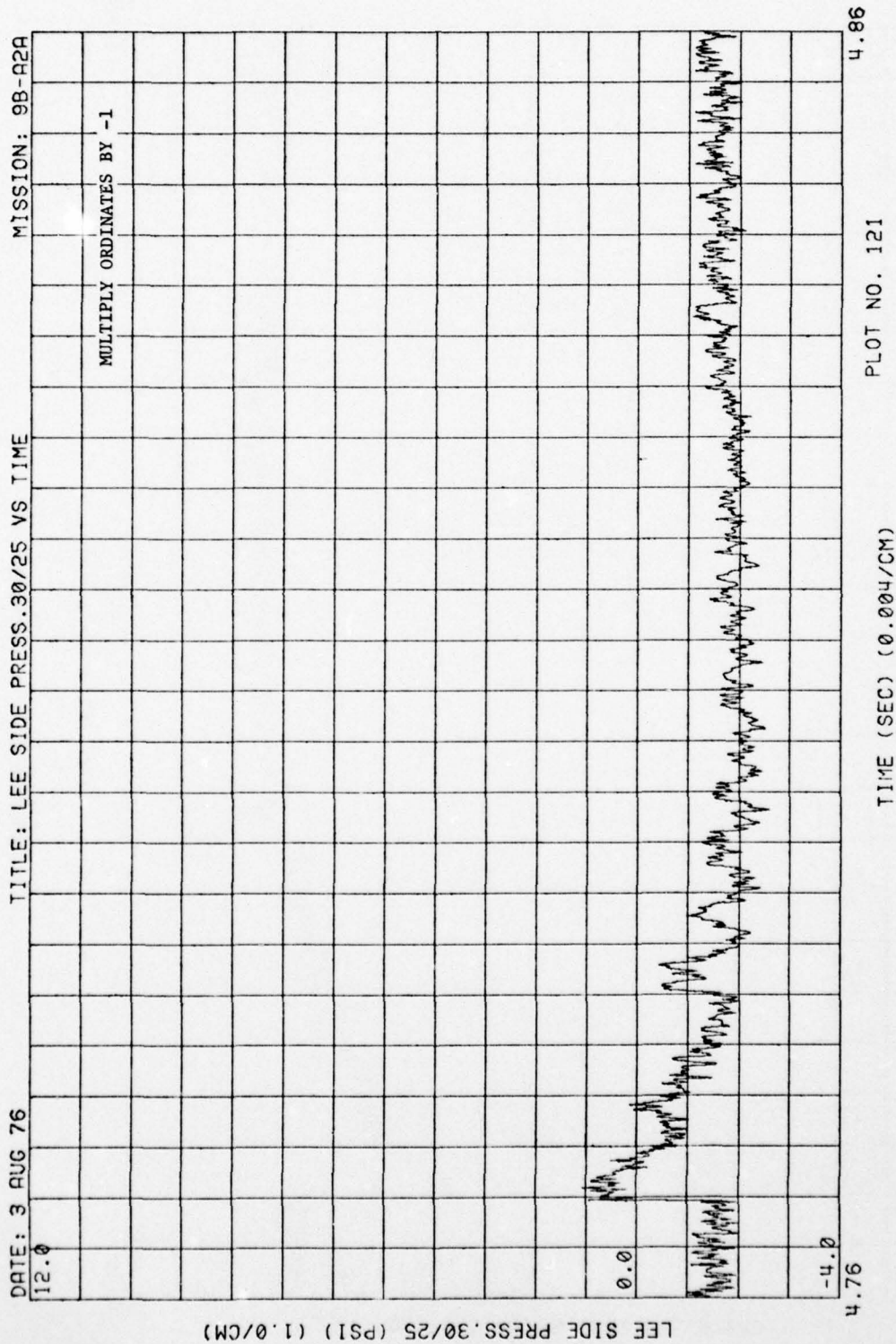


Figure 37. (Continued)

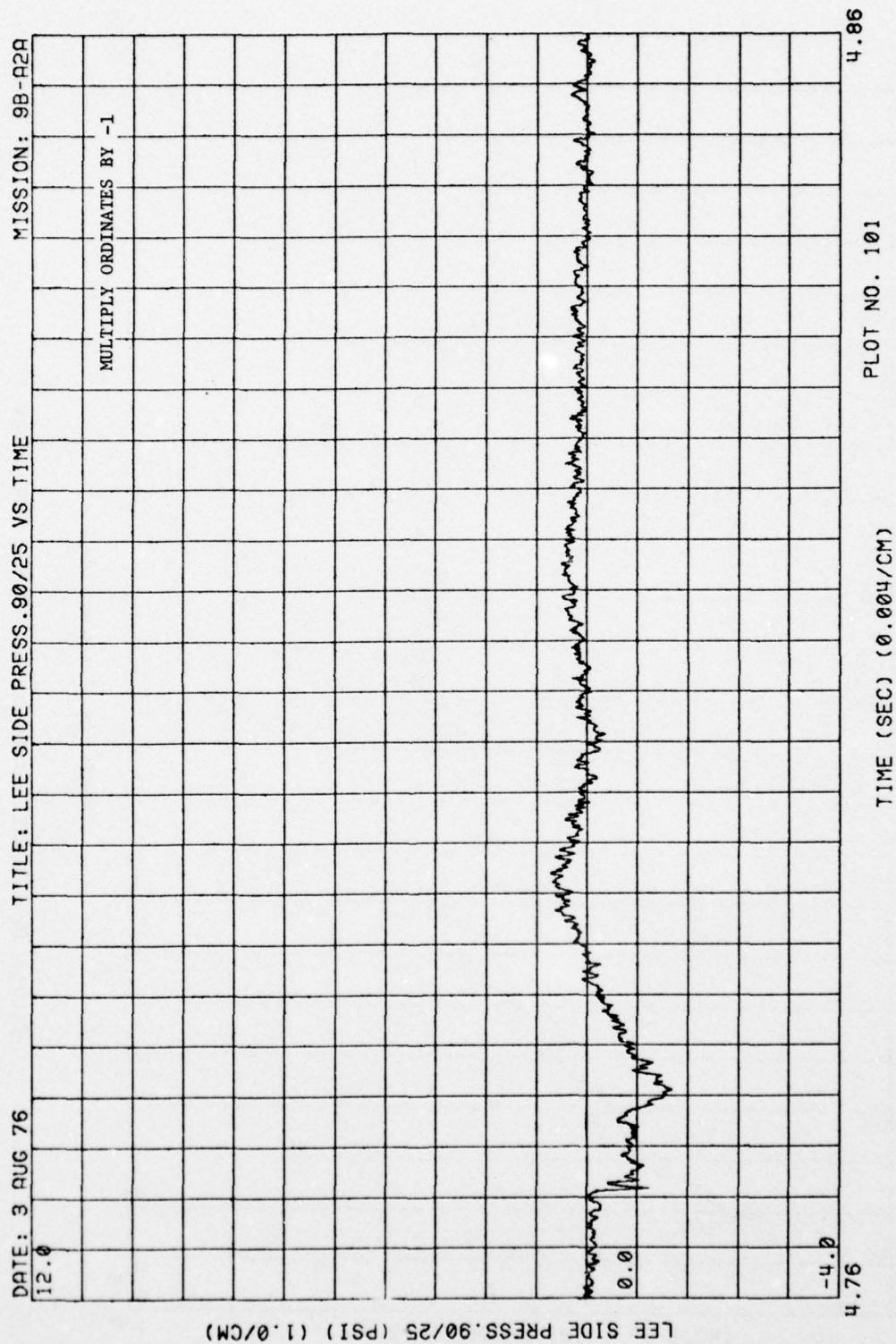


Figure 37. (Concluded)

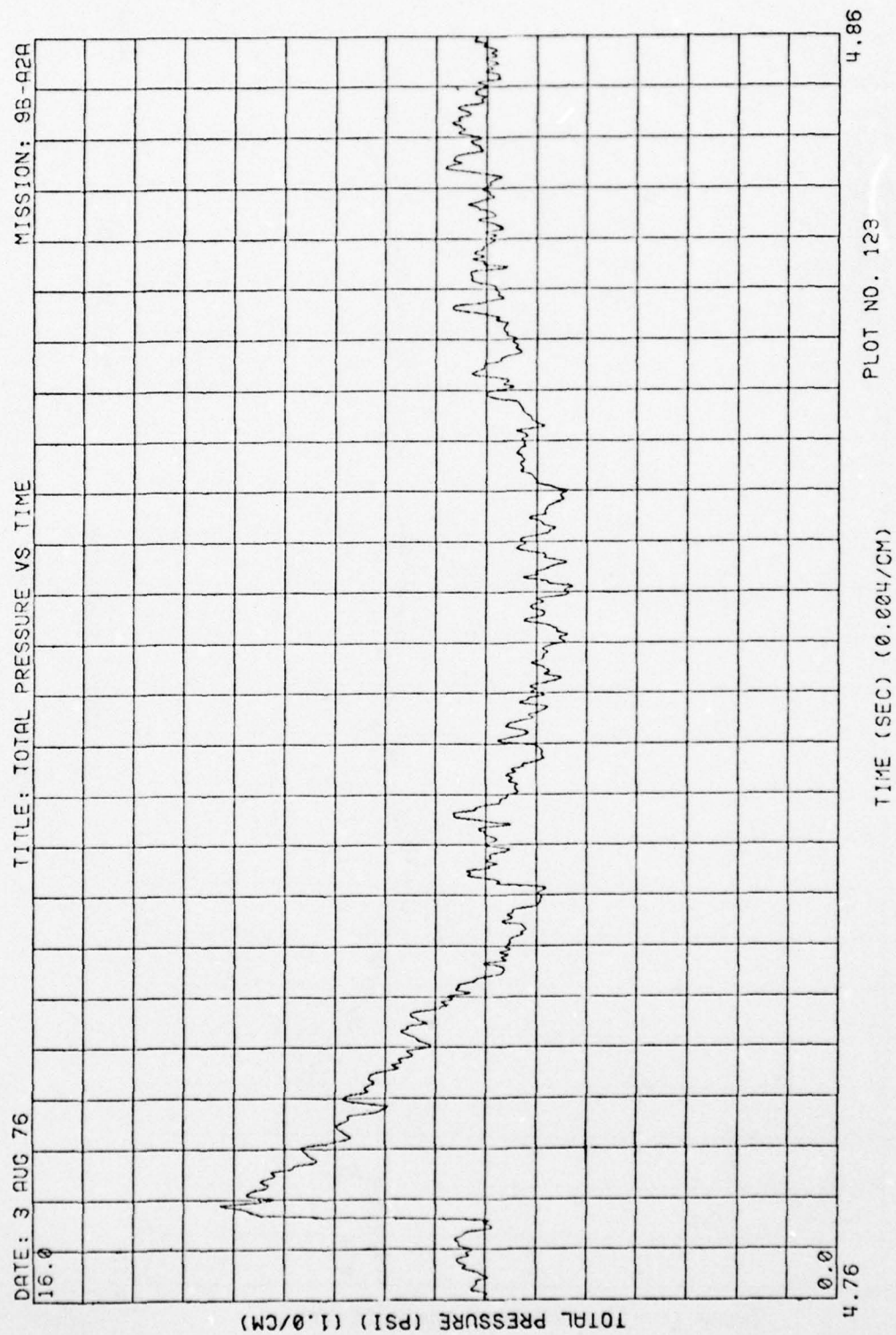


Figure 38. Total Pressure, Run 9B-A2, Intercept 1

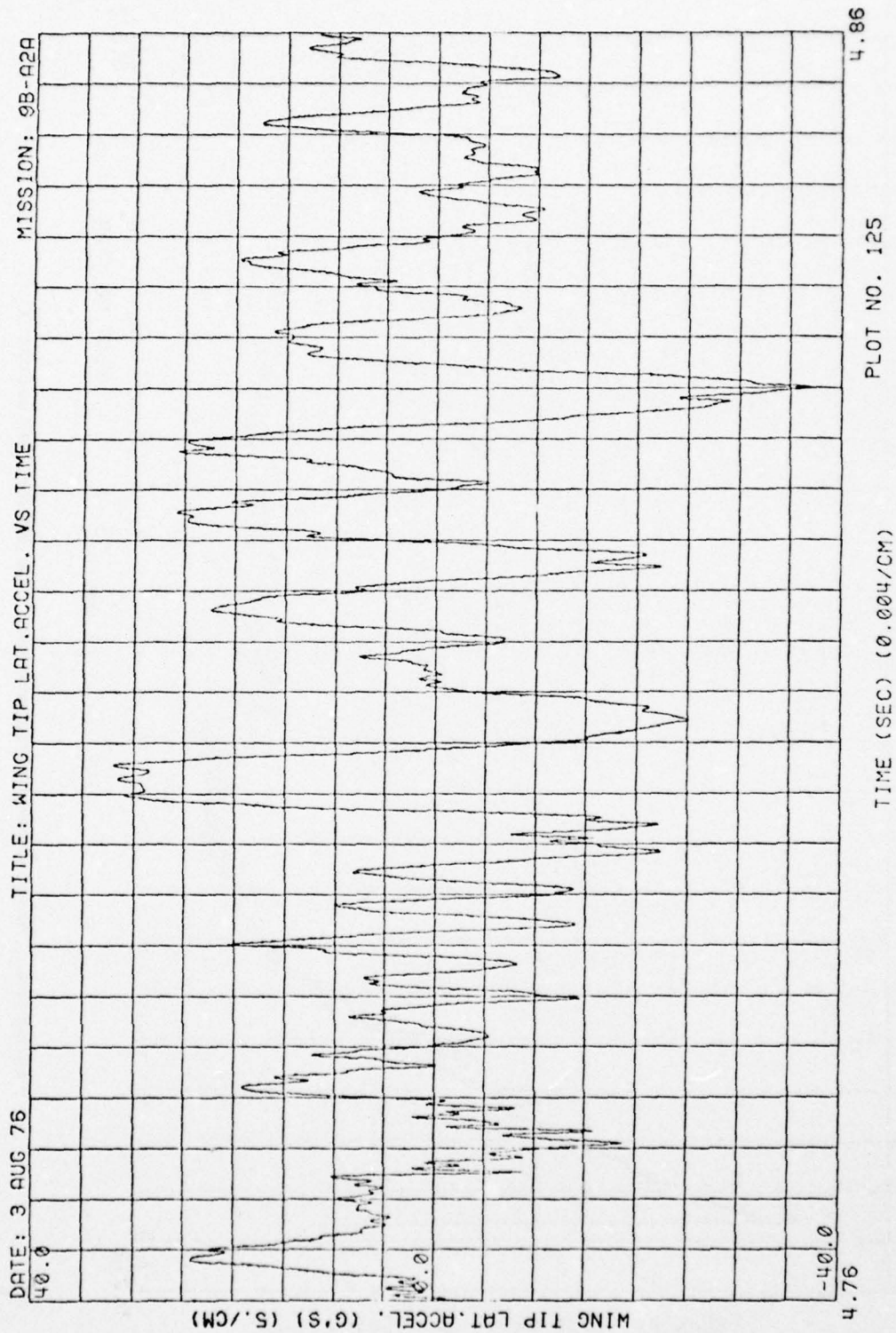


Figure 39. Wing Acceleration, Run 9B-A2, Intercept 1

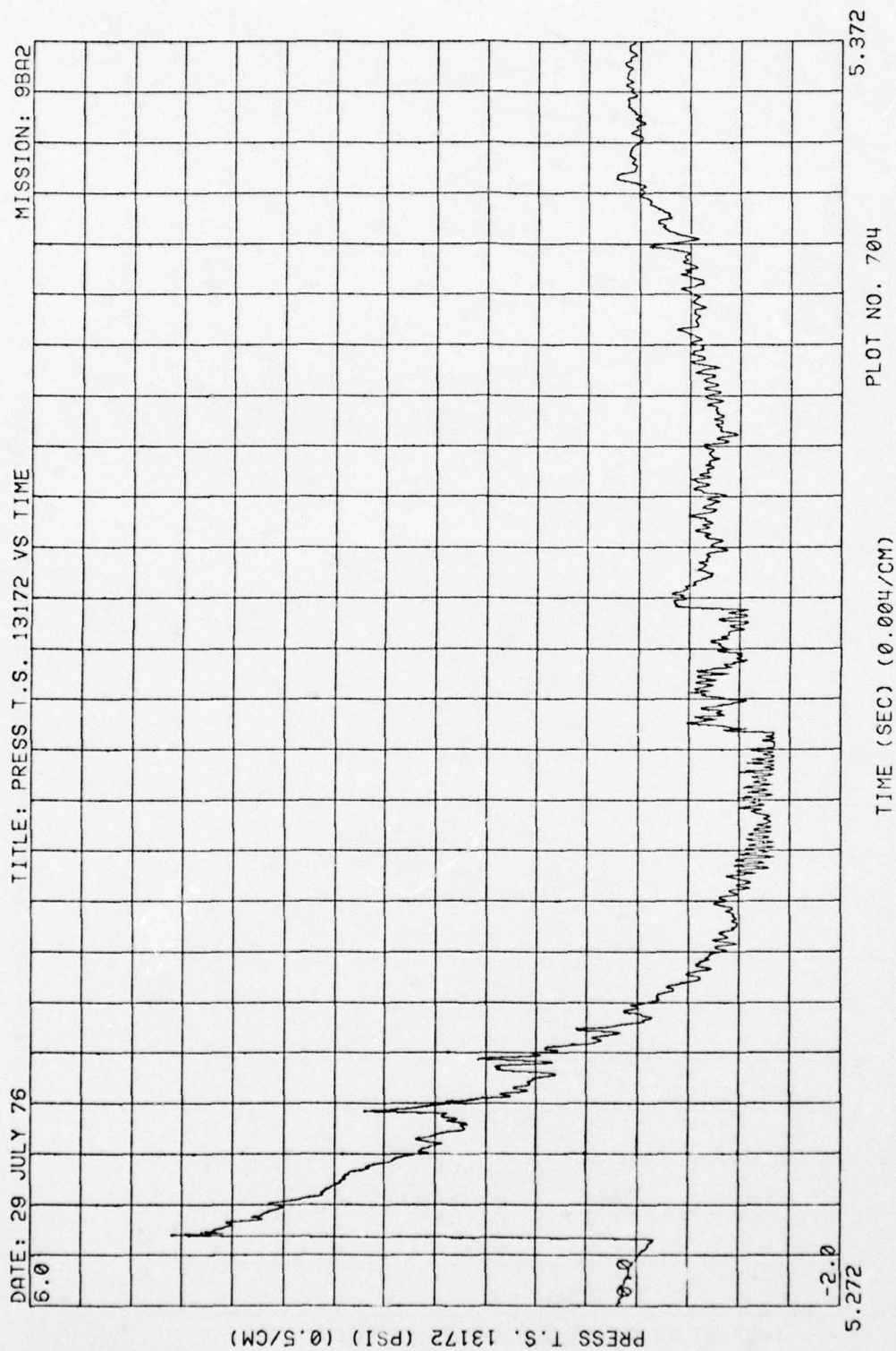


Figure 40. Blast-Line Overpressures, Run 9B-A2, Intercept 2

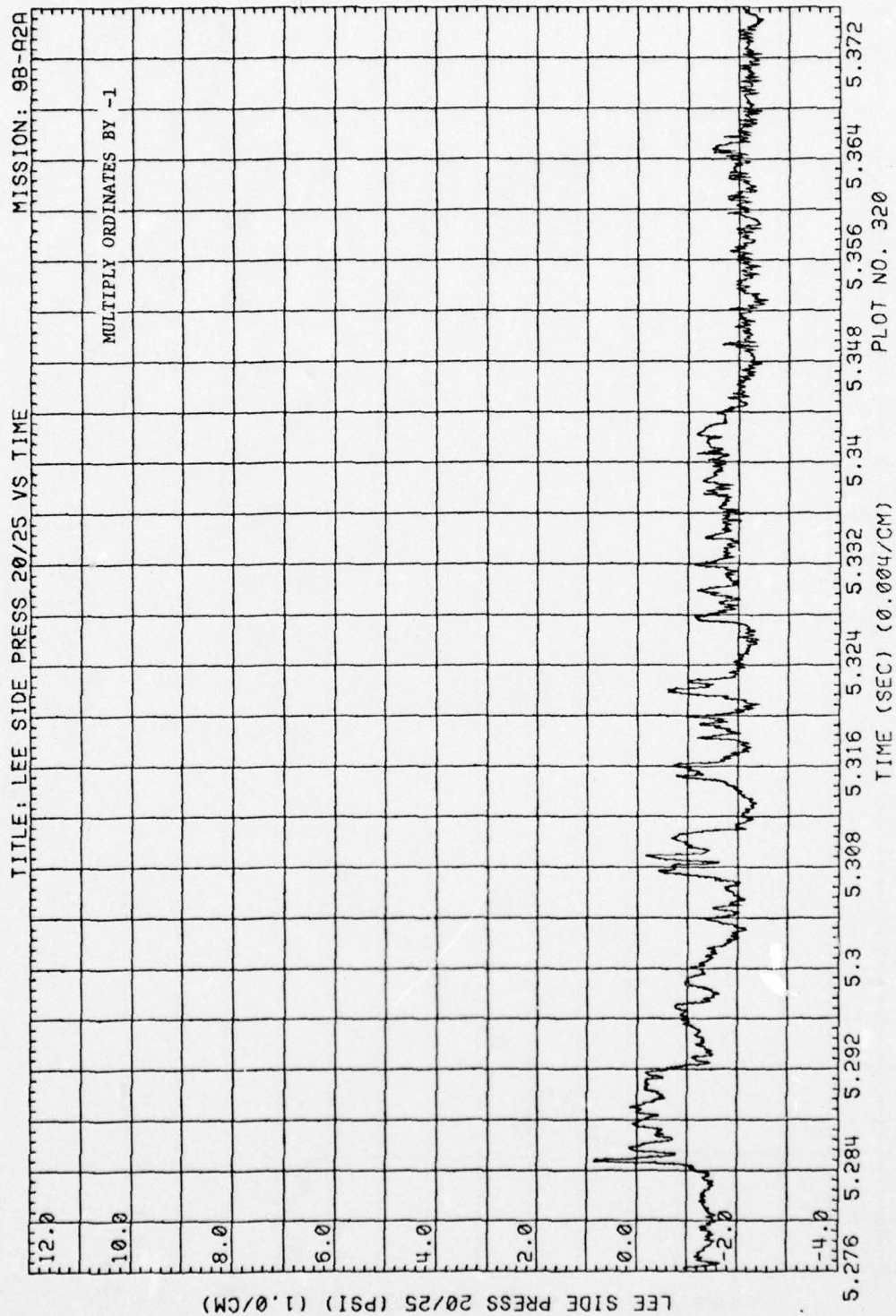


Figure 41. Blastward and Leeward Wing Pressures, Run 9B-A2, Intercept 2

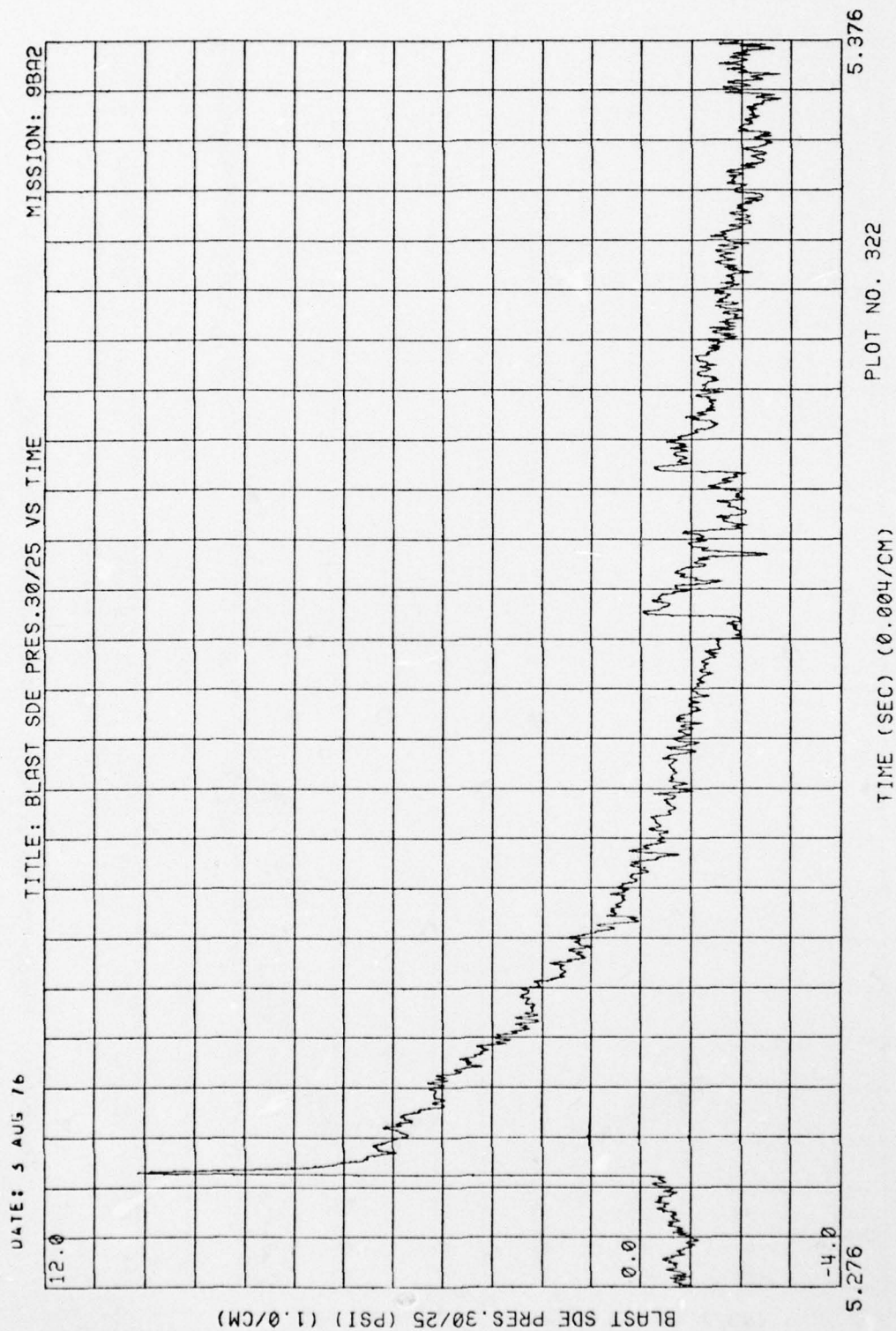


Figure 41. (Continued)

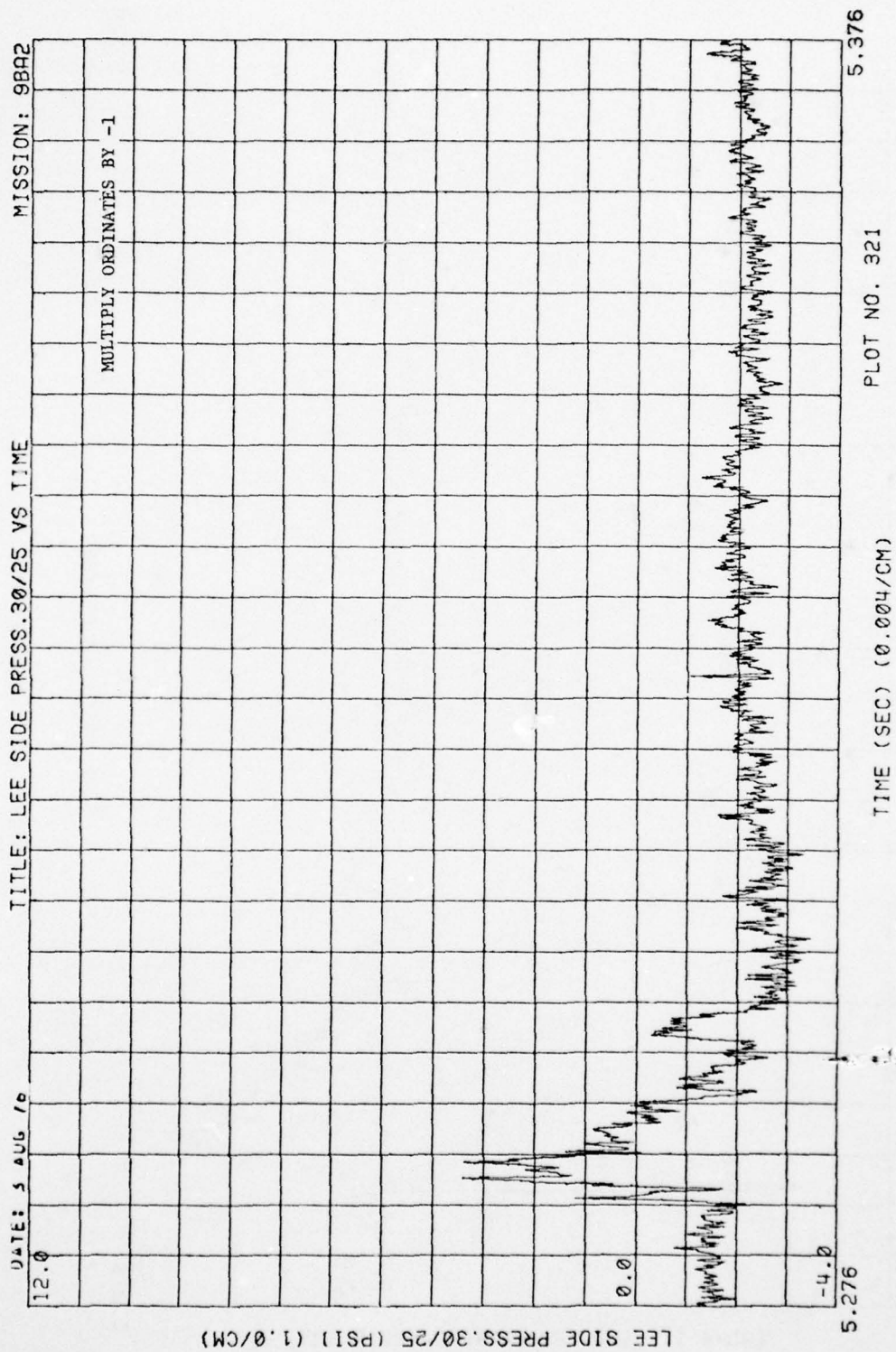


Figure 41. (Continued)

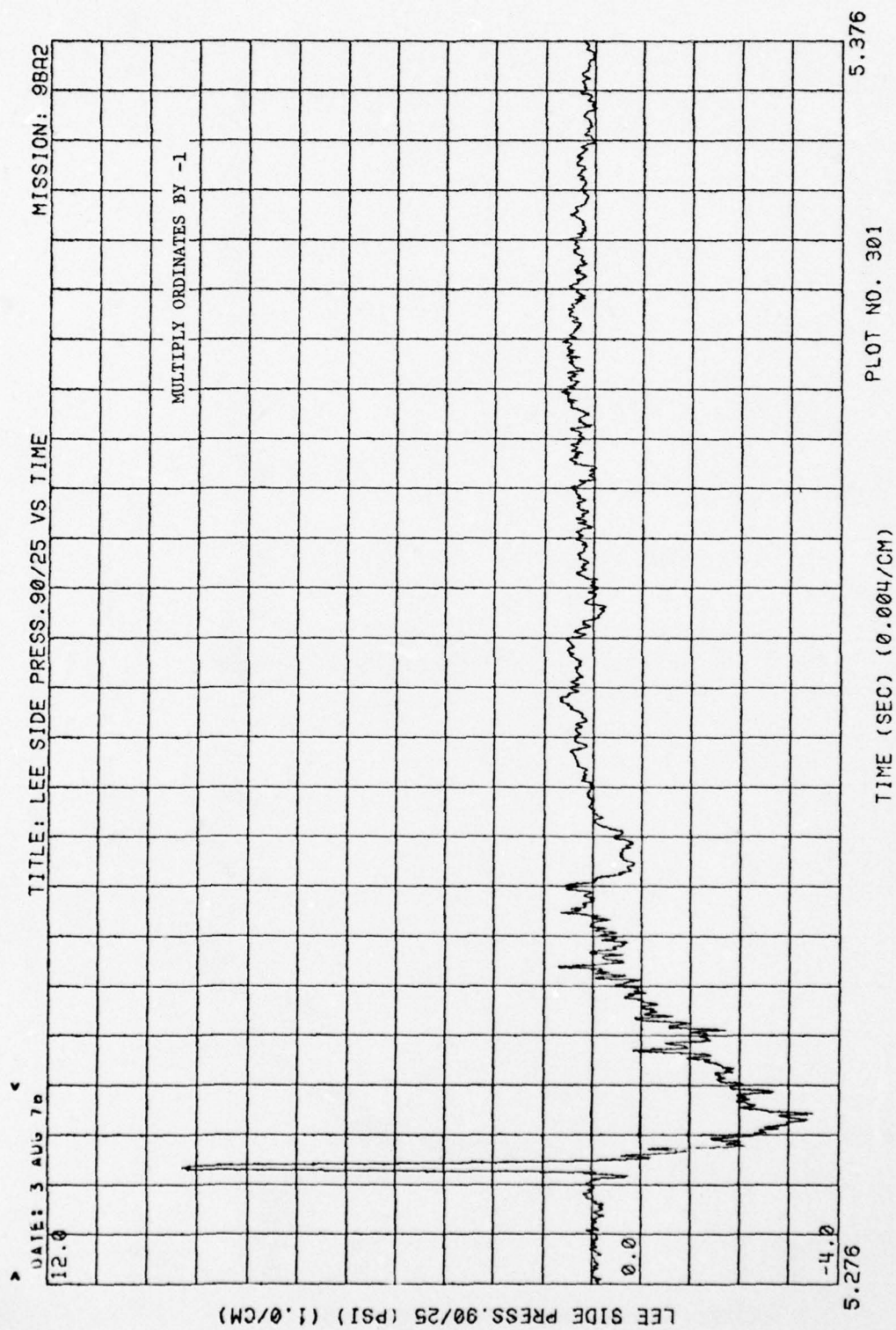


Figure 41. (Concluded)

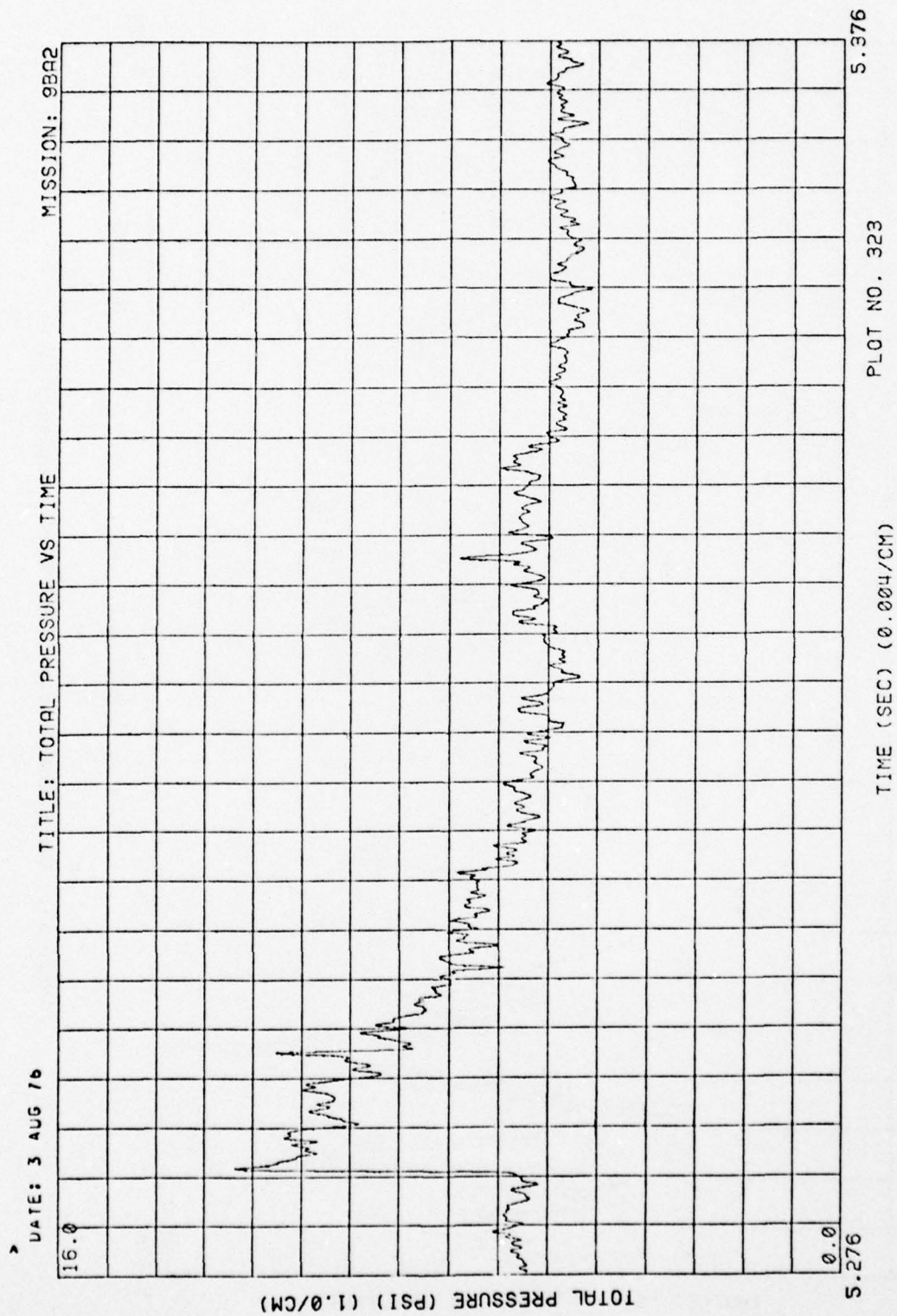


Figure 42. Total Pressure, Run 9B-A2, Intercept 2

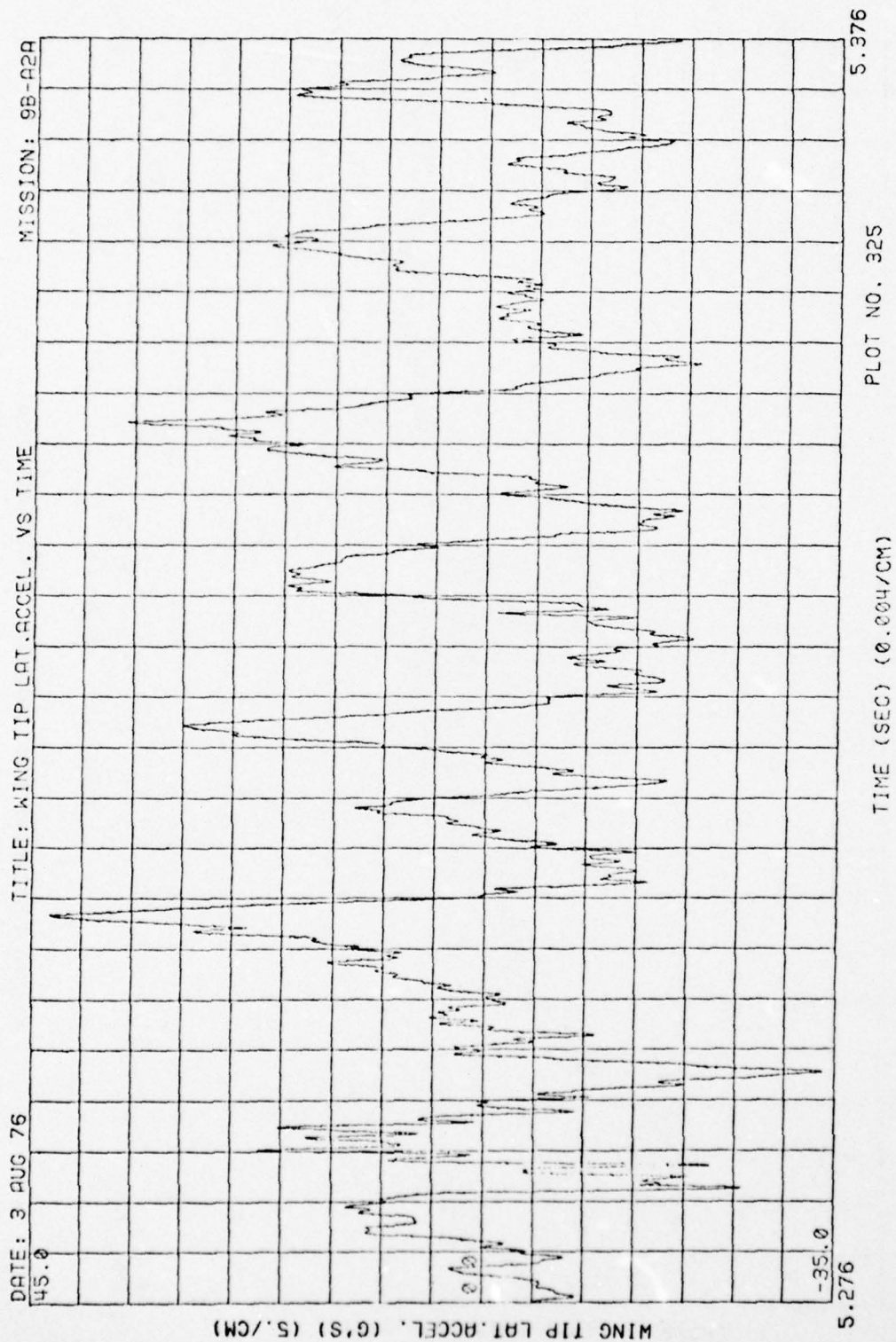


Figure 43. Wing Acceleration, Run 9B-A2, Intercept 2

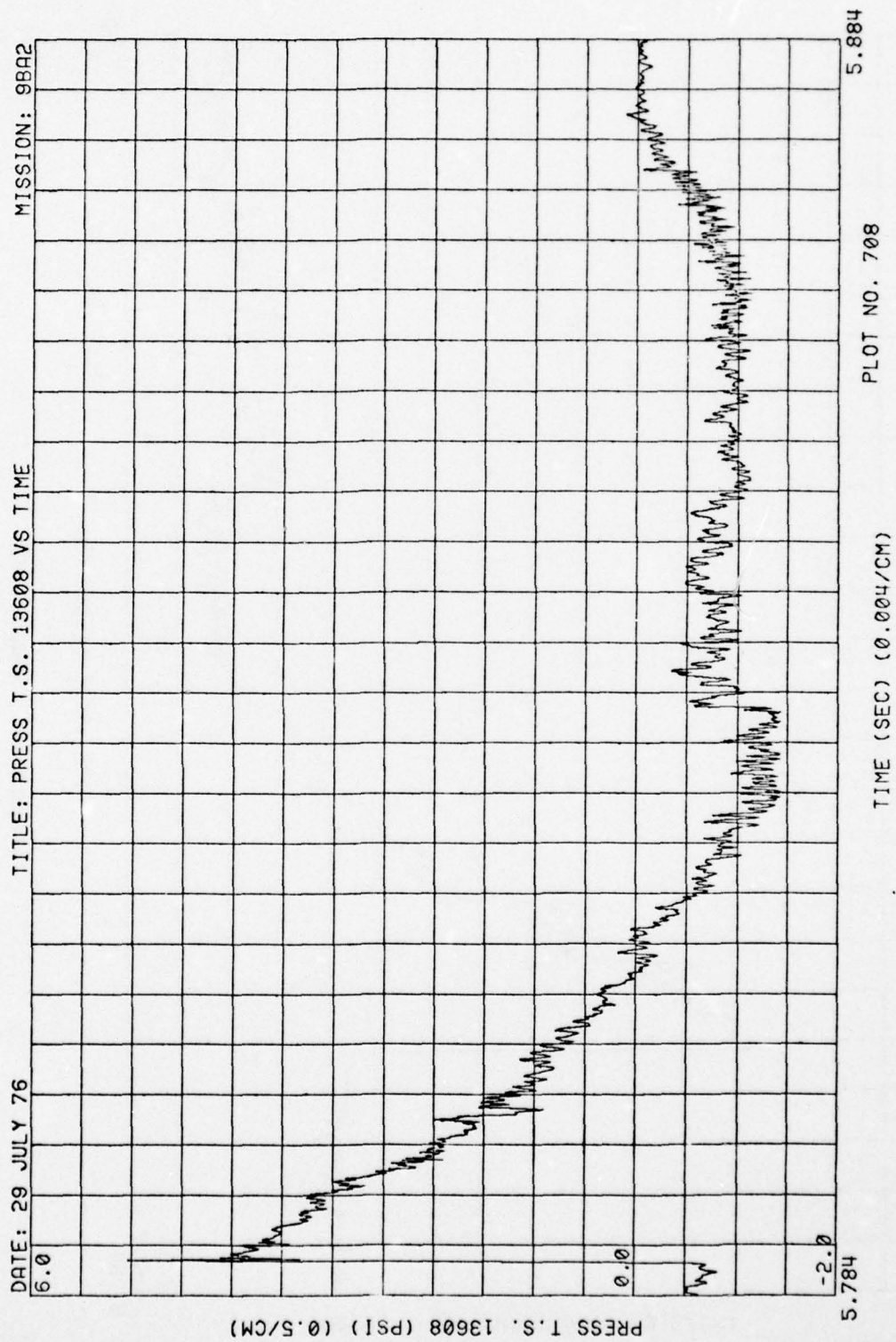


Figure 44. Blast-Line Overpressures, Run 9B-A2, Intercept 3

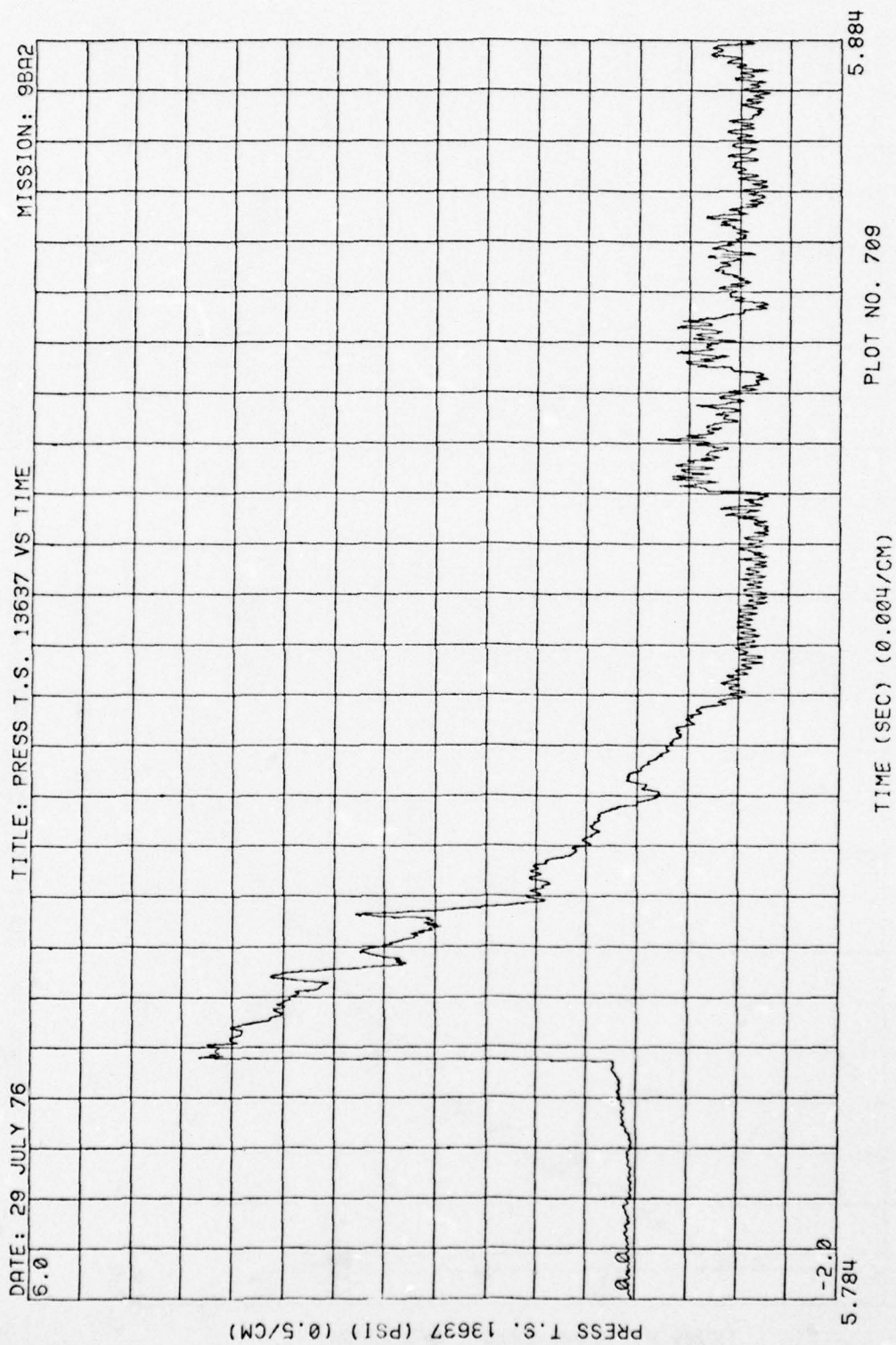


Figure 44. (Continued)

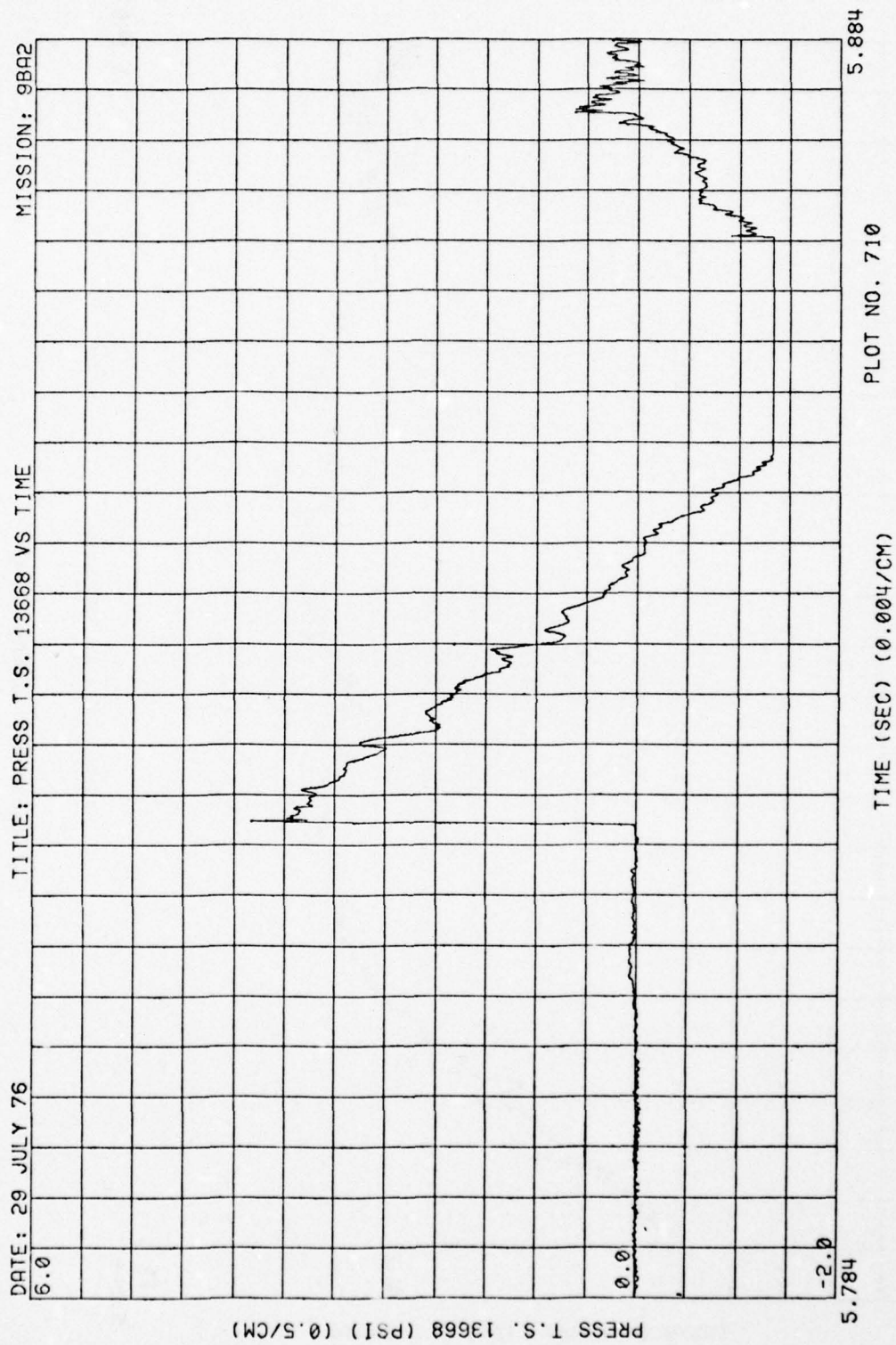


Figure 44. (Continued)

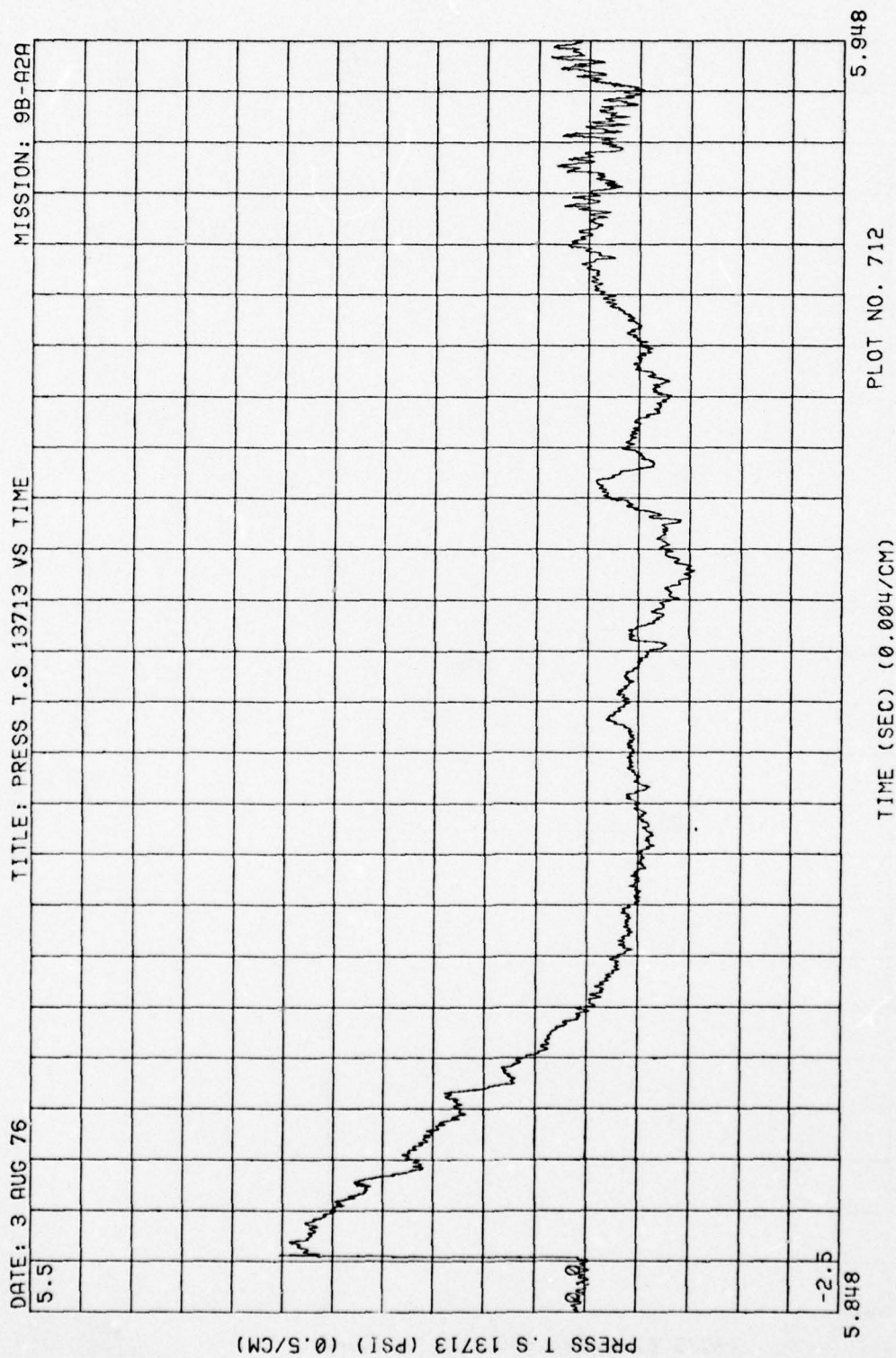


Figure 44. (Concluded)

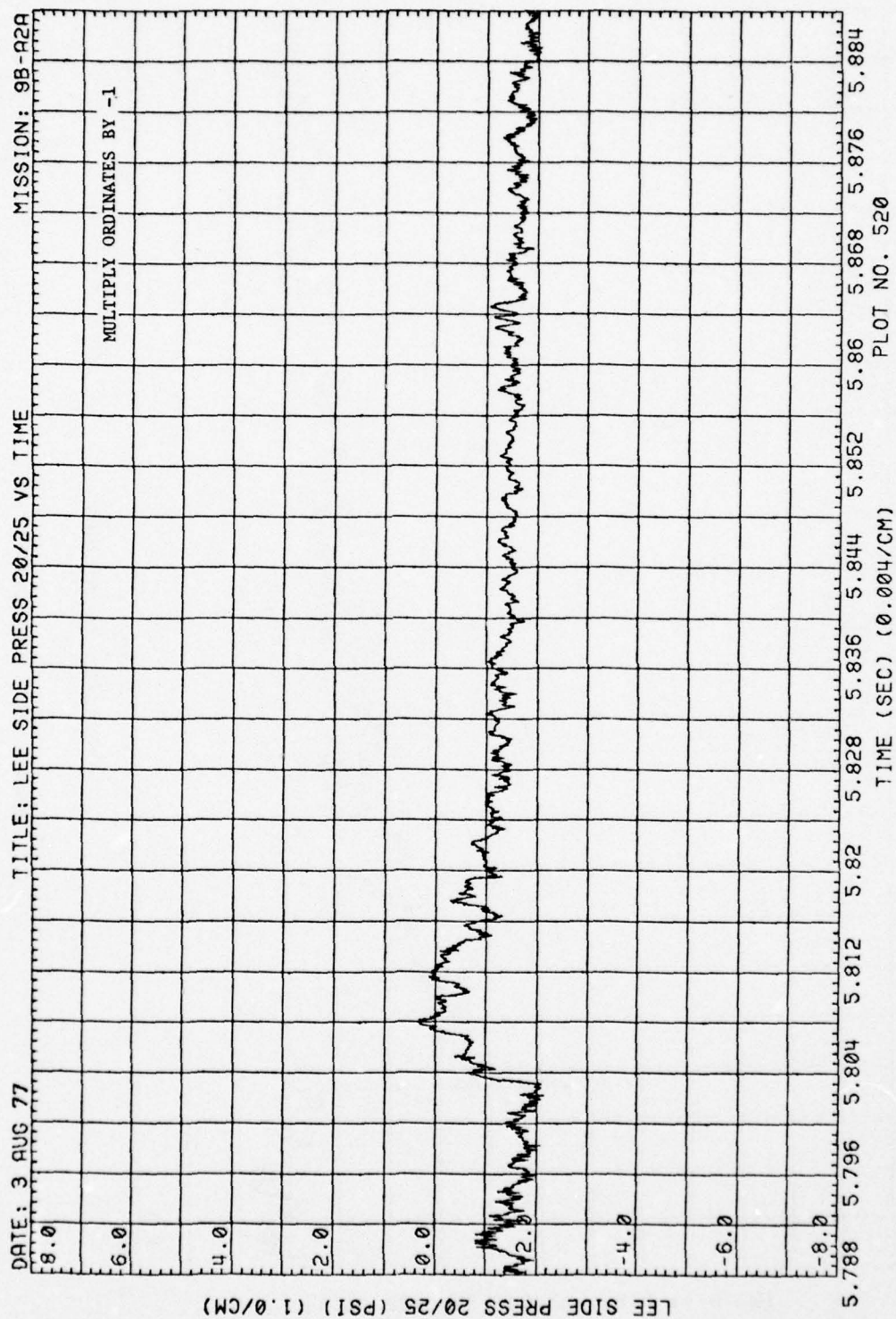


Figure 45. Blastward and Leeward Wing Pressures, Run 9B-A2, Intercept 3

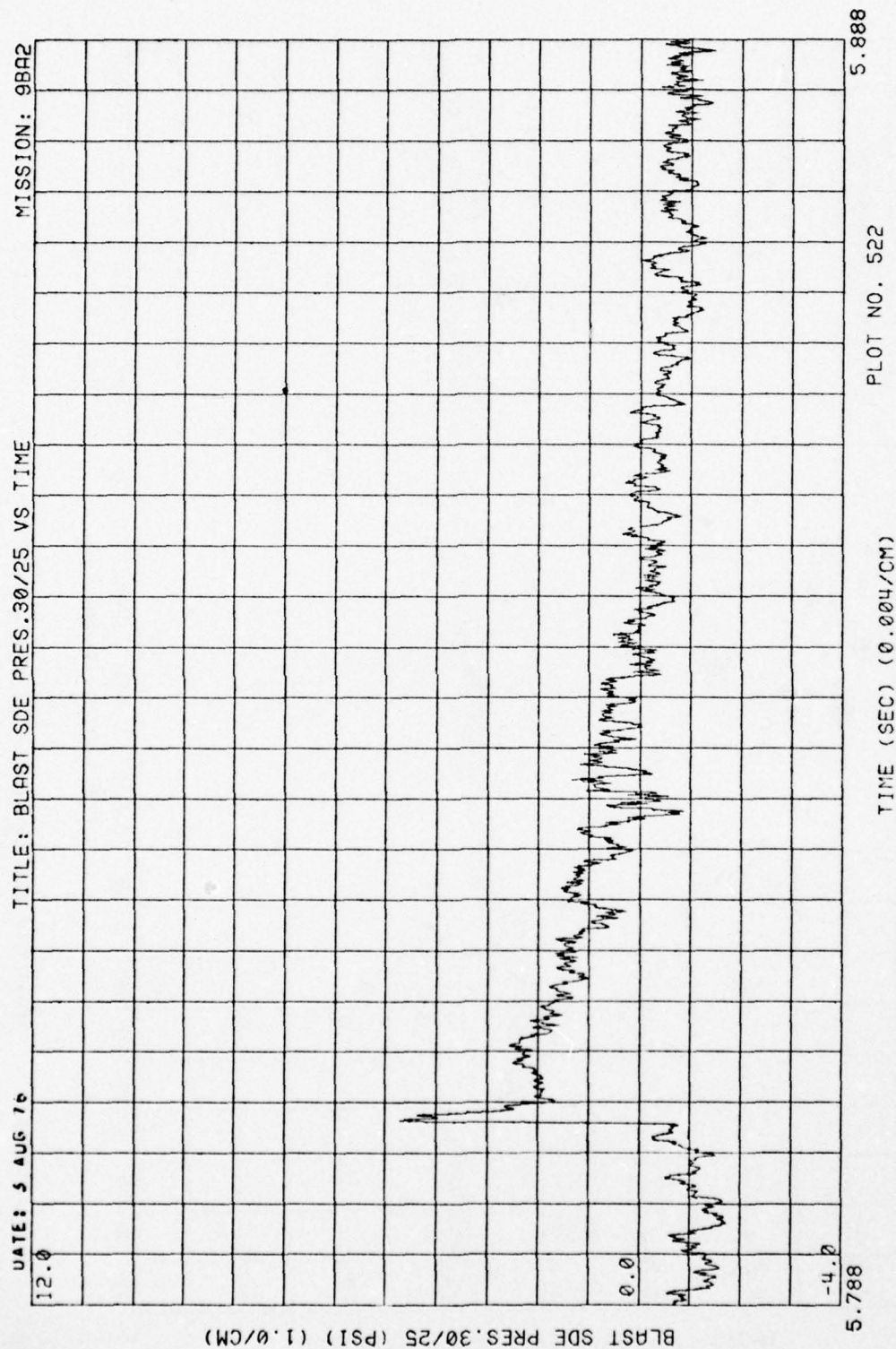


Figure 45. (Continued)

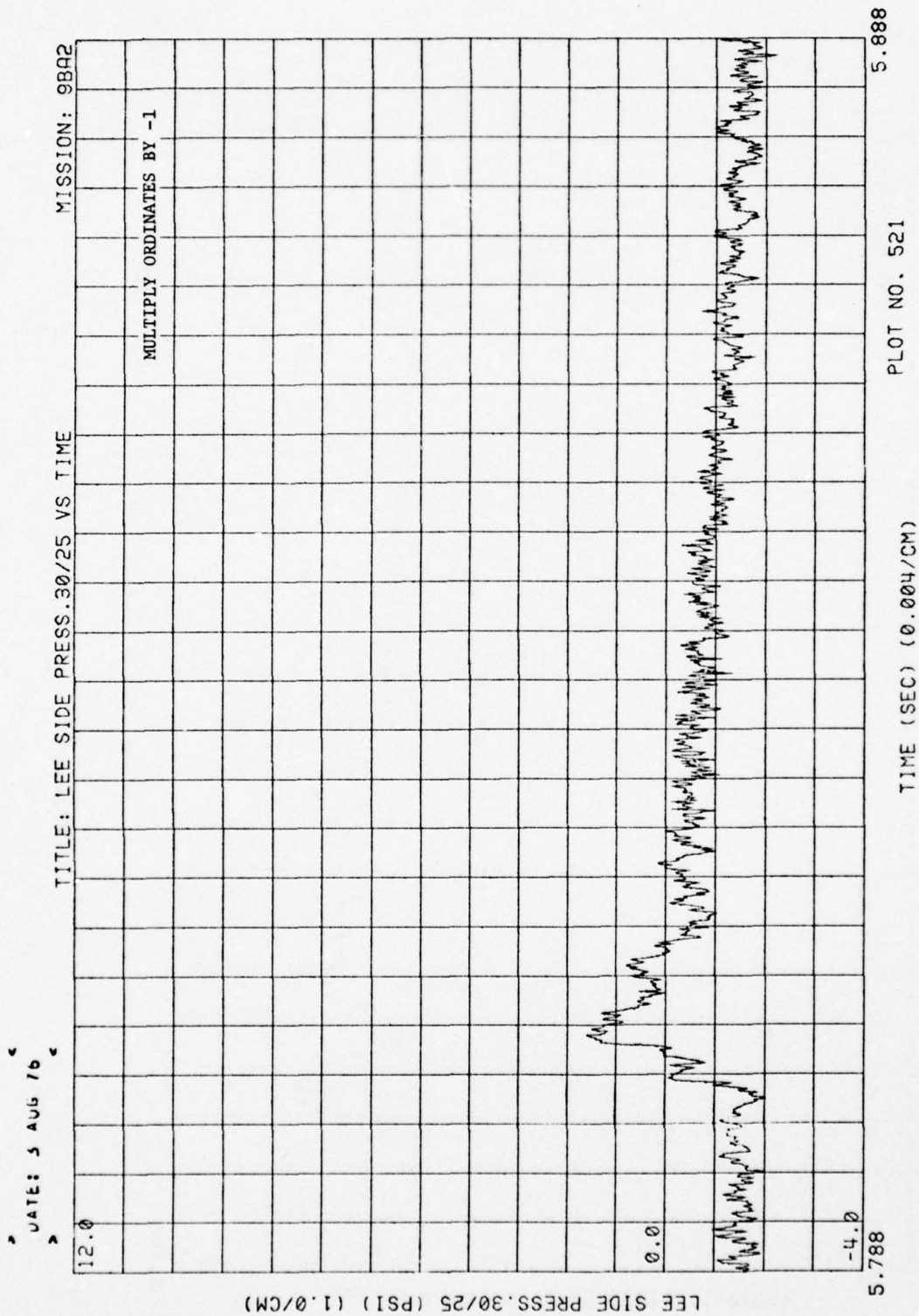


Figure 45. (Continued)

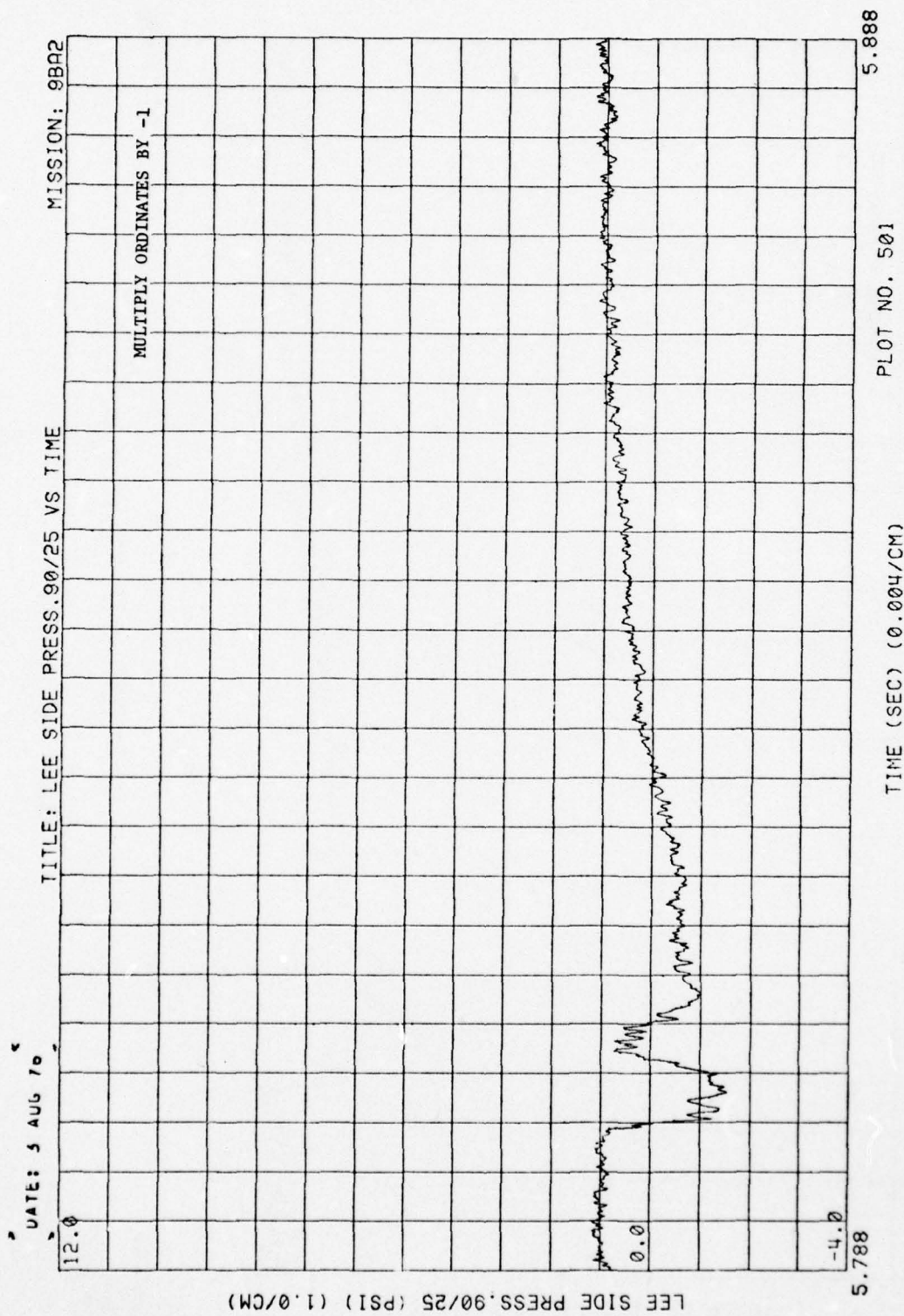


Figure 45. (Concluded)

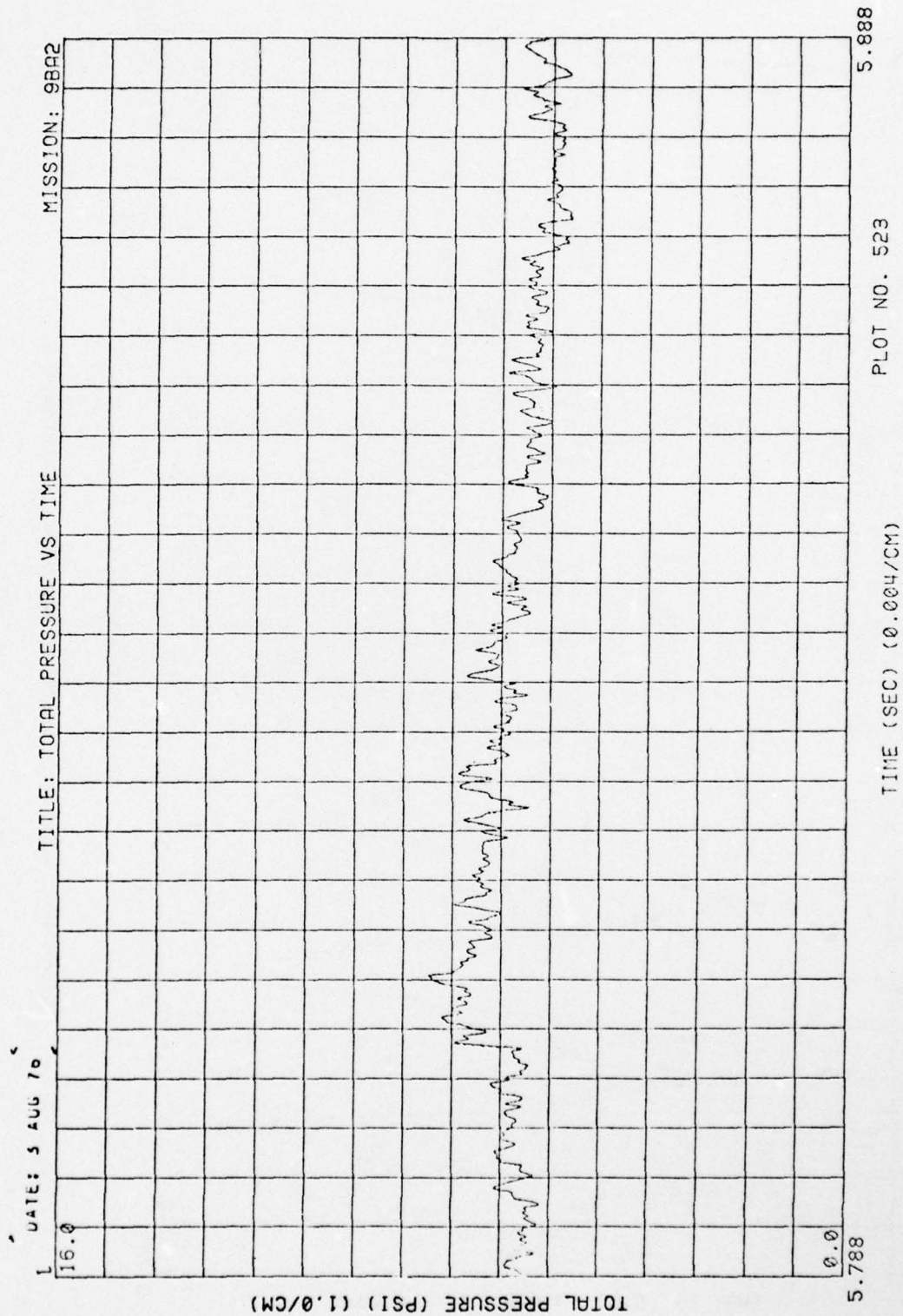


Figure 5. Total Pressure, Run 9B-A2, Intercept 3

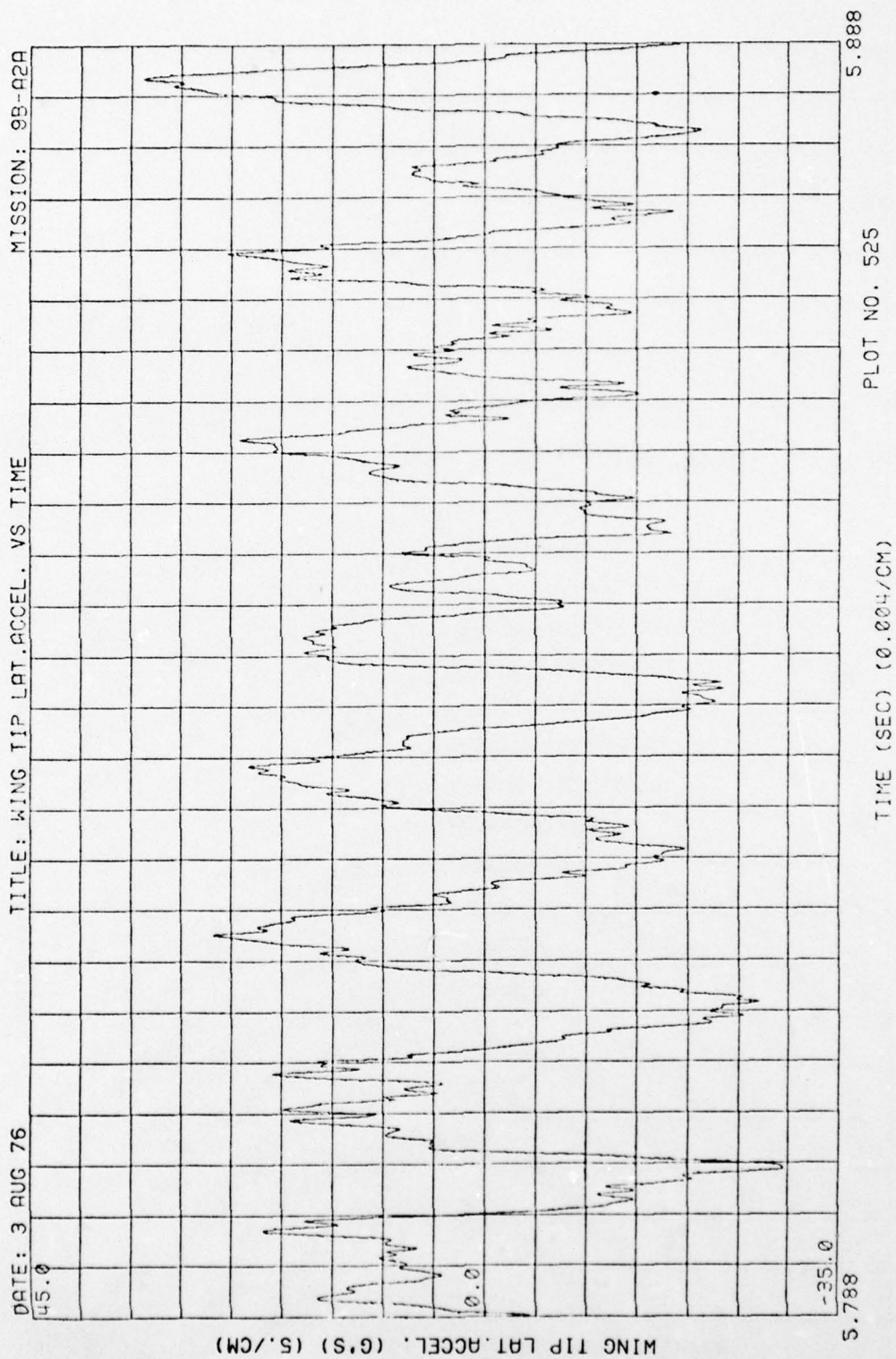


Figure 47. Wing Acceleration, Run 9B-A2, Intercept 3

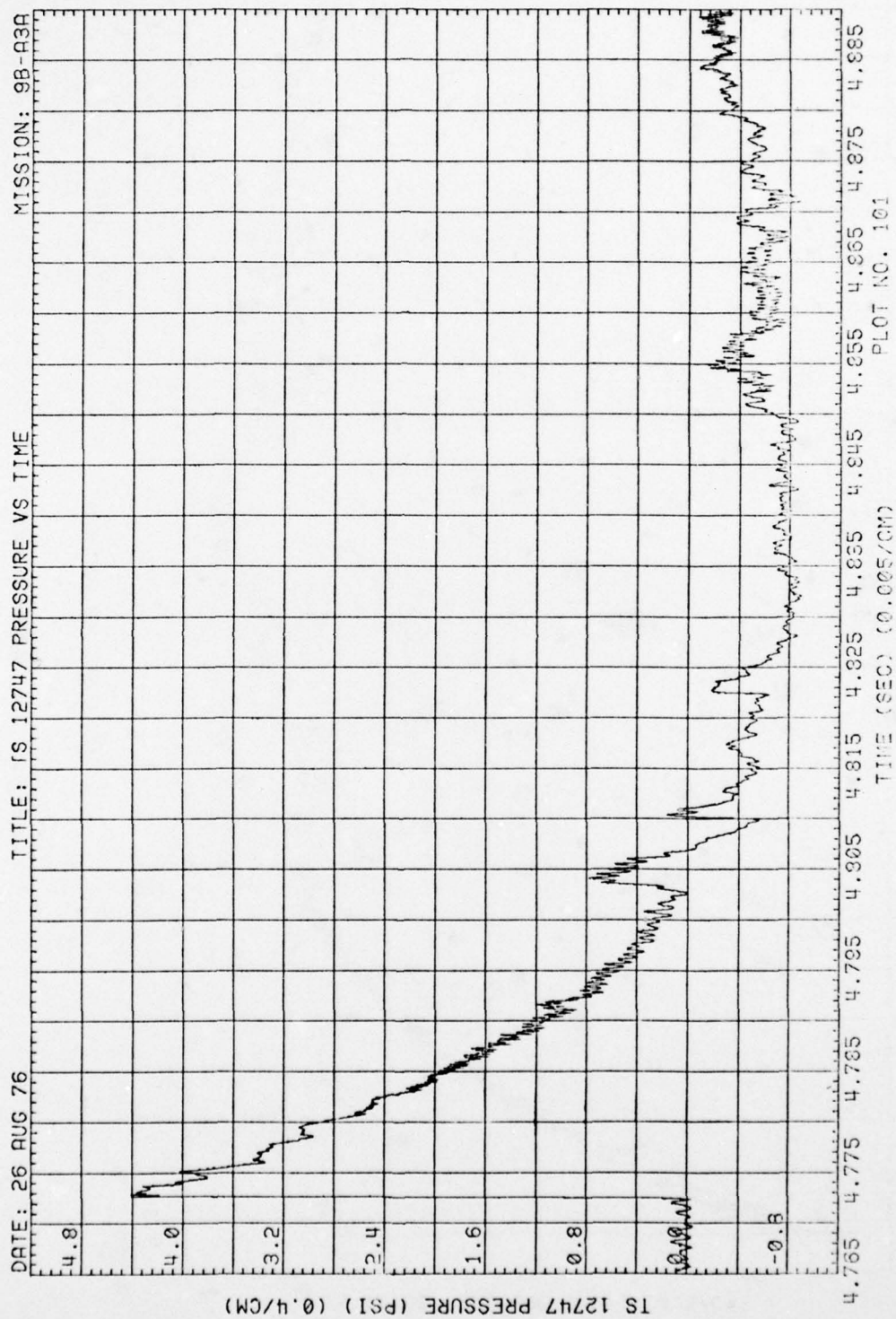


Figure 48. Blast-Line Overpressures, Run 9B-A3, Intercept 1

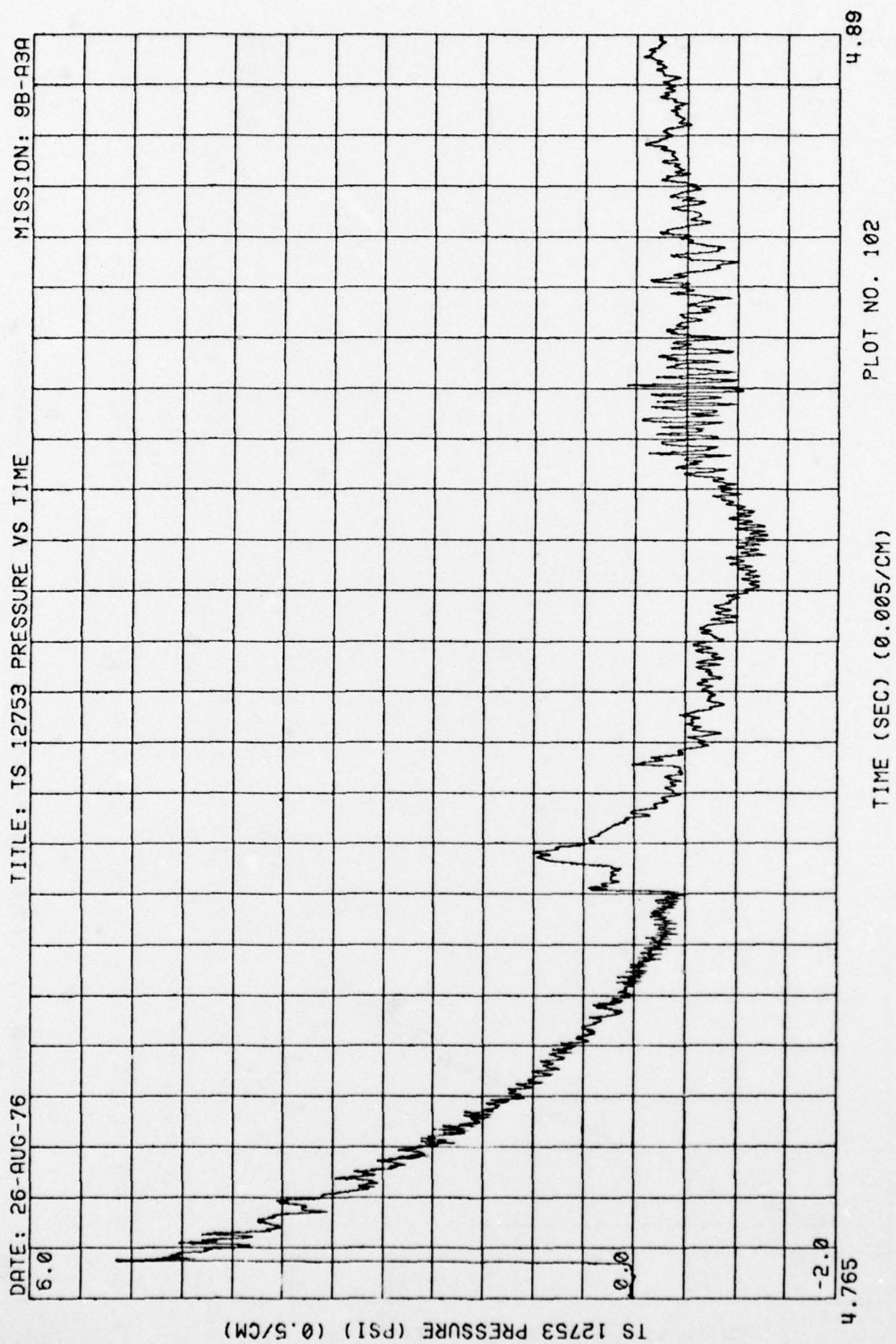


Figure 48. (Continued)

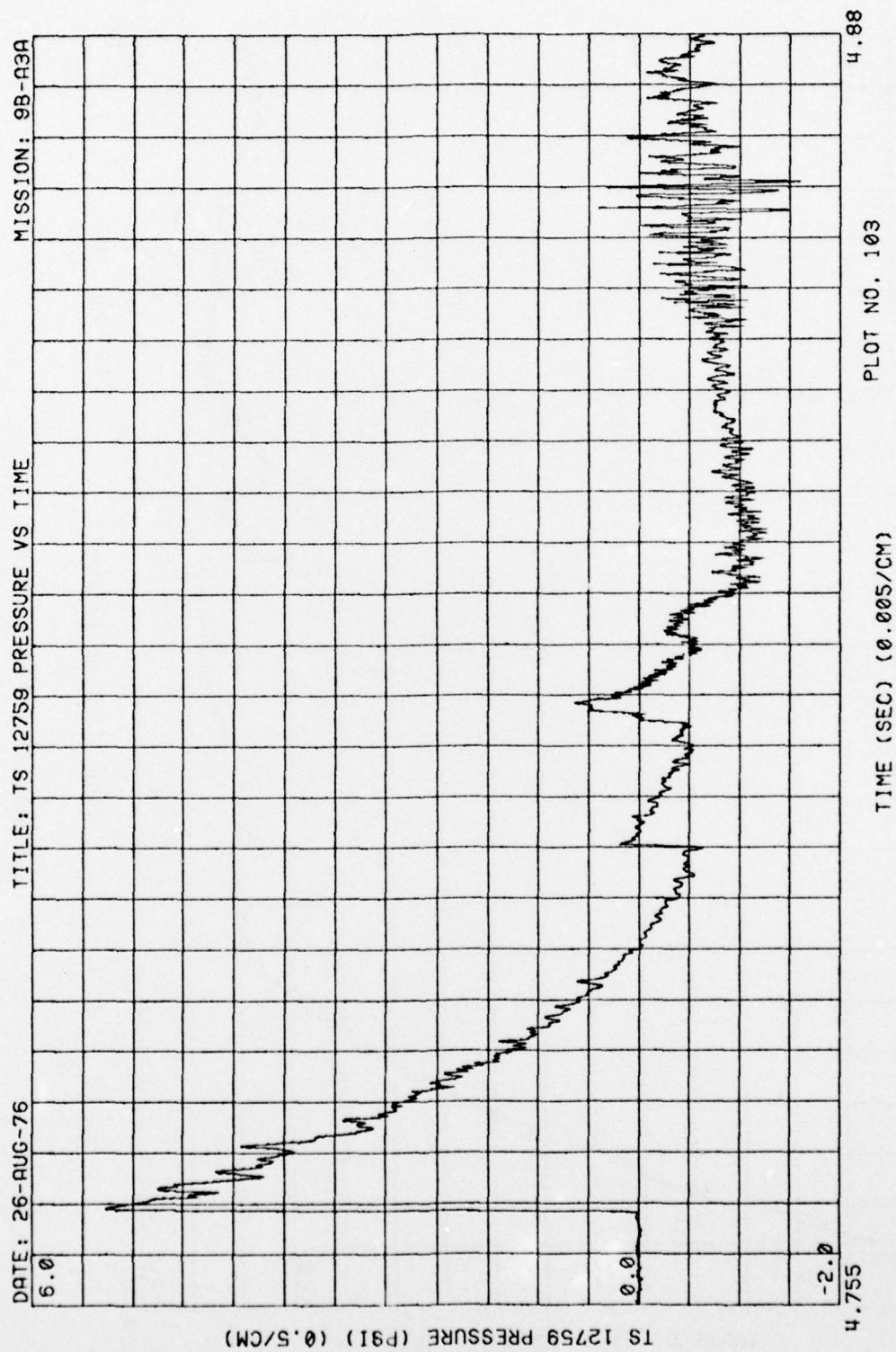


Figure 48. (Continued)

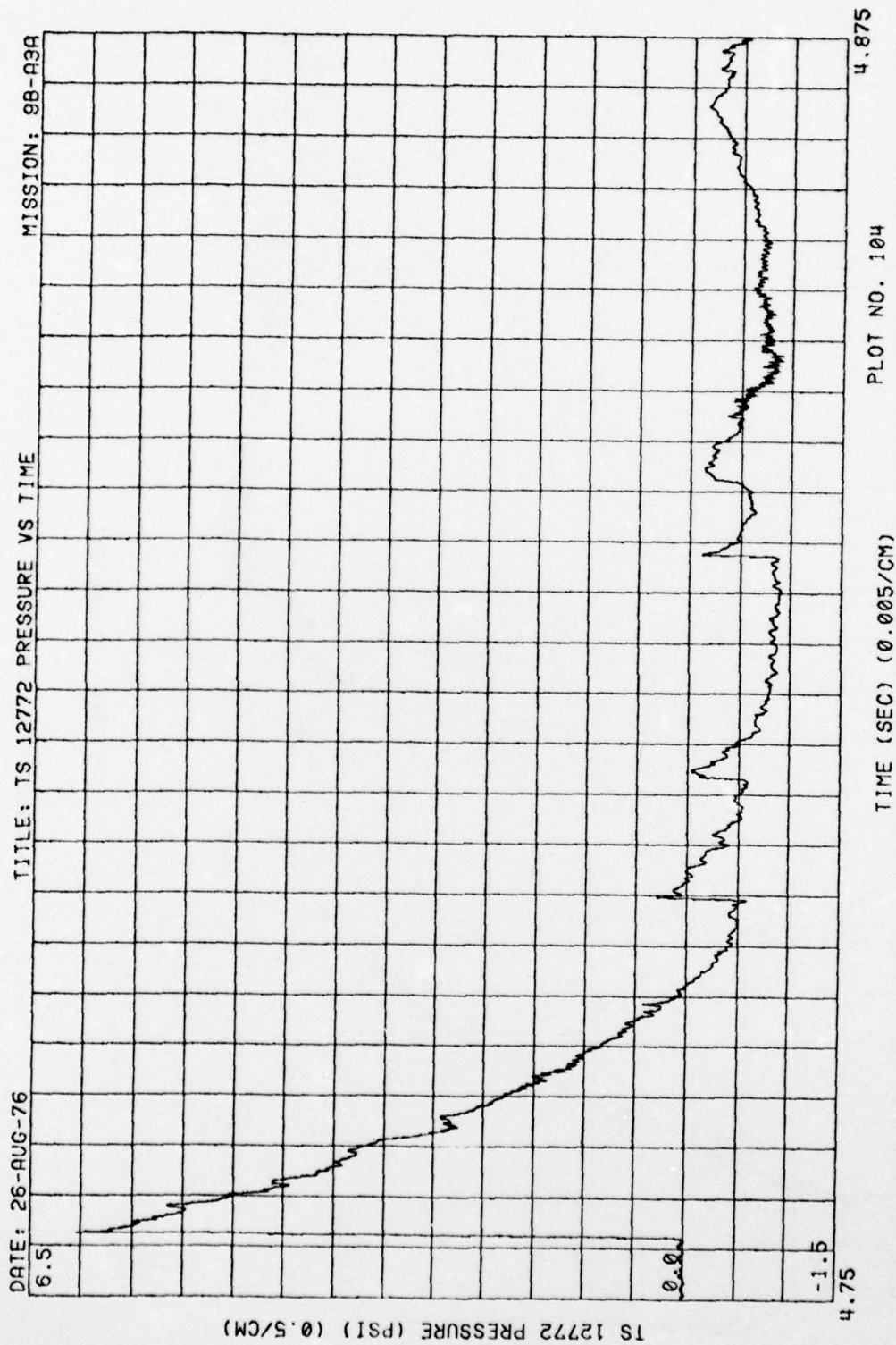


Figure 48. (Concluded)

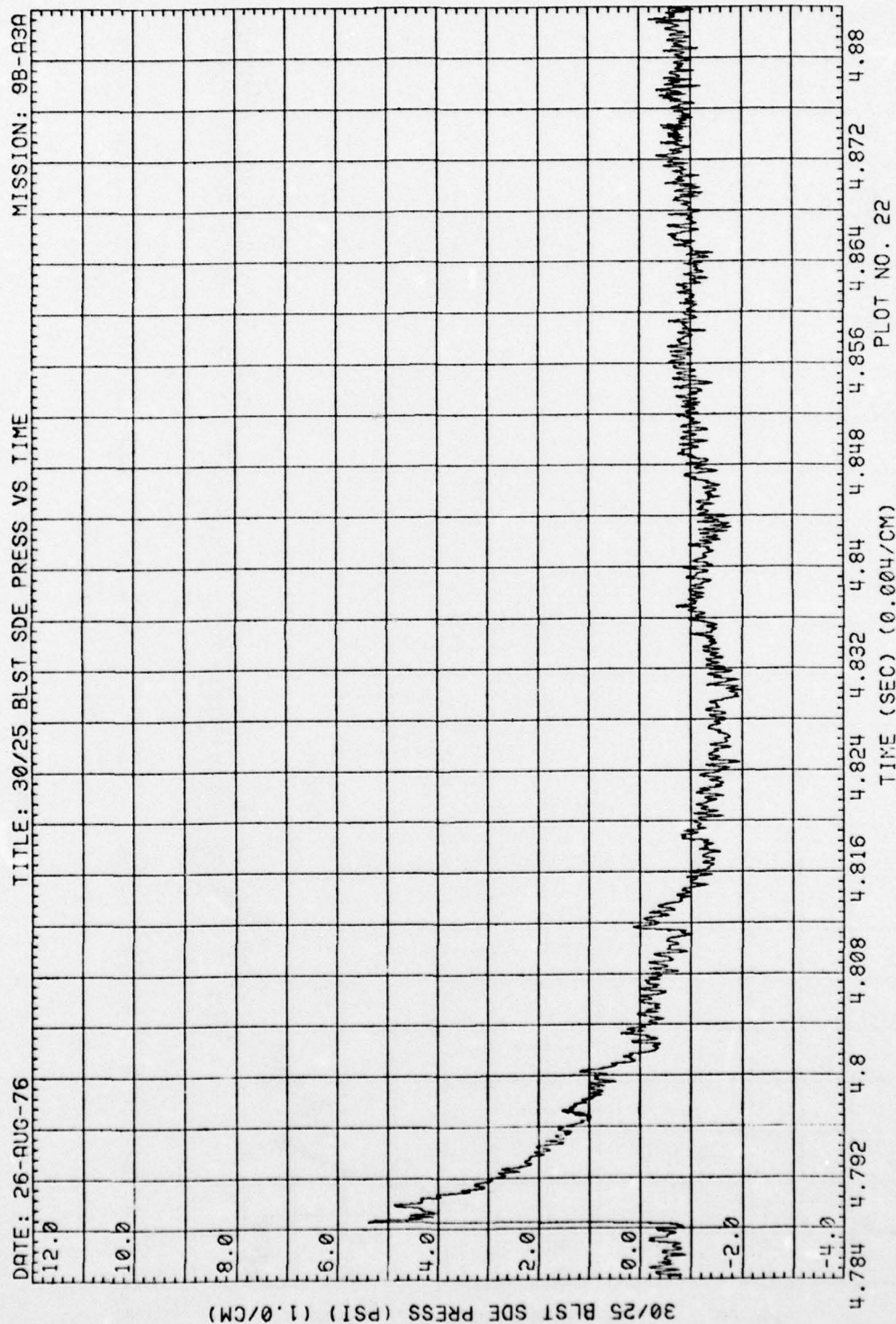


Figure 49. Blastward and Leeward Wing Pressures, Run 9B-A3, Intercept 1

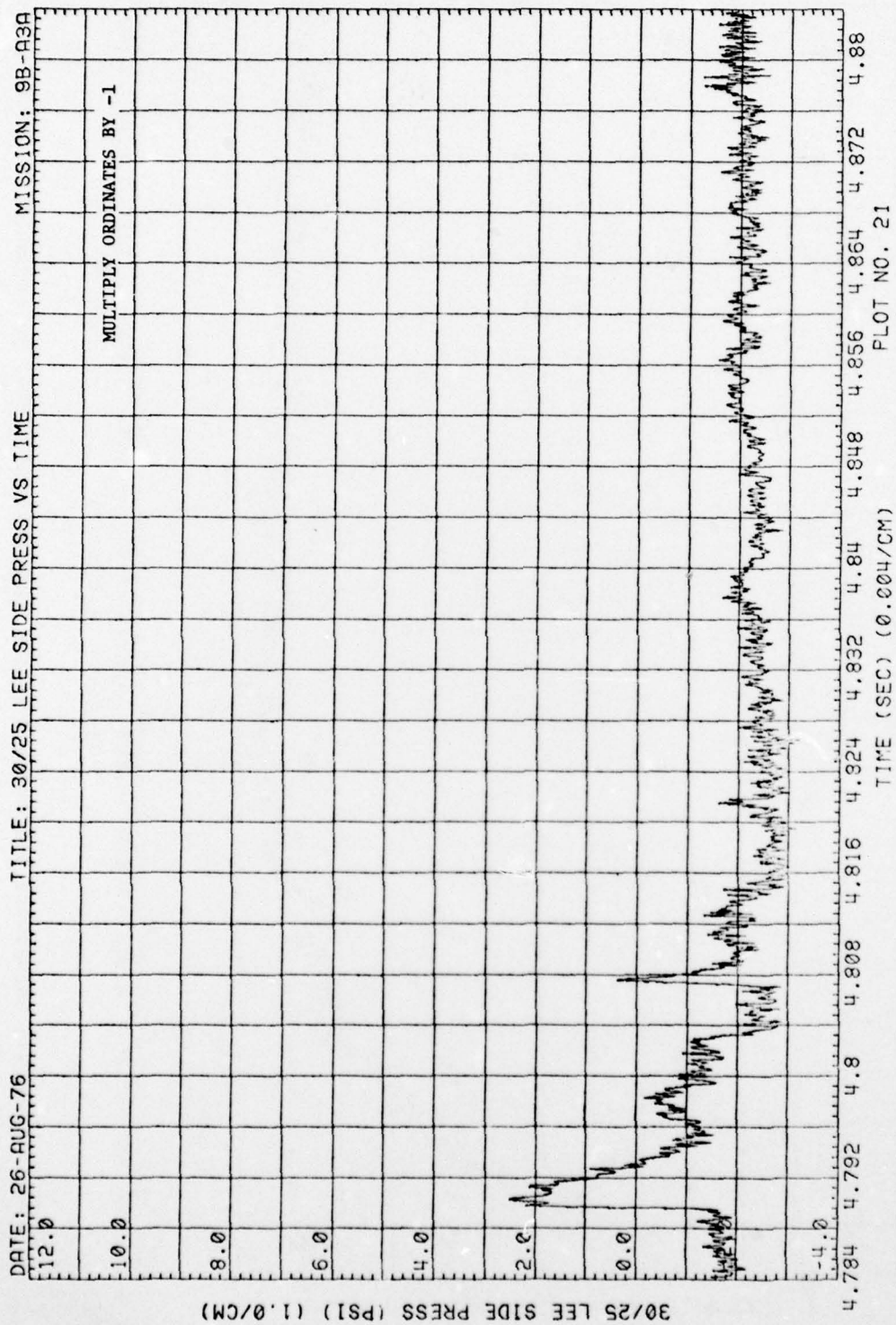


Figure 49. (Continued)

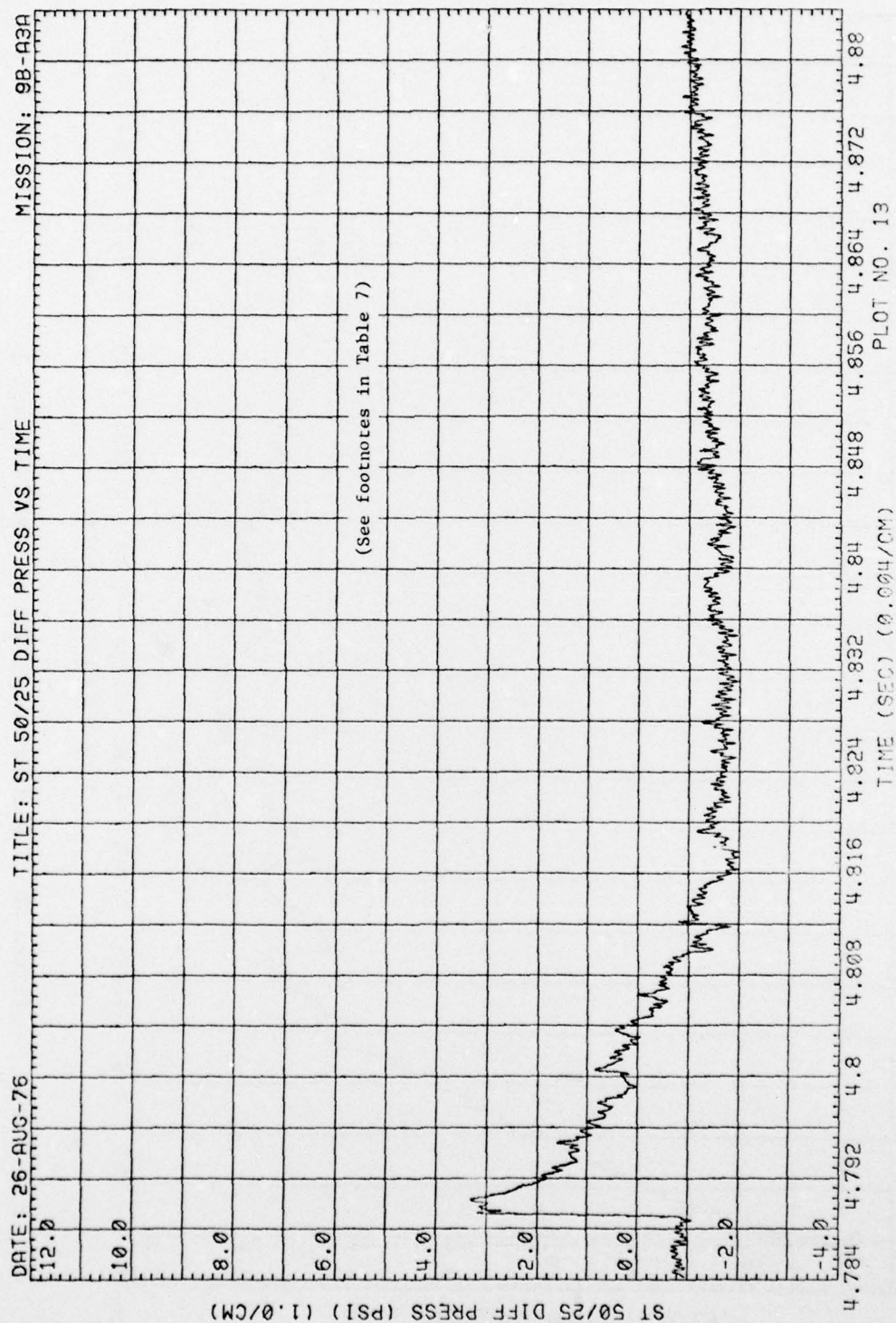


Figure 49. (Concluded)

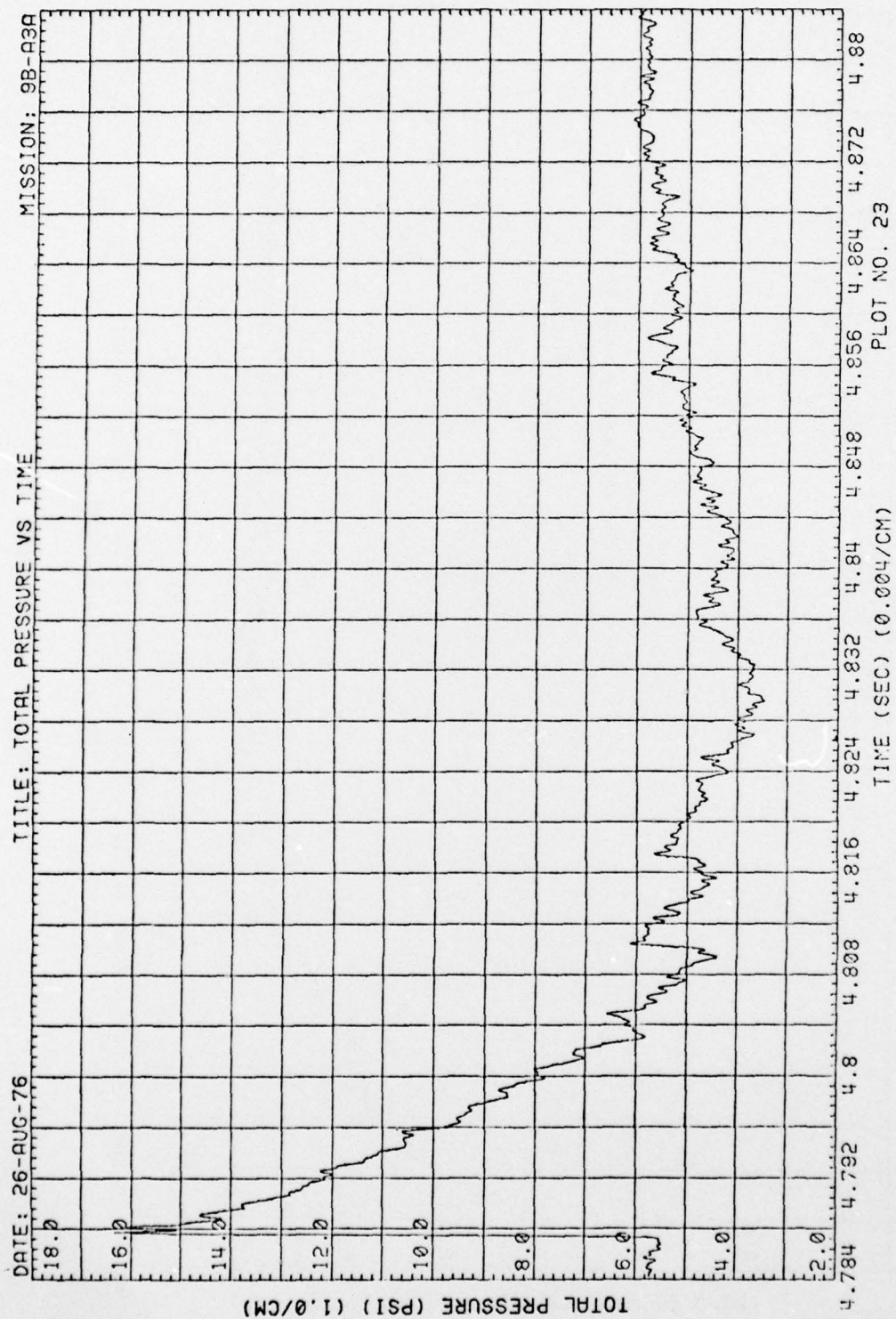


Figure 50. Total Pressure, Run 9B-A3, Intercept 1

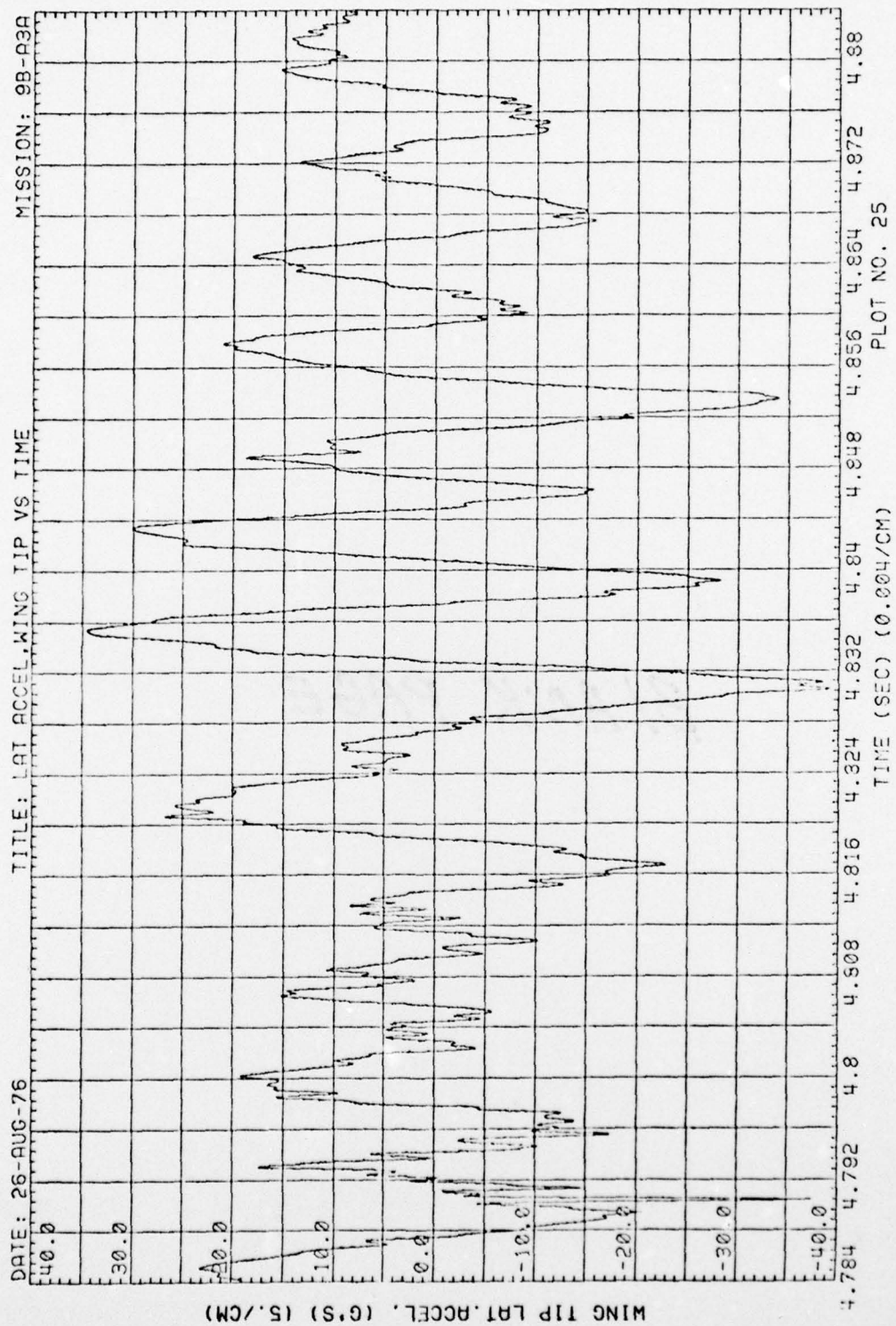


Figure 51. Wing Acceleration, Run 9B-A3, Intercept 1

APPENDIX B

DENSITY AND VELOCITY TIME HISTORIES

Blast density and material velocity time histories at the sled were determined from the overpressure time histories of Section 5 by use of the method of Reference 12, which utilizes plots of pressure, density and velocity derived from Brode's theory (Ref. 13). The particular plot needed is an unnumbered contour plot provided in the pocket of Reference 12 of the variables π , η , β with the abscissa $(\tau-\gamma)$ covering the range - 0.6 to -0.1 and the ordinate λ covering the range 0.8 to 2.6, where

$$\pi = \Delta p/p_o + 1$$

$$\eta = \rho/\rho_o$$

$$\beta = v/a_o$$

$$\tau = a_o t/\alpha$$

$$\lambda = r/\alpha$$

a_o is ambient speed of sound

p_o is ambient pressure

ρ is air density

v is blast material velocity

$$\alpha = \sqrt[3]{W/p_o}$$

W is total energy release

and subscript o designates ambient (pre-blast) conditions.

In applying this figure to the present problem it was found that the density and velocity curves (η and β curves) in the figure did not exactly satisfy the theoretical relationships for a normal shock. Consequently it was found advisable to slightly shift the upper end of all of the η and β curves in the figure for positive overdensity or positive material velocity (which are all straight lines) so that they would be consistent with the corresponding overpressure (π) curves at the shock front with regard to normal shock theory. Corrected η and β curves were then obtained by drawing straight lines between the shifted upper ends of these curves and the unaltered lower endpoints of the curves.

DISTRIBUTION LIST

DEPARTMENT OF DEFENSE

Director
Defense Nuclear Agency
ATTN: TISI Archives
ATTN: STSP
ATTN: DDST
ATTN: SPAS
3 cy ATTN: TITL, Tech. Lib

Under Sec'y of Def. for Rsch. & Engrg.
ATTN: S&SS (OS)

Commander, Field Command
Defense Nuclear Agency
ATTN: FCPR

Chief
Livermore Division, FCDNA
Lawrence Livermore Laboratory
ATTN: FCPRL

Defense Documentation Center
Cameron Station
12 cy ATTN: TC

DEPARTMENT OF THE ARMY

Commander
Harry Diamond Laboratories
ATTN: DRXDO-RBH, James H. Gwaltney
ATTN: DRXDO-NP

Director
U.S. Army Ballistic Research Labs.
ATTN: DRXBR-X, Julius J. Meszaros

Commander
U.S. Army Materiel Dev. & Readiness Cmd.
ATTN: DRCDE-D, Lawrence Flynn

Commander
U.S. Army Nuclear Agency
ATTN: MAJ J. Vecke
ATTN: COL Deverill

DEPARTMENT OF THE NAVY

Chief of Naval Material
ATTN: MAT 0323

Chief of Naval Research
ATTN: Code 464, Thomas P. Quinn

Director
Naval Research Laboratory
ATTN: Code 2600, Tech. Lib

Officer-in-Charge
Naval Surface Weapons Center
ATTN: Ken Caudle

Commanding Officer
Naval Weapons Evaluation Facility
ATTN: Peter Hughes

DEPARTMENT OF THE NAVY (Continued)

Director
Strategic Systems Project Office
ATTN: NSP-272

DEPARTMENT OF THE AIR FORCE

AF Materials Laboratory, AFSC
ATTN: MBC, Donald L. Schmidt
ATTN: MBE

AF Weapons Laboratory, AFSC
ATTN: DYV, Lt Col Rensvold
ATTN: SUL

Commander
ASD
4 cy ATTN: ENFS, D. Ward

Commander
Foreign Technology Division, AFSC
ATTN: PDBF, Mr. Spring

Commander in Chief
Strategic Air Command
ATTN: XPFS

DEPARTMENT OF ENERGY

Sandia Laboratories
ATTN: Doc. Control for D. McCloskey

DEPARTMENT OF DEFENSE CONTRACTORS

Aerospace Corporation
ATTN: W. Barry

Avco Research & Systems Group
ATTN: William Broding
ATTN: J. Patrick

The Boeing Company
ATTN: Robert Dyr-dahl
ATTN: Ed York

Boeing Wichita Company
ATTN: D. Pierson
ATTN: R. Syring

Effects Technology, Inc.
ATTN: Richard Parisse

General Dynamics Corp.
ATTN: R. Shemensky

General Electric Company
TEMPO-Center for Advanced Studies
ATTN: DASIAC

Kaman AviDyne
Division of Kaman Sciences Corp.
ATTN: Norman P. Hobbs
ATTN: J. Ray Ruetenik
ATTN: Robert F. Smiley

DEPARTMENT OF DEFENSE CONTRACTORS (Continued)

Kaman Sciences Corporation
ATTN: Donald C. Sachs

Martin Marietta Corporation, Orlando Division
ATTN: Gene Aiello

McDonnell Douglas Corporation
ATTN: J. McGrew

Northrop Corporation
ATTN: Don Hicks

Prototype Development Associates, Inc.
ATTN: John McDonald

DEPARTMENT OF DEFENSE CONTRACTORS (Continued)

R & D Associates
ATTN: Albert L. Latter
ATTN: F. A. Field
ATTN: Jerry Carpenter

Rockwell International Corporation
ATTN: R. Sparling

Science Applications, Inc.
ATTN: Dwane Hove

SRI International
ATTN: George R. Abrahamson